Engineering Multicomponent Nanomaterials for Plasmonic Catalysis

by

Umar Aslam

A dissertation submitted in partial fulfillment
of the requirements for the degree of
Doctor of Philosophy
(Chemical Engineering)
in the University of Michigan
2018

Doctoral Committee:

      Professor Suljo Linic, Chair
      Professor Kevin Kubarych
      Associate Professor Timothy Scott
      Assistant Professor Nirala Singh

Umar Aslam

uaslam@umich.edu

ORCID iD: 0000-0001-8310-2958

Dedication

This dissertation is dedicated to my mom, Iffat Aslam, who has been whispering the right things in my ear for as long as I can remember, my dad, Muhammad Aslam, whose strength has served as an infinite well of inspiration for me, and my three younger siblings, Umaira, Namra, and Taimoor Aslam, for all of whom I strive to be a great role model.

Acknowledgements

The successful completion of this dissertation was by no means the product of my efforts alone. Firstly, I would like to thank my doctoral committee, Prof. Suljo Linic, Prof. Kevin Kubarych, Prof. Timothy Scott, and Prof. Nirala Singh for being very helpful especially in these past few months. Things have come together quickly and I really appreciate the committee's flexibility. I would also like to thank Prof. Mark Barteau and Prof. Levi Thompson for providing feedback on my research work early on and writing recommendation letters for various applications.

Much of my development as a scientist and critical thinker over the last five years has been the product of the guidance and supervision provided by my dissertation advisor, Prof. Suljo Linic. Beyond simply providing the necessary resources for conducting scientific research, Suljo always pushed me to develop my scientific acumen and overall critical thinking skills. His curiosity, passion, and analytical approach to problem solving have been contagious. Suljo has helped me directly and indirectly in innumerable ways over the last five years, and I owe him a great deal of gratitude for that. I have never been very good at saying "thank you", but I hope that my actions have reflected the appreciation and respect I have for him.

I would also like to acknowledge current and past members of the Linic Lab who have helped me in countless ways. I would like to thank Michelle Przybylek for getting me started and Timothy Van Cleve, Brittany Farrell, and Paul Hernley for helping me develop various lab skills. Calvin Boerigter was a great colleague with who I shared fun conversions about science, politics, and a plethora of other topics. Along with Calvin, Matthew Morabito and Robert Campana made

for great lunch buddies and labmates. I also enjoyed discussing experiments and ideas with Young Geun Park and Saman Moniri. The current members of the Linic Lab, Vishal Govind Rao, Valentina Igenegbai, Joseph Quinn, Steven Chavez, Sean Dix, John Hemmerling, Rawan Almallahi, Rachel Elias, and Jacques Esterhuizen, have been very fun to work with. I've enjoyed our many spontaneous conversions on random topics and occasionally science. In particular, Valentina Igenegbai has been a great frie- I mean labmate who I always turned to for advice on anything and everything. I worked directly with Steven Chavez for a couple of years, and it has never been boring working with him. I'll always remember the Jimmy-Johns-fueled hustle we put in to finish getting data for the Nat Nano paper in the last two months of 2016. I've also worked directly with Vishal Govind Rao on some exciting projects that have been quite insightful. These last few months, I've been working with and training Rachel Elias. I'm hopeful that Rachel (and everyone else for that matter) will do very well with their future research. Special shout-out to Sean Dix as well who drew the shortest straw and ended up as my officemate for the last two years! These last couple years in the lab have been immensely enjoyable and it's all thanks to the members of the team. Having been a part of the group will always serve as a source of pride.

I've had the pleasure of working with a number of great undergraduate students (Tsatsral Battsengel, Austin Hegg, Miles Beauchamp, Alexander Marmorale, Devesh Shah, Joseph Moss, Amy Dao, Gaurav Hosur). Working with these students has been energizing and helped me improve as a scientific communicator, teacher, and leader. These students also played a key role in my ability to juggle up to six projects at a time. I was able to accomplish much more than I could have myself with their help and hope that they also gained some skills, perceptive, and scientific knowledge along the way.

The Chemical Engineering support staff also deserve special acknowledgment for their help with scheduling various events and completing orders. As manager of lab supplies and primary contact on a number of new equipment purchases, I would like to thank Connie Bacus, Barbara Perry, and Jennifer Downey in particular for all of their help (and patience!) with ordering equipment and supplies. Susan Hamlin has also been very helpful in navigating the PhD program. Whenever in doubt about some aspect of the program, Susan has been the person to turn to.

In addition, I would like to mention Trenton Wilke for his help with mass spectrometry experiments. The support staff of MC^2 also deserve special thanks for helping train and help me with electron microscopy and other techniques. I would especially like to thank Dr. Kai Sun of MC^2 for his support. Franklin Epiepang has been a great friend since my first year here. Frank and I can go back and forth for hours. He's had my "6" for the last 5 years and I've had his.

Lastly, I would like to thank my mom, Iffat Aslam, and dad, Muhammad Aslam. My parents moved to the US 25 years ago in search of a better life for their kids. They have made countless sacrifices and shouldered the weight of all hardships themselves. All of my accomplishments are in large part a reflection of their efforts. The completion of this degree ends a meaningful 5-year journey for me, but in some ways ends an even more profound 25-year journey for my parents. I would also like to thank my three younger siblings, Umaira Aslam, Namra Aslam, and Taimoor Aslam. The three of them have been my best friends for as long as I can remember and I value nothing more than spending time with them. Ideally, the four of us could go out for lunch or maybe coffee every week, but online video games work pretty well too! Hopefully, we will all get back together one day soon.

Table of Contents

List of Figures

Abstract

Heterogenous catalysis is an important technology used to facilitate chemical transformations. As increasing demand for chemicals and materials stresses the availability of resources and the environment, it is becoming ever more important to design catalysts with near perfect selectivity in the conversion of reactant feedstock to desired products. In traditional heterogeneous catalysis, heat is used to drive the conversion of reactants to products. An unintended side effect of this approach is that energy is unselectively deposited into all possible reaction pathways resulting in the simultaneous activation of undesired reactions, waste of feedstock resources, and production of chemical waste. An alternative mechanism for activating chemical reactions employs visible light to deposit energy into reactants. This mechanism could in principle make it possible to achieve much higher product selectivities but has been considered impractical as it requires high intensity lasers to produce sufficiently high reaction rates. Recently, it has been shown that plasmonic metal nanoparticles (Cu, Ag, and Au) can perform light-driven chemical reactions under relatively low intensity light on the order of sunlight. These findings have reignited interest in light-driven chemical reactions in heterogeneous catalysis and led to the emergence of a new field known as plasmonic catalysis. A major limitation of plasmonic catalysis is that it is restricted to reactions that can be performed by the plasmonic metals, Cu, Ag, and Au. In this dissertation, we address this limitation through the design of multicomponent plasmonic catalysts which combine plasmonic metals with catalytically-active materials. In particular, we focus on combining plasmonic metals, such as Ag, with catalytically-active metals, such as Pt, through the fabrication of bimetallic nanoparticles. We consider two extremes for synthesizing

nanoparticles composed of both metals: 1) alloy nanoparticles in which both metals are well-mixed and 2) core-shell structures in which a large Ag core is completely surrounded with a thin shell of Pt. We develop novel synthesis approaches for creating both structures and use a suite of characterization tools to shed light on the nanoscale structure and composition of the resulting materials. We then use the well-defined core-shell nanoparticles to perform a mechanistic investigation of the energy transfer mechanisms which allow for energy to be transferred from photoexcited plasmonic metals to catalytically-active sites. These studies demonstrate that coating a thin layer of a catalytic metal, such as Pt, on a plasmonic metal drastically biases the flow of energy in the nanoparticles towards absorption in the catalytic metal. We then design reactor studies showing that this re-routing of plasmonic energy enables plasmon-driven reactions to take place on non-plasmonic metal surfaces. These discoveries not only introduce new methods for precision synthesis of multimetallic nanostructures but also present a clear understanding for the physical mechanisms which allow for energy transfer from plasmonic metals to catalytically active sites thereby paving the way for the design of new hybrid plasmonic-catalytic materials for performing light-driven chemical reactions.

Chapter 1 Introduction

1.1 Summary

This chapter introduces the field of heterogeneous catalysis. Several examples aimed to highlight the impact of heterogenous catalysis on society are discussed. The focus then turns to an important subset of heterogeneous catalysts, supported metal nanoparticles. We describe the physical characteristics of metal nanoparticles that grant them their catalytic properties and highlight the widespread application of these materials as commercial catalysts. We then discuss the activation of chemical bonds on metal surfaces at elevated temperatures and the accompanying challenges associated with product selectivity. This temperature-driven activation of chemical bonds is contrasted with an alternative mechanism for activating chemical bonds on metals which relies on energetic charge carriers. We discuss the implications and potential benefits of using energetic charge carriers to drive chemical reactions and introduce plasmonic metal nanoparticles as a class of materials that has recently been shown to allow for high rates of charge carrier-mediated reactions. Finally, the chapter concludes by outlining the overall scope of this dissertation.

1.2 Heterogeneous Catalysis

As the global population continues to grow and standard of living around the world improves, the demand for energy and commodity chemicals is expected to rise rapidly.[1,2] To meet this increasing demand, the energy and chemical industries will need to push production to larger scales while simultaneously improving energy efficiency and minimizing production of chemical by-products. Heterogeneous catalysis has become an indispensable technology for operating within these constraints. Catalysts are materials that accelerate the rates of chemical reactions without being consumed in the process. There are two main advantages to implementing catalysts for chemical transformations. First, catalysts allow chemical transformations to take place at significantly lower temperatures compared to non-catalytic chemical transformations. They do so by providing new pathways for the evolution of reactants to the product state via the formation of chemical intermediates stabilized by the catalyst surface. This allows for chemical transformations that would otherwise require harsh, energy-intensive conditions to take place.

Second, catalytic chemical transformations are often highly selective, preferentially converting reactants to the desired product while mitigating conversion of reactants to waste products. This feature of chemical catalysis is becoming increasingly more important as chemical conversion processes grow to larger scales, feedstock resources become increasingly scarce, and the environmental impact of and costs associated with chemical waste become more pronounced.[3,4] For these reasons, the discovery and development of new catalysts which increase product selectivity by even a few percentage points can significantly reduce costs and improve process sustainability.

The discovery of heterogeneous catalysts has had a monumental impact on society in the past several decades. For instance, in 1908 Fritz Haber reported the discovery of a catalyst which

enabled the synthesis of ammonia from elemental N_2 and H_2.[5] Prior to this finding, reactive nitrogen was primarily mined from depleting salt and coal reservoirs.[6] The scarcity and costly extraction of reactive nitrogen rendered many nitrogen-based chemicals a luxury. The advent of large-scale catalytic production of ammonia (also known as the Haber-Bosch process) significantly drove down the cost of reactive nitrogen and paved the way for the industrial scale production of many nitrogen-based compounds, most importantly including crop fertilizers. The modern day scale of the Haber-Bosch process is so profound that it is estimated that nearly 1% of the total global energy produced yearly is consumed by this process.[7] Furthermore, it is argued that approximately 27% of the world's population in the 20th century (4 billion people) was supported by Haber-Bosch ammonia-derived fertilizer.[6]

In addition to the discovery of the ammonia synthesis catalyst, the 20th century also witnessed the development and widespread integration of the automotive catalytic converter for exhaust pollution mitigation.[8,9] The large scale adoption of gasoline-powered vehicles combined with increasing urbanization resulted in significant accumulation of pollution from vehicle emissions. The catalytic converter, a device consisting of metal nanoparticle catalysts supported on aluminum oxide, was introduced to motor vehicles to chemically convert unburned gasoline, toxic carbon monoxide, and nitrogen oxides into relatively benign compounds such as water, nitrogen, and carbon dioxide. This significantly improved air quality particularly in large metropolitan areas of the United States in the late 20th century. The success of the catalytic converter for emissions control led to the integration of the device in nearly all gasoline-powered automobiles manufactured in 1975 and onwards in the United States.

Beyond ammonia synthesis and emissions control, heterogeneous catalysis plays a key role in the production of many other chemicals and materials including sulfuric acid (the highest

volume commodity chemical produced in the US), ethylene, propylene, benzene, acetic acid, and many more.[10] The challenge moving forward in the field of heterogeneous catalysis is centered on the discovery of new catalytic materials that can approach 100% efficiency in the conversion of reactants to desired products. A particularly important and versatile class of catalytic materials for performing highly-selective chemical catalysis are nanostructured metals supported on high surface area oxide supports. In the following sections, we will discuss physical characteristics of these materials which make them of widespread interest in catalysis research and discuss the mechanisms of chemical bond activation on metal surfaces.

1.3 Metal Nanoparticle Catalysts

The catalytic properties of metal nanoparticles emerge from the relatively high energy of metal surface atoms.[11] If we consider a metal nanoparticle of arbitrary shape, there are essentially two types of metal atoms in this structure: bulk metal atoms which are completely surrounded by other metal atoms (i.e. highly-coordinated) and surface metal atoms which are bonded with underlying metal atoms but lacking chemical bonds at the surface (i.e. under-coordinated). This deficiency of chemical bonds experienced by metal surface atoms renders them higher in energy and more likely to seek out other atoms with which to share electron density and create chemical bonds. When a metal surface atom creates a chemical bond with a molecule, the bonds in the molecule become weaker making it easier to break those bonds. Furthermore, once bonds in a molecule break, adjacent metal surface atoms can chemically bond with the resulting fragments thereby stabilizing those fragments. These chemical fragments can then react with other chemical fragments on the metal surface and eventually desorb resulting in the synthesis of a new molecule. In this way, metal surface atoms facilitate chemical reactions (i.e. the making and breaking of chemical bonds).

Given the importance of metal surface atoms for catalysis, the synthesis of metal nanoparticle catalysts has been aimed at maximizing the availability of metal surface atoms per mass of the metal. Metal nanoparticle catalysts are typically synthesized using a technique known as wet impregnation.[12] This method involves physically mixing a metal precursor (solvated metal ions or transition metal complexes) with a metal oxide support material such as SiO_2, Al_2O_3, ZrO_2, TiO_2, and others. The metal precursor anchors onto the oxide support and is then dried and treated at high temperatures to decompose/reduce the metal precursor into small metal nanoparticles on the metal oxide support.[13] The end result is a catalyst of small metal nanoparticles with clean surfaces which provides the largest number of metal surface sites per mass of metal for surface chemistry (Figure 1.1).

| Metal nanoparticles supported on fumed SiO_2 | Electron micrograph of metal nanoparticles | Atomistic depiction of a metal nanoparticle |
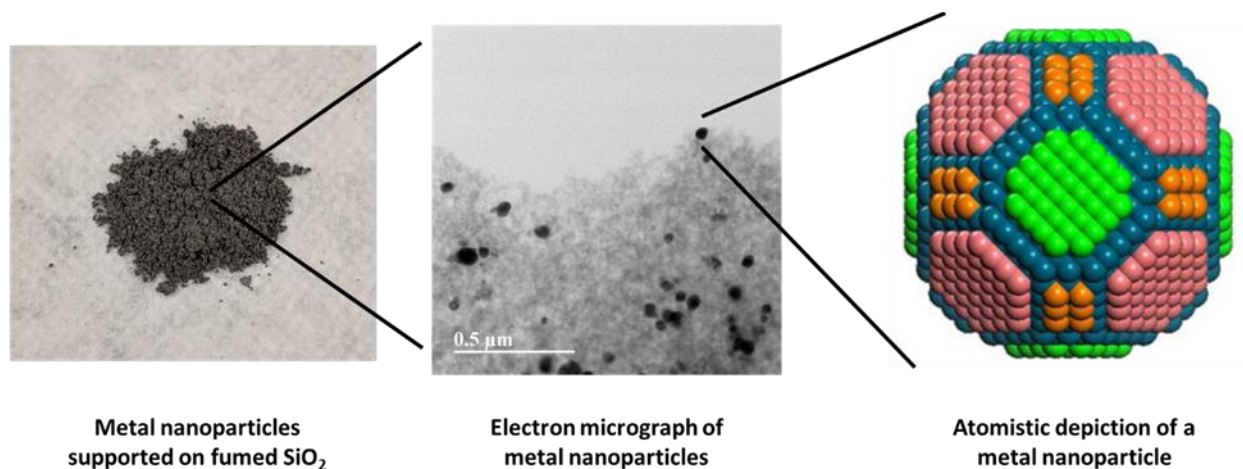
Figure 1.1 Supported metal nanoparticle catalysts. A picture of metal nanoparticles supported on fumed SiO_2 prepared using the wet impregnation technique. The individual metal nanoparticles formed on the metal oxide support can be viewed under an electron microscope. The inert oxide support facilitates the dispersion of the metal nanoparticles so surface area is not lost from aggregation of nanoparticles. The atomistic depiction of a metal nanoparticle emphasizes the heterogeneity of the metal surface which can express many different crystal facets.

The ultimate effectiveness of a catalyst is primarily accessed based on two metrics: the chemical activity for a specified reaction and the selectivity towards the desired reaction products. The activity of a catalyst is a measure of the rate at which reactants are converted to products per mass (or surface area) of the catalyst. The catalysts which produce the highest activities are those

that bind the relevant reactants "not too strongly or too weakly".[14] Weak binding of the reactant (or adsorbate) with the surface may not be sufficient for activating chemical bonds of the reactant whereas strong binding may make it very difficult to desorb the product once formed.

The chemical reactivity (i.e. the propensity to form strong chemical bonds) of a metal can be tuned in many different ways. One of the most versatile methods for tuning the chemical reactivity of metal surfaces is by alloying of two or more metals.[15,16] The chemical reactivity of transition metals generally correlates with the filling of the d-orbitals for a specific metal. Cu, Ag, and Au are all d^{10} metals and thus have completely full d-states. This characteristic of the metals makes them the least chemically reactive of the transition metals.[17] As we move to the left across the periodic table, the filling of the d-states of the transition metals decreases and the chemical reactivity of the metals in general increases. Given these inherent differences in chemical reactivity of transition metals, the reactivity of a given metal can be modified by combining the metal with another transition metal to make bimetallic nanoparticles.

While the catalyst activity has largely been the center of attention in catalyst research, the focus has increasingly shifted toward catalyst selectivity in the past several decades.[18] The selectivity of a catalyst is defined as the fraction of reactants converted to the desired product relative to the total amount of reactants converted to all products. Catalytic processes that produce low or even moderate product selectivities are often too costly and environmentally unsustainable, particularly for large scale processes. The production of unselective chemical by-products not only wastes a portion of the reactant feedstock but also must be separated from the desired product and disposed of in an environmentally benign way. For these reasons, the best catalyst for a given chemical conversion should display high chemical activity and ideally produce 100% selectivity towards the desired product. The unintentional production of chemical by-products (i.e. low

selectivity) is in large part a consequence of inadvertently activating chemical bonds of adsorbates that favor unselective reaction pathways. To understand why this is the case, we review the activation of chemical bonds on metal surfaces in the following section.

1.4 Activation of chemical bonds on metal surfaces

The catalytic transformation of chemical species on metal surfaces involves multiple elementary steps which can include adsorption, surface diffusion, chemical bond breakage or formation, and desorption.[19] In order for these elementary steps to take place, additional energy needs to be supplied to overcome an energetic activation barrier for the process. To illustrate this point, let's consider the dissociation of a diatomic molecule on a metal surface. The potential energy surface for the dissociation reaction can be approximated as a Lennard-Jones potential, as depicted in Figure 1.2a) where the equilibrium starting position of the adsorbate is at the bottom of the well (i.e. at the ground state vibrational energy).[20] In order for the molecule to dissociate, it must climb the vibrational energy ladder and overcome the activation barrier for dissociation. The vibrational energy distribution of the adsorbate is governed by a Boltzmann distribution which suggests that the population of vibrationally excited (i.e. vibrational energy levels above the ground state) molecules increases with temperature.[21] Thus, to increase the probability of reaction, vibrational energy is pumped into adsorbates by adding heat to the system. This excites vibrational modes of the molecules and phonon modes (collective lattice vibrations) of the metal. Phonon modes of the metal can then couple with molecular vibrations of the adsorbate to drive additional energy into the adsorbate thereby inducing the reaction.
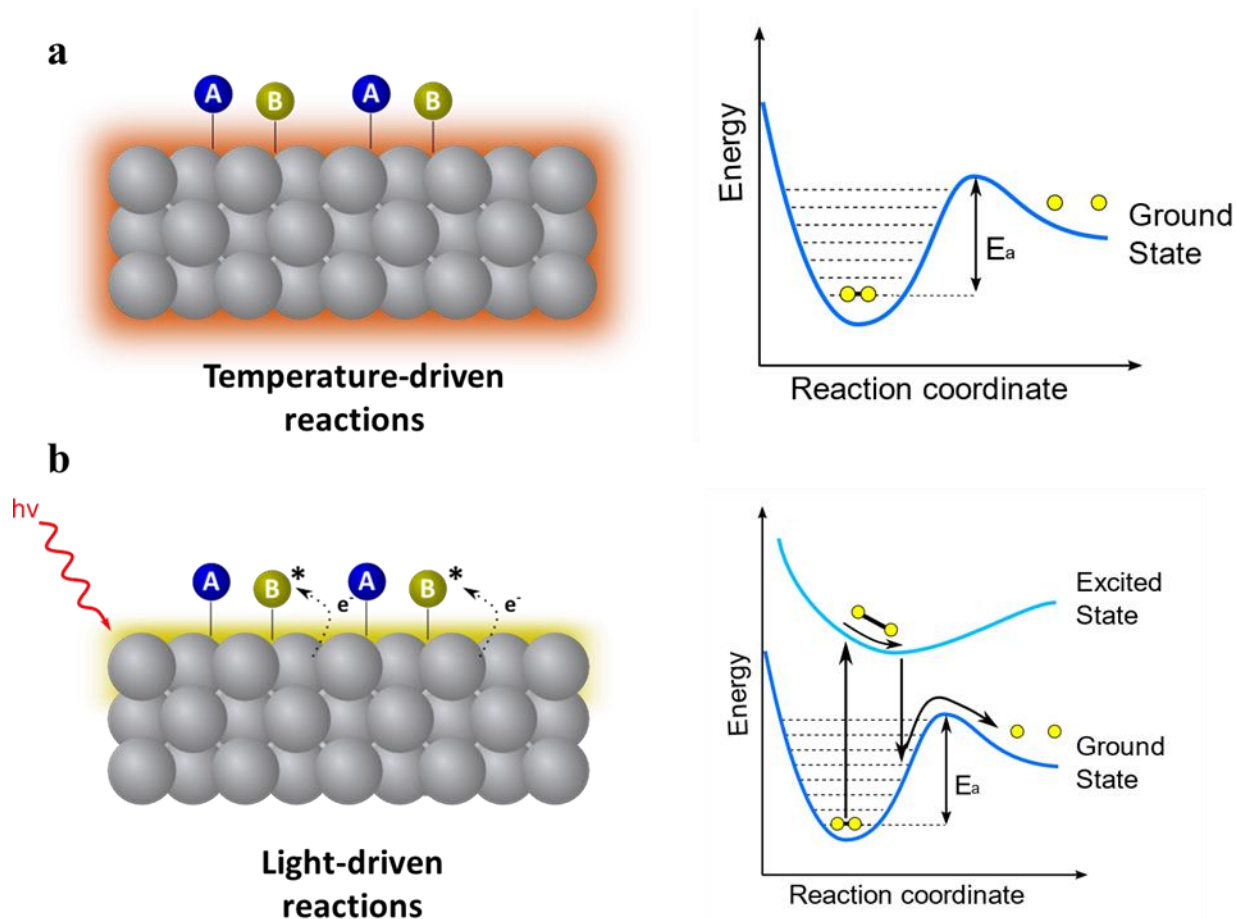
Figure 1.2 Activation of chemical reactions on metal surfaces. (a) Temperature-driven reactions. In order to activate chemical bonds on metal surfaces, energy is provided to the system in the form of heat. This results in the indiscriminate thermal excitation of all vibrational modes of all adsorbates and materials in the reactor. The additional vibrational energy gained by adsorbates increases the probability of reaction by pushing the adsorbate up the vibrational ladder (depicted as dashed lines in the potential well). **(b)** Light-driven (or charge carrier-driven) reactions. The photoexcitation of energetic charge carriers at the adsorbate-metal interface can excite a molecule from the electronic ground state to an excited state. The molecule evolves along this excited state potential energy surface to accommodate the additional energy. The molecule then returns to the ground state with additional vibrational energy thereby increasing the likelihood of overcoming the activation barrier for reaction.

In cases where there is only one viable reaction pathway, there are not many downsides to temperature-driven chemical bond activation on metal surfaces. However, when multiple chemical adsorbates are involved and several reaction outcomes are possible, an unavoidable side effect of this approach is that energy is unselectively deposited into every available vibrational mode of all adsorbates on the surface of the metal. This can result in the simultaneous activation of other, unselective reaction pathways leading to the undesirable formation of by-products and chemical waste.

Several strategies have emerged for improving selectivity in these temperature-driven chemical reactions. For example, some research has focused on identifying highly selective surface facets or active sites of a known catalyst and developing methods for synthesizing metal nanoparticles which predominately express those selective surface sites. Christopher et al. took this approach to develop Ag catalysts with inherently higher selectivity in the partial oxidation of ethylene to ethylene oxide.[22] Based on a mechanistic understanding of the elementary steps which control product selectivity, they identified Ag(100) surface sites as the most selective sites for the partial oxidation of ethylene. Cubic Ag nanoparticles were synthesized to maximize the availability of Ag(100) sites relative to all other surface facets and displayed markedly higher ethylene oxide selectivity. Other strategies for improving product selectivity include, tailoring the chemical reactivity of a metal surface to favor a particular reaction pathway, deliberately poisoning unselective active centers, and sterically hindering adsorption of molecules to limit access to certain chemical bonds.[23–25] All these tactics have shown some success but still fight against the fundamental limitation of indiscriminate energy transfer to all molecular vibrations and the resulting activation of multiple reaction pathways in temperature-driven catalysis.

An alternative mechanism for activating chemical bonds on metal surfaces involves the excitation of energetic charge carriers (typically via photoexcitation) at the metal-adsorbate interface.[26–29] The mechanism of charge carrier-mediated bond activation on metal surfaces was originally uncovered through studies using high-powered lasers to excite energetic charge carriers in bulk metal surfaces.[30,31] In this mechanism, the photoexcitation of charge carriers at the adsorbate-metal interface results in the excitation of the adsorbate to a charged or excited state (Figure 1.2b). This transfer of energy to the molecule forces the molecule to evolve along a charged (or excited) potential energy surface (i.e. the atoms of in the molecule reconfigure to accommodate the energy). Once the charged (or excited) state decays, the molecule returns to the ground state potential energy surface but with additional vibrational energy.

It is important to stress that this process does not require charge extraction out of the metal (i.e. the metal nanoparticle does not end up in a charged state). This process only leads to a transient electronic exchange between the metal and reactant, yielding transient adsorbate ions or excited states. These adsorbate ions survive on metal surfaces tens of picoseconds before the relaxation of the electronic excitation is transferred back to the metal. This mechanism of bond activation is known in the surface chemistry community as desorption induced by electronic transitions (DIET), where the reference to desorption comes from the fact that the initial reports of laser-induced surface chemistry were focused on desorption from metal surfaces.[30]

In contrast to temperature-driven activation of chemical bonds, this mechanism makes it possible to selectively provide energy to specific adsorbates by using photons that only target excitations associated with the desired adsorbates. By only allowing for energy to be transferred to select chemical bonds, it is possible to mitigate the production of by-products by pushing the chemical transformation of reactants predominantly along the desired reaction pathway. Although

this mechanism of activating chemical bonds on metal surfaces generated some excitement in the surface chemistry community, the need to use high intensity lasers on bulk metal surfaces made this mechanism of activating chemical reactions generally impractical for technological applications such as heterogeneous catalysis. However, in recent years it has been shown that nanoparticles made of plasmonic metals can perform charge carrier-mediated reactions under low intensity visible light illumination.[32–34] These findings on nanostructured, plasmonic metal catalysts have reignited interest in charge carrier-mediated transformations on metal surfaces and led to the emergence of a vibrant, new area of research in heterogeneous catalysis known as plasmonic catalysis.

1.5 Scope of Dissertation

When I began my doctoral dissertation in 2013, plasmonic catalysis was a relatively new field with nearly all studies focused on nanoparticles of Cu, Ag, and Au for driving plasmon-enhanced chemical reactions. We were interested in expanding the field beyond surface chemistry that could take place only on these three materials. In particular, we focused on answering the question – can we combine the optical properties of plasmonic metals (Cu, Ag, and Au) with the catalytic properties of other, catalytically-relevant materials? The objective of this dissertation is to develop a fundamental understanding of the energy transfer processes at work in multicomponent plasmonic materials and to use this understanding to guide the design of plasmonic catalysts for catalytic transformations beyond those that can be performed by the plasmonic metals. To do this, we considered the case of bimetallic nanoparticles containing a plasmonic metal (Ag) and a catalytic metal (Pt). Synthesis techniques were developed for fabricating bimetallic nanoparticles of these materials in two distinct architectures: alloy nanoparticles in which both metals were completely mixed, and core-shell nanoparticles in which

a large Ag core was surrounded by an ultra-thin Pt shell. We perform detailed characterization and reactor studies of these materials to uncover the mechanism for the transfer of energy from photoexcited plasmonic metals to other catalytic materials. The chapters of this dissertation are organized a follows.

In chapter 2, essential background information on plasmonic catalysis is covered in detail. In particular, the physical characteristics of plasmonic nanostructures enabling charge carrier-mediated chemical transformations to take at low intensities are outlined. These characteristics include the excitation of localized surface plasmon resonance, photon absorption pathways in metals, and excitation/relaxation of energetic charge carriers in metals. We then discuss the mechanisms by which energy can be transferred from photoexcited plasmonic metals to chemically attached materials. Finally, the chapter concludes with a discussion on the limitations of plasmonic catalysis and our rationale for focusing on the design of bimetallic Ag-Pt nanoparticles to understand energy flow in multicomponent plasmonic nanoparticles.

In chapter 3, the experimental and theoretical methods and tools used to carry out the work presented in the dissertation are described. Strong emphasis will be placed on nanoparticle synthesis techniques as the development of novel synthesis methods for new materials sets the foundation for drawing meaningful conclusions from experiments in this dissertation. Characterization tools used to study the optical and catalytic properties of materials as well as the design of reactor experiments will also be discussed.

In chapter 4, we set out to develop a synthesis method for creating well-mixed Ag-Pt bimetallic alloy nanoparticles. We outline the challenges of forming alloy nanoparticles of immiscible metals and strategies for overcoming those challenges. By borrowing aspects of previously successful methods for synthesizing alloy nanoparticles and leveraging the optical

properties of Ag, we invent a creative synthesis approach designed to coerce the mixing of Ag and Pt atoms into a single, kinetically-stable alloy nanostructure. We characterize the nanoparticles at several stages of the synthesis and discuss the advantages and disadvantages of the newly-discovered synthesis.

In chapter 5, we turn our attention to developing a highly-scalable synthesis for coating large Ag nanoparticles with ultra-thin shells of Pt. We hypothesize that coating a thin layer of Pt onto large Ag nanoparticles should allow for the creation of hybrid plasmonic nanoparticles which manifest the optical properties of Ag while displaying the surface chemical properties of Pt. We outline obstacles in the synthesis of core-shell nanoparticles with ultra-thin shells and formulate a unique approach for surmounting these obstacles. We focus on seed-mediated syntheses in which Pt is slowly coated on the surface of Ag nanoparticles. We explore methods aimed to tailor the reactivity of Pt metal precursors through ligand exchange. We then use spectroscopic tools to characterize the optical and surface chemical properties of the nanostructures to assess whether the Ag-Pt nanoparticles express the hybrid optical-catalytic properties we desire.

In chapter 6, we employ our newly-discovered Ag-Pt core-shell nanoparticles as platforms to study the underlying physical mechanisms governing energy flow from plasmonic metals to other, catalytically-relevant transition metals. We probe the flow of energy in these materials using a combined experimental and theoretical approach. Optical integrating sphere spectroscopy combined with UV-vis transmission spectroscopy allow us to study changes in the optical properties of Ag nanoparticles when coated with a thin layer of Pt. These experiments show that the thin layer of Pt results in a drastic change in the optical properties of the nanoparticles. Electrodynamic simulations are used to augment the spectroscopic experiments and show that

most of the energy captured by the plasmonic Ag core in directed into the thin coating of Pt at the surface.

In chapter 7, we test whether the funneling of plasmonic energy from the Ag core to the Pt shell of the nanoparticles can be used to perform plasmonic catalysis on the surface of non-plasmonic metals. We design reactor studies focusing on the preferential oxidation of carbon monoxide in excess hydrogen. The results of variable temperature photoreactor studies demonstrate that the rate of the reaction can be accelerated by shining low intensity visible light on the catalyst. A series of mass spectrometry, diffuse reflectance UV-vis spectroscopy and wavelength-dependent reactor experiments build strong evidence that plasmon excitation of the Ag core is directly responsible for the enhanced rates of reaction observed under visible light illumination. We discuss the implications of these results for the future design of multicomponent plasmonic catalysts.

In chapter 8, we conclude by summarizing the main findings of this dissertation. A perspective of the current state of the field and opportunities for future advancements are also discussed.

1.6 References

1. Roberts, L. 9 Billion? *Science* **333,** 540–543 (2011).

2. Chu, S., Cui, Y. & Liu, N. The path towards sustainable energy. *Nat Mater* **16,** 16–22 (2017).

3. Somorjai, G. A. & Rioux, R. M. High technology catalysts towards 100% selectivity: Fabrication, characterization and reaction studies. *Catalysis Today* **100,** 201–215 (2005).

4. Somorjai, G. A. & Park, J. Y. Molecular Factors of Catalytic Selectivity. *Angewandte Chemie* **47,** 9212–9228 (2008).

5. Ertl, G. Elementary Steps in Heterogeneous Catalysis. *Angewandte Chemie* **29,** 1219–1227 (1990).

6. Erisman, J. W., Sutton, M. A., Galloway, J., Klimont, Z. & Winiwarter, W. How a century of ammonia synthesis changed the world. *Nature Geosci* **1,** 636–639 (2008).

7. Abstracts | U.S. DOE Office of Science (SC). Available at: https://science.energy.gov/bes/community-resources/reports/abstracts/#Ammonia. (Accessed: 18th May 2018)

8. Taylor, K. C. Automobile Catalytic Converters. in *Catalysis* 119–170 (Springer, Berlin, Heidelberg, 1984).

9. Bell, A. T. The Impact of Nanoscience on Heterogeneous Catalysis. *Science* **299,** 1688–1691 (2003).

10. Frontmatter. in *Handbook of Heterogeneous Catalysis* (eds. Ertl, G., Knözinger, H. & Weitkamp, J.) I–XIX (Wiley-VCH Verlag GmbH, 1997).

11. Hammer, B. & Nørskov, J. K. Theoretical surface science and catalysis—calculations and concepts. in *Advances in Catalysis* (ed. Bruce C. Gates, H. K.) **45,** 71–129 (Academic Press, 2000).

12. Lee, S.-J. & Gavriilidis, A. Supported Au Catalysts for Low-Temperature CO Oxidation Prepared by Impregnation. *Journal of Catalysis* **206,** 305–313 (2002).

13. Soled, S. Silica-supported catalysts get a new breath of life. *Science* **350,** 1171–1172 (2015).

14. Medford, A. J. *et al.* From the Sabatier principle to a predictive theory of transition-metal heterogeneous catalysis. *Journal of Catalysis* **328,** 36–42 (2015).

15. Nørskov, J. K., Bligaard, T., Rossmeisl, J. & Christensen, C. H. Towards the computational design of solid catalysts. *Nat Chem* **1,** 37–46 (2009).

16. Cleve, T. V., Moniri, S., Belok, G., More, K. L. & Linic, S. Nanoscale Engineering of Efficient Oxygen Reduction Electrocatalysts by Tailoring the Local Chemical Environment of Pt Surface Sites. *ACS Catal.* **7,** 17–24 (2017).

17. Hammer, B. & Norskov, J. K. Why gold is the noblest of all the metals. *Nature* **376,** 238–240 (1995).

18. Somorjai, G. A. & McCrea, K. Roadmap for catalysis science in the 21st century: a personal view of building the future on past and present accomplishments. *Applied Catalysis A: General* **222,** 3–18 (2001).

19. Chorkendorff, I. & Niemantsverdriet, J. W. *Concepts of Modern Catalysis and Kinetics.* (John Wiley & Sons, 2017).

20. Linic, S., Aslam, U., Boerigter, C. & Morabito, M. Photochemical transformations on plasmonic metal nanoparticles. *Nat Mater* **14,** 567–576 (2015).

21. Boerigter, C., Aslam, U. & Linic, S. Mechanism of Charge Transfer from Plasmonic Nanostructures to Chemically Attached Materials. *ACS Nano* **10,** 6108–6115 (2016).

22. Christopher, P. & Linic, S. Shape- and Size-Specific Chemistry of Ag Nanostructures in Catalytic Ethylene Epoxidation. *ChemCatChem* **2,** 78–83 (2010).

23. Studt, F. *et al.* Identification of Non-Precious Metal Alloy Catalysts for Selective Hydrogenation of Acetylene. *Science* **320,** 1320–1322 (2008).

24. Linic, S., Jankowiak, J. & Barteau, M. A. Selectivity driven design of bimetallic ethylene epoxidation catalysts from first principles. *Journal of Catalysis* **224,** 489–493 (2004).

25. Zhang, J., Wang, B., Nikolla, E. & Medlin, J. W. Directing Reaction Pathways through Controlled Reactant Binding at Pd–TiO2 Interfaces. *Angewandte Chemie* **129,** 6694–6698 (2017).

26. Lindstrom, C. D. & Zhu, X.-Y. Photoinduced Electron Transfer at Molecule−Metal Interfaces. *Chem. Rev.* **106,** 4281–4300 (2006).

27. Frischkorn, C. & Wolf, M. Femtochemistry at Metal Surfaces: Nonadiabatic Reaction Dynamics. *Chem. Rev.* **106,** 4207–4233 (2006).

28. White, J. M. Using photons and electrons to drive surface chemical reactions. *Journal of Molecular Catalysis A: Chemical* **131,** 71–90 (1998).

29. Busch, D. G. & Ho, W. Direct Observation of the Crossover from Single to Multiple Excitations in Femtosecond Surface Photochemistry. *Phys. Rev. Lett.* **77,** 1338–1341 (1996).

30. Ageev, V. N. Desorption induced by electronic transitions. *Progress in Surface Science* **47,** 55–203 (1994).

31. Bonn, M. *et al.* Phonon- Versus Electron-Mediated Desorption and Oxidation of CO on Ru(0001). *Science* **285,** 1042–1045 (1999).

32. Christopher, P., Xin, H. & Linic, S. Visible-light-enhanced catalytic oxidation reactions on plasmonic silver nanostructures. *Nat Chem* **3,** 467–472 (2011).

33. Mukherjee, S. *et al.* Hot Electrons Do the Impossible: Plasmon-Induced Dissociation of H2 on Au. *Nano Lett.* **13,** 240–247 (2013).

34. Marimuthu, A., Zhang, J. & Linic, S. Tuning Selectivity in Propylene Epoxidation by Plasmon Mediated Photo-Switching of Cu Oxidation State. *Science* **339,** 1590–1593 (2013).

Chapter 2 Essential Background for Plasmonic Catalysis

2.1 Summary

This chapter provides a review of plasmonic catalysis. We start by introducing plasmonic metal nanoparticles and the excitation of localized surface plasmon resonance. We discuss the physical characteristics of metals that allow for plasmon excitation and various plasmon relaxation pathways in isolated, monometallic plasmonic nanoparticles. In particular, we focus on plasmon-induced absorption (i.e. the excitation of energetic charge carriers) in metal nanoparticles. This includes the various absorption channels in metals, initial excitation of charge carriers, and relaxation of energetic charge carriers. We then delve into the activation of chemical bonds on photoexcited plasmonic metal nanoparticles and mechanisms by which energy can be transferred from plasmons to adsorbates. This is followed by a discussion on the limitations of plasmonic catalysis with particular focus on the limitations imposed by monometallic nanoparticles. The chapter concludes by considering the possibility of alleviating these restrictions through the design of multicomponent plasmonic nanomaterials.

2.2 Plasmonic metal nanoparticles

Plasmonic metal nanoparticles are light-harvesting materials that interact strongly with visible light through the excitation of localized surface plasmon resonance (LSPR).[1,2] LSPR is established when light of wavelengths much longer than the size of the metal nanoparticles causes

a resonant, collective oscillation of the free electrons in the metal nanoparticles. This physical process allows the nanoparticles to collect the energy of visible light, concentrate it near the surface of the particles, and convert light energy into the energy of excited charge carriers. We present a detailed discussion of these processes in the following sections.

2.2.1 Plasmon excitation

A key characteristic of plasmon excitation is a large optical extinction cross section of the metal nanoparticles at resonant frequencies.[3,4] At these frequencies, the extinction cross-section of plasmonic nanoparticles can be up to 10 times their geometric cross-section.[5] This produces an antenna effect whereby photons not directly in the path of the particles can nevertheless interact with the nanoparticles through LSPR excitation. Assuming Mie theory for a spherical nanoparticle, the extinction cross section (σ_{ext}) is related to the complex dielectric function of the metal as follows

$$\sigma_{ext} \sim \frac{\varepsilon_2}{[\varepsilon_1 + 2\varepsilon_m]^2 + \varepsilon_2^2} \quad \text{(equation 1)}$$

where ε_1 is the real part of the dielectric function of the metal, ε_2 is the imaginary part of the dielectric function of the metal, and ε_m is the dielectric constant of the medium.[6] This relationship allows us to identify physical criteria that must be satisfied for a metal to undergo plasmon excitation. It is clear that the extinction cross section is the largest as the denominator approaches zero. This stipulates that $\varepsilon_1 \approx -2\varepsilon_m$ and ε_2 should be very small for plasmon excitation to occur. The real part of the dielectric function (ε_1) describes the polarizability of the metal with respect to wavelength and is generally negative for metals across a wide range of frequencies. The value of ε_1 as a function of wavelength as well as ε_m of air is plotted in Figure 2.1a. From these data, it can

be seen that the first condition for plasmon excitation ($\varepsilon_1 \approx -2\varepsilon_m$) can be established for many metals in air at UV-visible frequencies.

The imaginary part of the dielectric function (ε_2) is directly related to the probability for photon absorption in the metal at a particular frequency (Figure 2.1b). This physical property of metals is inextricably linked to their electronic structure. Transition metals are generally characterized by a half-filled s-band and a partially-filled d-band. There are two types of electronic excitations that can take place in these materials. The first are excitations from filled s-states below the Fermi level to empty s-states above the Fermi level, known as intraband excitations. These excitations are generally available for all transition metals in the visible range. The second are excitations from filled d-states below the Fermi level to empty s-states above the Fermi level, known as interband excitations. The availability of these transitions in the visible range depends on the location of the d-states in each metal relative to the Fermi level. For instance, Ag is characterized by a full d-band that lies well-below the Fermi level (Figure 2.1c). Consequently, d-to-s interband excitations cannot be induced by visible light photons in Ag which results in a low value of ε_2 throughout the visible range. Au and Cu are also characterized by a full d-band which lies below the Fermi level (Figure 2.1c), but visible light photons above a specific threshold energy are able to induce interband excitations in these metals which translates to higher values of ε_2 at short visible light wavelengths. In contrast to the noble metals, where we define noble metals as metals with completely filled d-states, the d-states for the non-noble transition metals are not completely full and intersect the Fermi level (Figure 2.1c). As a result, these metals can absorb photons via interband excitations throughout the visible range, and consequently, have high ε_2 in the visible region. This feature of the imaginary part of the dielectric function for non-noble transition metals compromises their ability to undergo plasmon excitation in the visible range and

results in small extinction cross sections for nanoparticles of these metals. The combination of ε_1 ≈ -2ε_m and low ε_2 is why Ag, Au and Cu exhibit LSPR in the visible range and are typically regarded as the "plasmonic" metals.
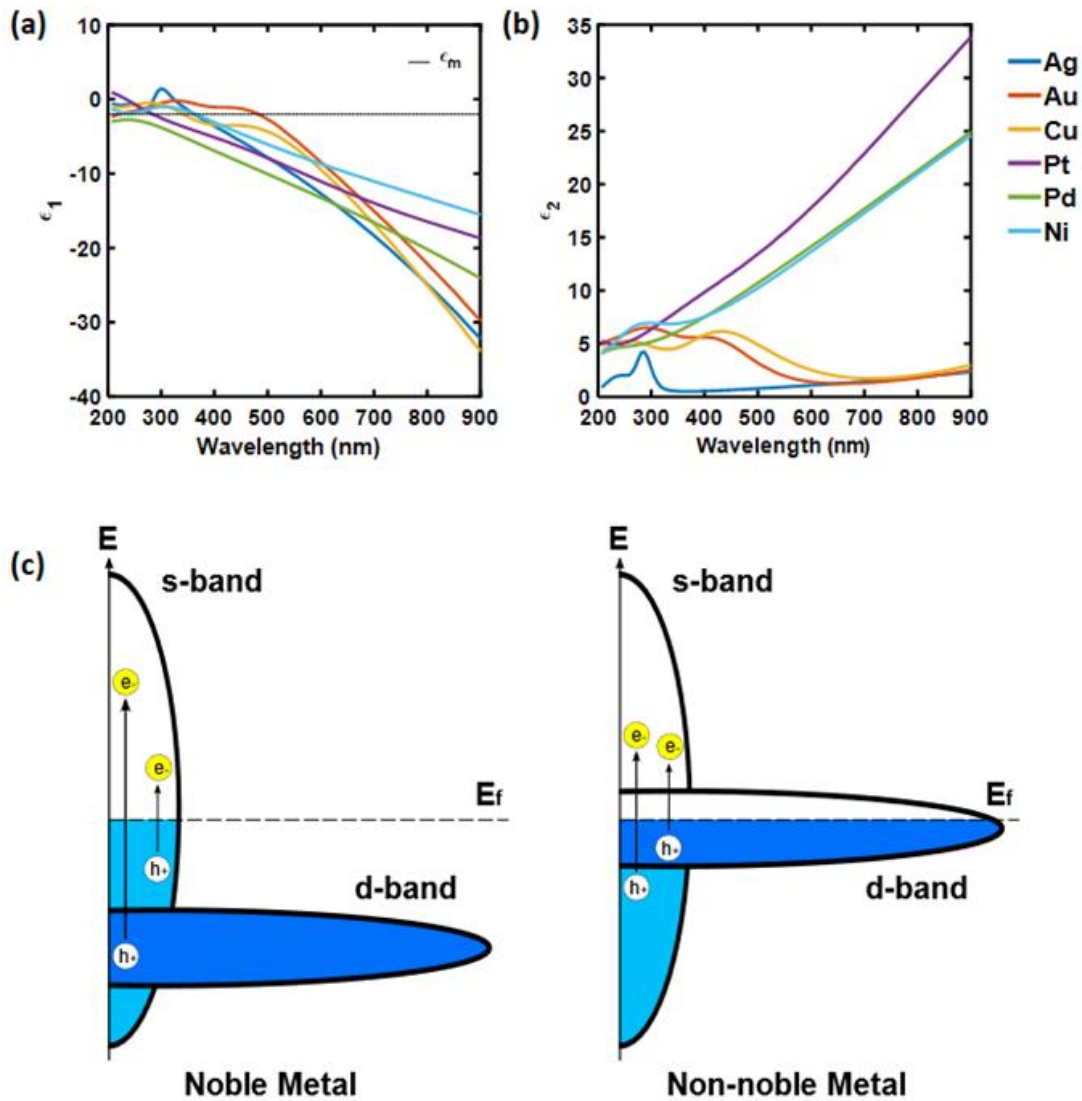
Figure 2.1 Optical properties of metals. (a) The real part of the dielectric function for the plasmonic metals (Ag, Cu, Au) and other transition metals. The black dotted line represents ε_m for air. **(b)** The imaginary part of the dielectric function for the plasmonic metals and other transition metals. **(c)** Sketches of the representative density of states of a plasmonic metal (left) and a typical transition metal (right). Intraband s-to-s transitions are low energy transitions and are accessible with visible light photons for both groups metals. However, because the d-band lies far before the Fermi level (E_f) for plasmonic metals, only high energy photons can induce interband d-to-s excitations for these metals. In the case of non-noble metals, the d-band intersects E_f allowing for d-to-s excitations to take place throughout the visible range.

2.2.2 Field confinement and plasmon decay

A direct consequence of plasmon excitation is the confinement of light energy near the surface of metal nanoparticles in the form of elevated electric fields.[7] The distribution of the confined electric fields in the metal is spatially inhomogeneous with the maximum field intensities localized at the surface of the nanoparticles.[8] The intensity of these fields decay dramatically with distance from the surface. For isolated particles, the elevated field intensities can be up to 10^2 times the intensity of the incoming electromagnetic field and up to 10^3 times the intensity at corners or other sharp features of the nanoparticles.[9] Furthermore, the field confinement can reach 10^4-10^6 times the intensity of incoming radiation in the space between two closely positioned plasmonic nanoparticles. These regions of extremely high field intensities are commonly referred to as plasmonic "hot spots". The amplification of the electric field intensity near the surface of the nanoparticles can then be used to amplify other photophysical processes such as absorption (i.e. excitation of electrons/holes) and photon scattering. A classic example of this is the amplification of inherently weak Raman scattering from photoexcited molecular vibrations in surface-enhanced Raman spectroscopy (SERS).[10–12] The confinement and concentration of incoming electromagnetic radiation by plasmonic nanoparticles has been shown to allow for the detection of even single molecules in SERS.[13–15]

For the case of isolated plasmonic nanoparticles, the energy stored in the elevated fields can be dissipated either radiatively via photon scattering or non-radiatively via absorption in the metal nanoparticles.[16,17] Non-radiative absorption results in the generation of energetic charge carriers near the surface of the metal nanoparticles which can then be extracted to perform a specific function.[18,19] As discussed earlier, absorption (i.e. the generation of energetic charge carriers) in metals can occur through either intraband s-to-s excitations or interband d-to-s

excitations (Figure 2.2a). The s-to-s excitations are indirect electronic excitations that require involvement of a third entity to provide the necessary change in the momentum of the charge carriers. This change in momentum can be supplied by lattice phonons or collisions with the nanoparticle surface. Because these excitations require a change in momentum, intraband excitations exhibit a relatively small characteristic rate constant of $\sim 10^{13}$ s^{-1}.[20] In the case of the d-to-s interband excitations, no change in the momentum of the charge carriers is required resulting in a larger characteristic rate constant for these excitations of $\sim 10^{15}$ s^{-1}. Due to the inherently larger rate constant of interband excitations, plasmon decay via these excitations is expected to be the dominant decay pathway when available. This was recently shown to be the case from first principles by Atwater et al.[21] The data in Figure 2.2b show the partitioning of various absorption pathways in plasmonic gold nanoparticles vs plasmon energy. These data show that direct interband excitations quickly become the dominant pathway for photon absorption in Au once they become energetically accessible regardless of nanoparticle size. The contribution of the other absorption processes (phonon-assisted or surface-assisted intraband excitations) are size-dependent and only dominate for plasmon energies at which direct interband transitions are inaccessible.
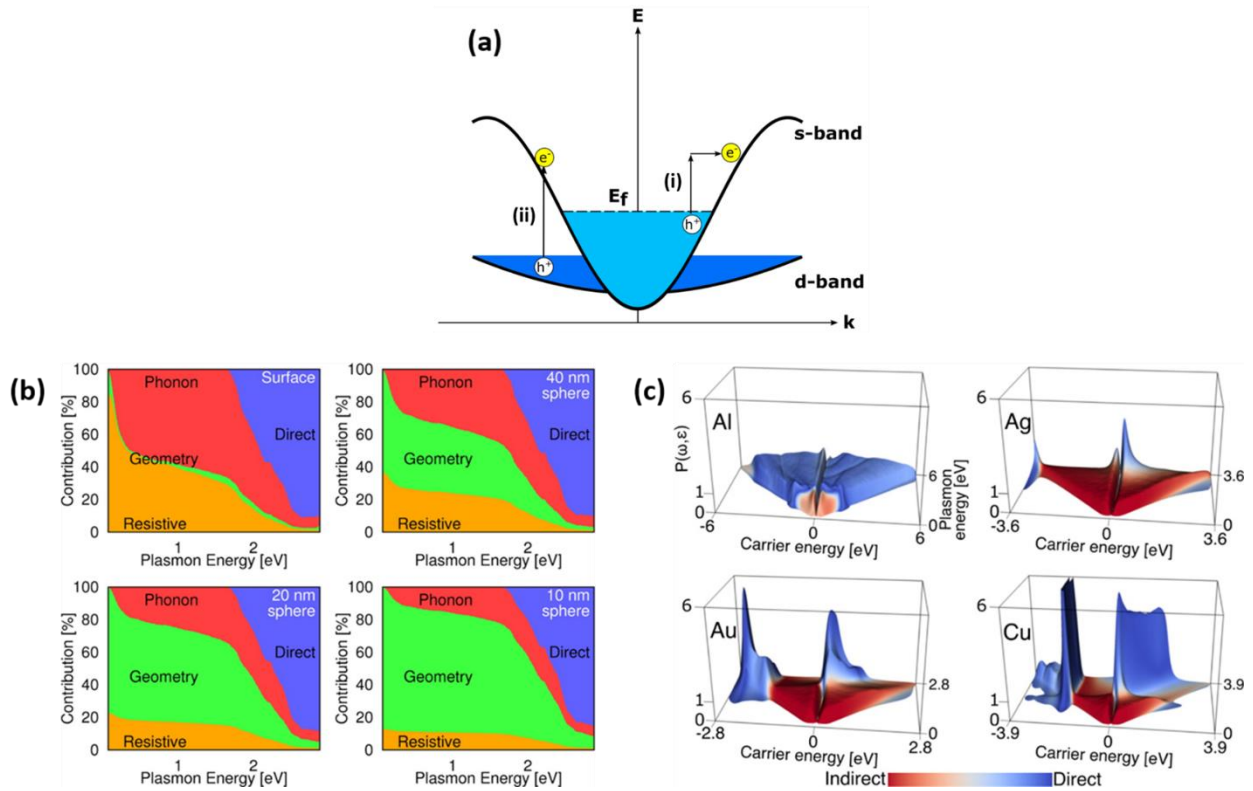
Figure 2.2 Excitation of energetic charge carriers in plasmonic metals. (a) Band diagram depiction of photon absorption in metals. The x-axis represents momentum space (also known as k space). Momentum space essentially represents the various configurations of electrons in orbitals for a solid state material. The two types of excitations that can take place in metals are (i) indirect s-to-s intraband excitations or (ii) d-to-s interband excitations. **(b)** Relative contributions of resistive, geometry-assisted, phonon-assisted, and direct excitations to absorption in a semi-infinite gold surface and spherical gold nanoparticles of various sizes as a function of plasmon energy. Direct excitations in Au dominant when available regardless of the size of the Au particles. **(c)** Energy distributions of initially-excited hot carriers ($P(\omega,\varepsilon)$) in Al, Ag, Au, and Cu as a function of plasmon frequency (ω) and carrier energy (ε). Excitation of intraband transitions results in the generation of equally-energetic hot electrons and holes. Excitation of interband transitions generates an asymmetric distribution of low energy electrons and high energy holes. Figure 2.2a was adapted from ref 20. Figures 2.2b and c were taken from ref 21.

The initial energy distribution of the excited charge carriers largely depends on the type of transitions (intraband or interband) that are excited.[22,23] For plasmonic Ag nanoparticles, interband transitions do not overlap with LSPR excitation frequencies. Therefore, plasmon decay in Ag nanoparticles only results in the formation of energetic charge carriers through s-to-s excitations. In contrast, LSPR excitation frequencies for Au and Cu nanoparticles can overlap with interband transitions in the metals. Atwater et al. have shown that the excitation of intraband transitions in Cu, Ag, and Au results in the formation of hot electrons and holes in the s-states of the metals that are of relatively equal energies (Figure 2.2c).[21] In contrast, excitation of interband transitions in Au and Cu results in an asymmetric energy distribution of energetic charge carriers wherein low energy s-electrons and high energy d-holes are produced. This distribution of energetic charge carriers (generated via interband excitations) is a direct consequence of exciting electrons from low-lying filled d-states to empty s-states above the Fermi level of these metals.

These initially-formed high energy charge carriers will quickly lose energy through a number of relaxation processes. These relaxation processes are generally well-understood for energetic charge carriers in the s-states.[24,25] The initially-excited energetic charge carriers primarily lose energy through electron-electron collisions on the fs timescale (Figure 2.3). This results in the secondary excitation of charge carriers near the Fermi level leading to a hot Fermi-Dirac distribution of energetic charge carriers in the s-states. These charge carriers further cool by coupling to phonon modes of the metal nanoparticles ultimately resulting in heating of the metals.
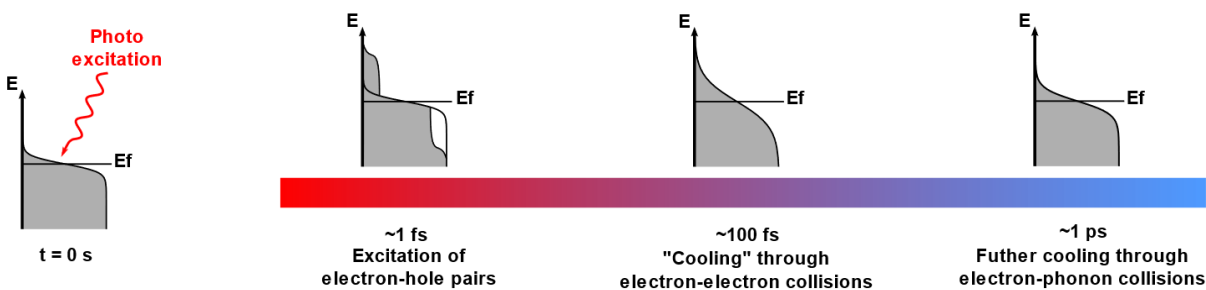
Figure 2.3 Dynamics of energetic charge carriers in metals. Cooling of energetic charge carriers in metals. Plasmon-decay results in the immediate excitation of a collection of energetic charge carriers on the time scale of ~1 fs forming an athermal distribution of energetic charge carriers. These initially-excited charge carriers cool via electron-electron collisions on the ~100 fs time scale forming a hot Fermi-Dirac distribution. The charge carriers further relax on the time scale of ~1 ps through electron-phonon collisions.

In the case of hot d-holes, it has been suggested that hot d holes relax via an Auger process whereby an s-electron fills the d-hole creating an energetic s-hole in the process.[26] This energetic s-hole then relaxes via the electron-electron and electron-phonon interactions described above. Wolf et al. have suggested that this mechanism of energetic d-hole relaxation slightly prolongs the lifetime of energetic charge carriers in the metal nanoparticle.[26]

2.3 Activation of chemical bonds on plasmonic nanoparticles

The strong light-matter interactions displayed by plasmonic nanostructures have been leveraged for applications in spectroscopy, chemical sensing, cancer therapy, among others.[27–34] In recent years, there have also been several reports of plasmon-driven reactions on Ag and Au nanoparticles. For instance, photoexcitation of Ag and Au nanoparticles has been shown to activate CO oxidation, partial oxidation of ethylene, hydrogenation of carbonyls, dissociation of H_2, and reduction of nitroaromatics among others.[35–42] In these cases, it is argued that the energy required to activate chemical bonds is provided by plasmon-mediated excitation of energetic charge carriers at or near the adsorbate-metal interface. The mechanism of charge carrier-mediated bond activation on metal surfaces was originally uncovered through studies using high-powered lasers to excite energetic charge carriers in bulk metal surfaces.[43,44] We discussed this mechanism earlier

in Chapter 1. In brief, the photoexcitation of charge carriers at the adsorbate-metal interface results in the excitation of the adsorbate to a charged or excited state. This transfer of energy to the molecule forces the molecule to evolve along an excited potential energy surface. The excited state then decays and the molecule returns to the ground state potential energy surface but with additional vibrational energy.

A classic signature of charge carrier-mediated reactions from these experiments on extended metal surfaces was the observation of an elevated kinetic isotope effect (KIE).[45] The traditional thermal kinetic isotope effect emerges as a consequence of the lower zero point energy (vibrational ground state energy) of the heavy isotope.[46] This means that the heavy isotope will always face a slightly larger activation barrier for reaction compared to the light isotope, as depicted in Figure 2.4a. This effect is exaggerated for charge carrier-mediated reactions due to the excitation of the molecule to a charged/excited state. For the heavy isotope of the molecule, the evolution of the molecule on the charged/excited potential energy surface will be less pronounced as the heavy molecule will require larger forces (i.e. more energy) to undergo the same reconfiguration. Hence, the heavy isotope will obtain less vibrational energy from this process resulting in an elevated kinetic isotope effect for charge carrier-mediated reactions on metal surfaces (Figure 2.4b).

To build evidence of charge carrier-mediated reactions on photoexcited plasmonic nanoparticles, our group examined the effect of plasmon excitation on the KIE for ethylene partial oxidation on plasmonic Ag nanoparticle catalysts.[35,37] For this reaction, the dissociation of O_2 was determined to be rate-limiting and the KIE experiments were performed by substituting O^{16} with O^{18}. Under purely thermal conditions, a measured KIE of 1.09 was found, consistent with the theoretically-calculated value of 1.07. On the other hand, photoexcitation of the plasmonic catalyst

resulted in an elevated KIE of up to 1.48. This stark contrast in the observed KIE supports the conclusion that O_2 dissociation under photoexcitation was aided by plasmon-induced excitation of energetic charge carriers.

These findings of charge carrier-mediated reactions on photoexcited plasmonic catalysts were corroborated by several other groups for a number of different chemical transformations on Ag and Au nanoparticles. For example, Halas et al. demonstrated that photoexcited Au nanoparticles could result in the catalytic dissociation of H_2 at room temperature whereas little-to-no dissociation took place under purely thermal conditions even at temperatures as high at 100°C.[36,38] Furthermore, it was shown that the photocatalytic rate of H_2 dissociation was proportional to the plasmon intensity of the Au nanoparticles. These data demonstrate that plasmon-mediated excitation of energetic charge carriers was involved in the activation of H_2 on the Au nanoparticles. In a separate case, Moores et al. showed that plasmonic Ag nanoparticles could drive photocatalytic hydrogenation of carbonyls under plasmon excitation.[39] Here again, no chemical conversion was observed under purely thermal conditions suggesting that the reaction was driven by plasmon-derived energetic charge carriers.
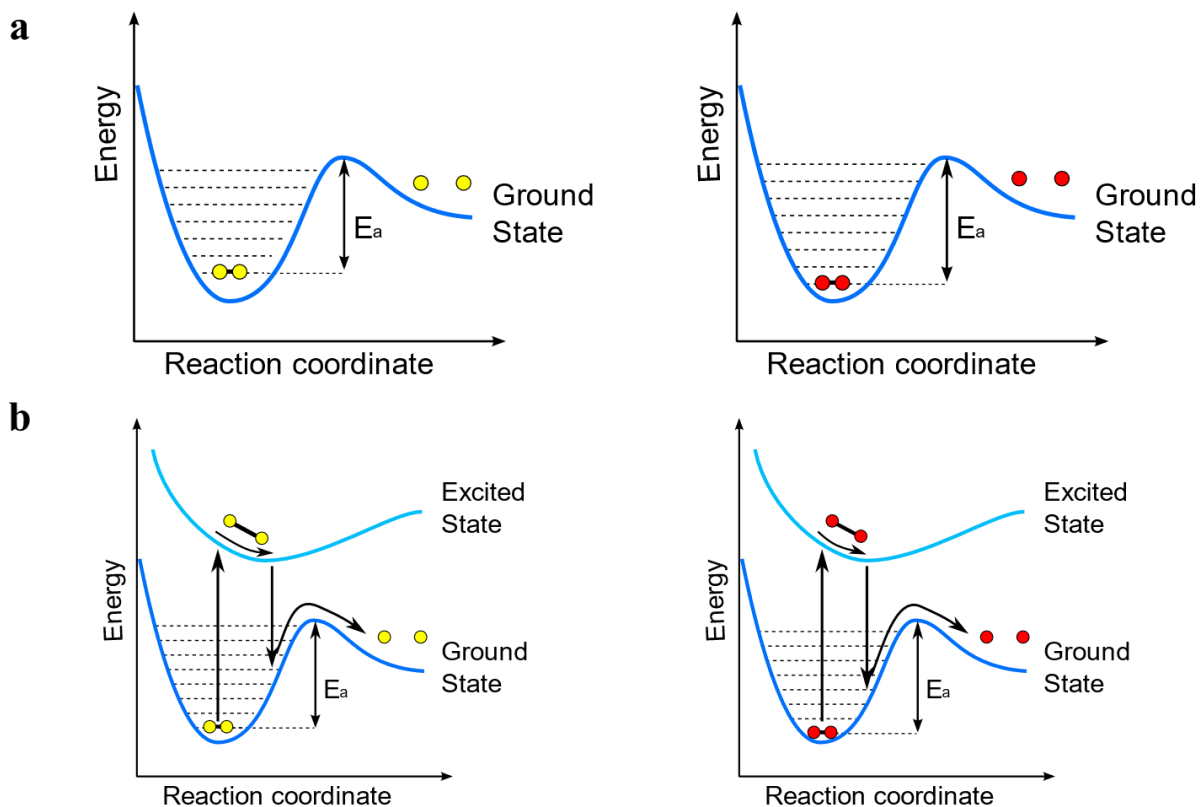
Figure 2.4 Kinetic isotope effect. (a) Thermal kinetic isotope effect (KIE). The thermal kinetic isotope effect is a result of the lower zero-point energy of the heavy isotope (depicted in red). This cause the heavy isotope to lie deeper in the potential well which results in a larger activation barrier for the dissociation of the heavy isotope. **(b)** The KIE is exaggerated for charge carrier-mediated reactions. The excitation of the molecule to an excited potential energy state forces the molecule to rearrange to accommodate the additional energy. Because more energy is required to move atoms in the heavy isotope, the evolution of the heavy isotope on the excited potential energy surface will be less pronounced. Upon relaxation, the heavy isotope may relax to a lower vibrational state compared to the light isotope thereby widening the difference in the apparent activation barrier for dissociation between the light and heavy isotopes.

The interest in plasmonic catalysis stems from this ability to perform charge carrier-mediated reactions under low intensity visible light illumination on nanostructured catalysts. In temperature-driven reactions, energy is provided to all adsorbates and molecular vibrations indiscriminately resulting in the simultaneous activation of many reaction pathways. Alternatively, charge carrier-mediated reactions potentially offer the opportunity to selectively transfer energy to specific adsorbates or molecular vibrations thereby pushing the evolution of reactants to a desired product state. There are two mechanisms by which plasmon energy can be transferred to adsorbates: 1) the indirect mechanism in which plasmon decay results in the generation of energetic charge carriers in the metal followed by charge injection into accessible adsorbate orbitals, and 2) the direct mechanism in which plasmon decay results in direct excitation of charge carriers into accessible adsorbate states. We will discuss both mechanisms in more detail in the following sections.

2.3.1 Indirect Transfer of Energy

The most commonly accepted mechanism for energy transfer to adsorbates on photoexcited metals is the indirect transfer mechanism. In this mechanism, photoexcitation of the plasmonic metal results in the excitation of energetic charge carriers in the metal. Charge carriers with sufficient energy at the adsorbate-metal interface can then transfer from the metal to empty states of the adsorbate-metal complex (Figure 2.5a). This transfer of charge provides additional energy to the molecule through the DIET mechanism discussed earlier.
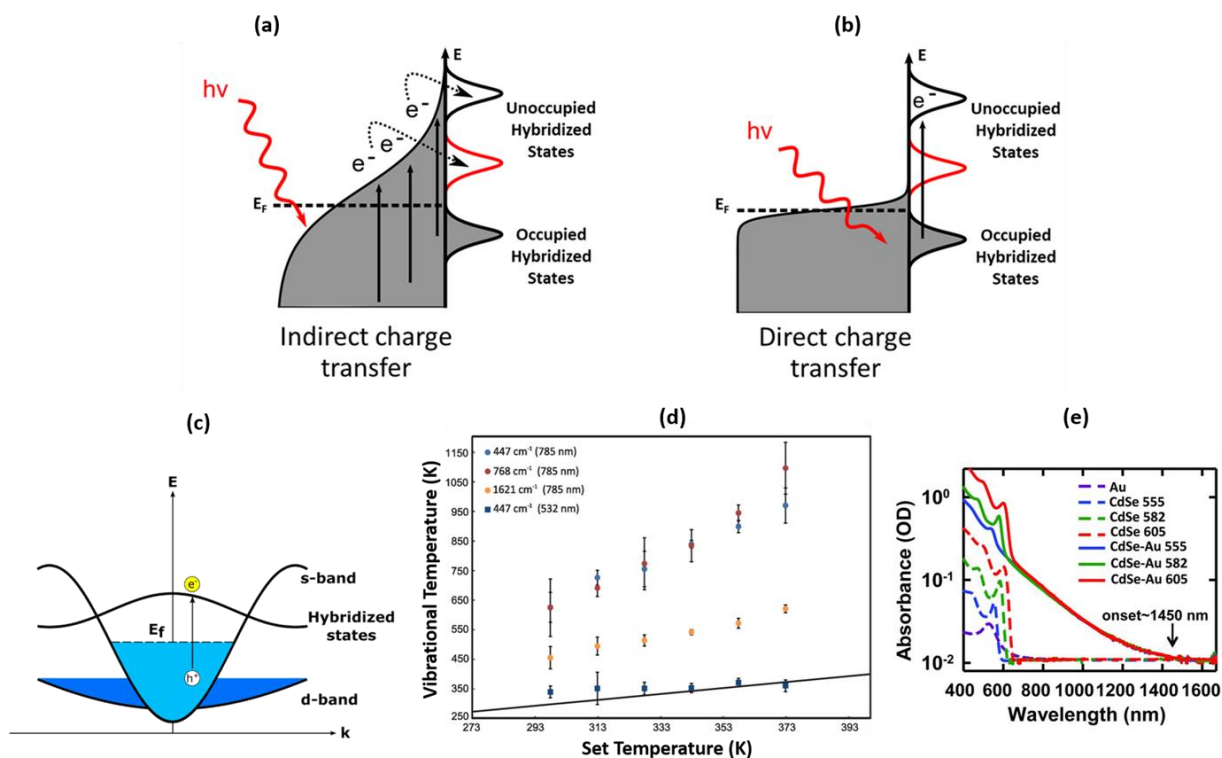
Figure 2.5 Mechanism of energy transfer in plasmonic metal-molecules systems. (a) Indirect energy transfer mechanism. Plasmon relaxation results in an electron distribution that is characterized by a high concentration of low-energy charge carriers. Those at or above the energy level of the lowest unoccupied adsorbate orbitals can transfer into those orbitals. **(b)** Direct energy transfer mechanism. Decay of a resonant plasmon causes direct excitation of charge carriers within the adsorbate-metal complex. **(c)** The adsorption of molecules onto the metal surface essentially creates a band of hybridized metal-adsorbate states which allows for direct excitations form the metal to these states. **(d)** Temperatures of different vibrational modes of MB chemisorbed on Ag. Under 532 nm illumination, the vibrational temperature is nearly equal to the set temperature (represented by the black line). Under 785 nm illumination, the vibrational temperatures for all modes are significantly increased above the metal nanoparticle temperature, indicating a resonant, selective energy transfer into the MB adsorbate. **(e)** Excitation of Au nanoparticles strongly coupled with CdSe nanorods results in energy transfer between Au and CdSe which results in a continuous absorption feature extending to the near-infrared (IR) spectrum. Figure 2.5c adapted from ref 20. Figure 2.5d was taken from ref 50. Figure 2.5e was taken from ref 51.

31

In this mechanism, the transfer of energy to adsorbates will depend on the positioning of the adsorbate states relative to the Fermi level of the metal. Adsorbate states closer to the Fermi level will always experience higher rates of energy transfer due to the high density of energetic charge carriers closer to the Fermi level. Consequently, activation of chemical bonds associated with high energy adsorbate states will result in the simultaneous activation of chemical bonds associated with low energy adsorbate states. Although this energy transfer mechanism can produce reaction outcomes unique from thermal reactions, it does not allow for significant control of the energy transfer and chemical bond activation processes which ultimately limits the ability to control product selectivity.

2.3.2 Direct Transfer of Energy

An alternative mechanism for the transfer of energy from photoexcited metals to adsorbates involves the direct excitation of charge carriers from the metal to hybridized states at the adsorbate-metal interface, as depicted in Figure 2.5b.[47] In this mechanism, chemical bonding of the adsorbate with the metal results in the formation of hybridized electronic states at the interface.[48] These hybridized electronic states of the adsorbate-metal complex provide an additional energy dissipation pathway for the energy collected via LSPR excitation. The alignment of these states in momentum-space with filled states of the metal can allow for direct, momentum-conserved excitations of electrons from filled metal states to empty states in the adsorbate-metal complex (Figure 2.5c).[49] In bulk metals, the probability of exciting these transitions is inherently low due to the low density of these hybridized states compared to bulk metal states. For plasmonic nanostructures, the intense electric fields generated at the surface via LSPR excitation essentially reroutes charge excitation processes to the surface. This effect combined with the emergence of

the inherently fast momentum-conserved direct electronic transitions results in the preferential transfer of energy to the adsorbate.

In contrast to the indirect mechanism, the direct mechanism avoids the excitation of charge carriers in the metal suggesting that plasmon energy can be channeled to particular adsorbates by targeting specific states at the interface with resonant photons. For example, our group has shown that the direct transfer mechanism is the dominant pathway for energy transfer to adsorbates for the case of methylene blue chemisorbed on Ag nanoparticles.[47,50] In this study, we used surface-enhanced Raman spectroscopy to follow the flow of energy in our model system. It was found that photoexcitation of the system with 785 nm light resulted in significantly more energy transfer to vibrational modes of the molecule compared to photoexcitation with 532 nm light of the same photon flux. This resonant energy transfer induced by 785 nm photons resulted in the non-equilibrium heating of the molecule as shown in Figure 2.5d. These results suggest that chemical bonding of the adsorbate with the metal surface opened new channels for energy dissipation that could be targeted using 785 nm light but were inaccessible for higher energy photons (i.e. 532 nm light).

Similar findings were reported by Lian et al. for a system of Au nanoparticles coupled with CdSe nanorods.[51] Here, it was argued that the chemical-attachment of the Au nanoparticles to the CdSe nanorods resulted in strong mixing of the electronic states of the two materials. This interaction opened a new pathway for the dissipation of plasmon energy via interfacial charge carrier excitations. Optical measurements combined with transient absorption spectroscopy (Figure 2.5e) demonstrated that plasmon excitation of the Au nanoparticles resulted in energy transfer to the CdSe nanorods via direct electronic transitions from filled metal states to the conduction band of the semiconductor at the interface between the two materials.

2.4 Limitations of Plasmonic Catalysis

Although plasmon-driven reactions present exciting possibilities for controlling product selectivity in chemical transformations on metal surfaces, there are several complexities associated with plasmonic catalysis that must be emphasized. Firstly, the selective transfer of energy to targeted adsorbates depends largely on the chemical interaction of the adsorbate with the metal surface. For instance, it is possible that only a few combinations of plasmonic metal-adsorbate systems will provide hybridized states that can be targeted by visible light photons. This limitation is exacerbated by the inherently low chemical reactivity of the noble plasmonic metals (Cu, Ag, and Au).[52,53] Secondly, the plasmon excitation frequency of the nanoparticles must also be aligned to match the energy gap of the direct excitation associated with the hybridized states of the adsorbate-metal complex. This alignment is critical as excitation of LSPR is required to produce the elevated electric field intensities at the surface of the plasmonic nanoparticles which compensates for the relatively low density of the hybridized states. Lastly and perhaps most saliently, the limited catalytic activity of plasmonic metals (Cu, Ag, and Au) significantly restricts the phase space of chemical transformations that can benefit from plasmonic catalysis.

This last point has been the central obstacle to expanding the use of plasmonic catalysis. The main objective of this dissertation is to develop a fundamental understanding of the physical mechanisms of energy flow in plasmonic nanoparticles and leverage this understanding to design functioning nanostructures where a plasmonic material concentrates light energy and channels this energy efficiently towards a more active catalytic material. The catalytic materials we have focused on are non-noble transition metals such Pt, Pd, Ni, etc. We hypothesized that it could be possible to combine the optical properties of plasmonic metals with the catalytic properties of other transition metals through the synthesis of bimetallic nanoparticles. We chose Ag as the plasmonic

metal because it has the lowest losses of any of the plasmonic metals. For our catalytic metal, we focused mainly on Pt given its ubiquity in heterogeneous catalysis.

These two metals can be combined in many different ways at the nanoscale. We considered two extremes: Ag-Pt alloys in which the two metals are completely mixed in a single nanostructure and Ag-Pt core-shell nanoparticles where both metals are completely separated from one another. In the case of the alloy nanoparticles, we hypothesized that by using a small amount of Pt, we could create nanostructures that still interacted with visible light through LSPR excitation and the energy collected by LSPR could help drive reactions on Pt atoms at the surface of the alloy nanoparticles.

However, we also anticipated that the heterogeneity of the alloy surface may present a challenge in rigorously interpreting data from spectroscopic and reactor studies. This motivated us to simultaneously pursue the more difficult goal of developing a synthesis for Ag-Pt core-shell nanoparticles with ultra-thin shells of Pt (~1 nm). We hypothesized that the plasmonic core of these structures would enable the collection and concentration of light energy at the Pt surface via LSPR excitation thereby allowing for plasmon-enhanced surface chemistry on a pure Pt surface.

2.5 References

1. Maier, S. A. *Plasmonics: Fundamentals and Applications*. (Springer Science & Business Media, 2007).

2. Kelly, K. L., Coronado, E., Zhao, L. L. & Schatz, G. C. The Optical Properties of Metal Nanoparticles: The Influence of Size, Shape, and Dielectric Environment. *J. Phys. Chem. B* **107,** 668–677 (2002).

3. Link, S. & El-Sayed, M. A. Spectral Properties and Relaxation Dynamics of Surface Plasmon Electronic Oscillations in Gold and Silver Nanodots and Nanorods. *J. Phys. Chem. B* **103,** 8410–8426 (1999).

4. El-Sayed, M. A. Some Interesting Properties of Metals Confined in Time and Nanometer Space of Different Shapes. *Acc. Chem. Res.* **34,** 257–264 (2001).

5. Langhammer, C., Kasemo, B. & Zorić, I. Absorption and scattering of light by Pt, Pd, Ag, and Au nanodisks: Absolute cross sections and branching ratios. *The Journal of Chemical Physics* **126,** 194702 (2007).

6. Kreibig, U. & Vollmer, M. *Optical Properties of Metal Clusters*. (Springer Science & Business Media, 2013).

7. Halas, N. J., Lal, S., Chang, W.-S., Link, S. & Nordlander, P. Plasmons in Strongly Coupled Metallic Nanostructures. *Chem. Rev.* **111,** 3913–3961 (2011).

8. Hao, E. & Schatz, G. C. Electromagnetic fields around silver nanoparticles and dimers. *The Journal of Chemical Physics* **120,** 357–366 (2004).

9. Linic, S., Christopher, P. & Ingram, D. B. Plasmonic-metal nanostructures for efficient conversion of solar to chemical energy. *Nat Mater* **10,** 911–921 (2011).

10. Brus, L. Noble Metal Nanocrystals: Plasmon Electron Transfer Photochemistry and Single-Molecule Raman Spectroscopy. *Acc. Chem. Res.* **41,** 1742–1749 (2008).

11. Moskovits, M. Surface-enhanced spectroscopy. *Rev. Mod. Phys.* **57,** 783–826 (1985).

12. Moskovits, M. Surface-enhanced Raman spectroscopy: a brief retrospective. *J. Raman Spectrosc.* **36,** 485–496 (2005).

13. Kneipp, K. *et al.* Near-infrared surface-enhanced Raman scattering can detect single molecules and observe 'hot' vibrational transitions. *J. Raman Spectrosc.* **29,** 743–747 (1998).

14. Jiang, Bosnick, K., Maillard, M. & Brus, L. Single Molecule Raman Spectroscopy at the Junctions of Large Ag Nanocrystals. *J. Phys. Chem. B* **107,** 9964–9972 (2003).

15. Kneipp, K. *et al.* Single Molecule Detection Using Surface-Enhanced Raman Scattering (SERS). *Phys. Rev. Lett.* **78,** 1667–1670 (1997).

16. Evanoff, D. D. & Chumanov, G. Size-Controlled Synthesis of Nanoparticles. 2. Measurement of Extinction, Scattering, and Absorption Cross Sections. *J. Phys. Chem. B* **108,** 13957–13962 (2004).

17. Jain, P. K., Lee, K. S., El-Sayed, I. H. & El-Sayed, M. A. Calculated Absorption and Scattering Properties of Gold Nanoparticles of Different Size, Shape, and Composition: Applications in Biological Imaging and Biomedicine. *J. Phys. Chem. B* **110,** 7238–7248 (2006).

18. Manjavacas, A., Liu, J. G., Kulkarni, V. & Nordlander, P. Plasmon-Induced Hot Carriers in Metallic Nanoparticles. *ACS Nano* **8,** 7630–7638 (2014).

19. Atwater, H. A. & Polman, A. Plasmonics for improved photovoltaic devices. *Nat Mater* **9,** 205–213 (2010).

20. Khurgin, J. B. How to deal with the loss in plasmonics and metamaterials. *Nature Nanotechnology* **10,** 2–6 (2015).

21. Brown, A. M., Sundararaman, R., Narang, P., Goddard, W. A. & Atwater, H. A. Nonradiative Plasmon Decay and Hot Carrier Dynamics: Effects of Phonons, Surfaces, and Geometry. *ACS Nano* **10,** 957–966 (2016).

22. Bernardi, M., Mustafa, J., Neaton, J. B. & Louie, S. G. Theory and computation of hot carriers generated by surface plasmon polaritons in noble metals. *Nature Communications* **6,** 7044 (2015).

23. Sundararaman, R., Narang, P., Jermyn, A. S., Goddard Iii, W. A. & Atwater, H. A. Theoretical predictions for hot-carrier generation from surface plasmon decay. *Nat Commun* **5,** 5788 (2014).

24. Frischkorn, C. & Wolf, M. Femtochemistry at Metal Surfaces: Nonadiabatic Reaction Dynamics. *Chem. Rev.* **106,** 4207–4233 (2006).

25. Brongersma, M. L., Halas, N. J. & Nordlander, P. Plasmon-induced hot carrier science and technology. *Nat Nano* **10,** 25–34 (2015).

26. Knoesel, E., Hotzel, A. & Wolf, M. Ultrafast dynamics of hot electrons and holes in copper: Excitation, energy relaxation, and transport effects. *Phys. Rev. B* **57,** 12812–12824 (1998).

27. Kambhampati, P., Child, C. M., Foster, M. C. & Campion, A. On the chemical mechanism of surface enhanced Raman scattering: Experiment and theory. *The Journal of Chemical Physics* **108,** 5013–5026 (1998).

28. Jain, P. K., Huang, X., El-Sayed, I. H. & El-Sayed, M. A. Noble Metals on the Nanoscale: Optical and Photothermal Properties and Some Applications in Imaging, Sensing, Biology, and Medicine. *Acc. Chem. Res.* **41,** 1578–1586 (2008).

29. Dolinnyi, A. I. Nanometric Rulers Based on Plasmon Coupling in Pairs of Gold Nanoparticles. *J. Phys. Chem. C* (2015). doi:10.1021/jp5116614

30. Nasir, M. E., Dickson, W., Wurtz, G. A., Wardley, W. P. & Zayats, A. V. Hydrogen Detected by the Naked Eye: Optical Hydrogen Gas Sensors Based on Core/Shell Plasmonic Nanorod Metamaterials. *Adv. Mater.* **26,** 3532–3537 (2014).

31. Carpin, L. B. *et al.* Immunoconjugated gold nanoshell-mediated photothermal ablation of trastuzumab-resistant breast cancer cells. *Breast Cancer Res Treat* **125,** 27–34 (2010).

32. El-Sayed, I. H., Huang, X. & El-Sayed, M. A. Selective laser photo-thermal therapy of epithelial carcinoma using anti-EGFR antibody conjugated gold nanoparticles. *Cancer Letters* **239,** 129–135 (2006).

33. Neumann, O. *et al.* Nanoparticle-Mediated, Light-Induced Phase Separations. *Nano Lett.* **15,** 7880–7885 (2015).

34. Aslam, U. & Linic, S. Kinetic Trapping of Immiscible Metal Atoms into Bimetallic Nanoparticles through Plasmonic Visible Light-Mediated Reduction of a Bimetallic Oxide Precursor: Case Study of Ag–Pt Nanoparticle Synthesis. *Chem. Mater.* **28,** 8289–8295 (2016).

35. Christopher, P., Xin, H. & Linic, S. Visible-light-enhanced catalytic oxidation reactions on plasmonic silver nanostructures. *Nat Chem* **3,** 467–472 (2011).

36. Mukherjee, S. *et al.* Hot Electrons Do the Impossible: Plasmon-Induced Dissociation of H2 on Au. *Nano Lett.* **13,** 240–247 (2013).

37. Christopher, P., Xin, H., Marimuthu, A. & Linic, S. Singular characteristics and unique chemical bond activation mechanisms of photocatalytic reactions on plasmonic nanostructures. *Nat Mater* **11,** 1044–1050 (2012).

38. Mukherjee, S. *et al.* Hot-Electron-Induced Dissociation of H2 on Gold Nanoparticles Supported on SiO2. *J. Am. Chem. Soc.* **136,** 64–67 (2014).

39. Landry, M. J., Gellé, A., Meng, B. Y., Barrett, C. J. & Moores, A. Surface-Plasmon-Mediated Hydrogenation of Carbonyls Catalyzed by Silver Nanocubes under Visible Light. *ACS Catal.* **7,** 6128–6133 (2017).

40. Zhu, H., Ke, X., Yang, X., Sarina, S. & Liu, H. Reduction of Nitroaromatic Compounds on Supported Gold Nanoparticles by Visible and Ultraviolet Light. *Angewandte Chemie* **122,** 9851–9855 (2010).

41. Kim, Y., Wilson, A. J. & Jain, P. K. The Nature of Plasmonically Assisted Hot-Electron Transfer in a Donor–Bridge–Acceptor Complex. *ACS Catal.* 4360–4365 (2017). doi:10.1021/acscatal.7b01318

42. Huang, Y.-F. *et al.* Activation of Oxygen on Gold and Silver Nanoparticles Assisted by Surface Plasmon Resonances. *Angewandte Chemie* **53,** 2353–2357 (2014).

43. Ageev, V. N. Desorption induced by electronic transitions. *Progress in Surface Science* **47,** 55–203 (1994).

44. Misewich, J. A., Heinz, T. F. & Newns, D. M. Desorption induced by multiple electronic transitions. *Phys. Rev. Lett.* **68,** 3737–3740 (1992).

45. Bonn, M. *et al.* Phonon- Versus Electron-Mediated Desorption and Oxidation of CO on Ru(0001). *Science* **285,** 1042–1045 (1999).

46. Bigeleisen Jacob & Wolfsberg Max. Theoretical and Experimental Aspects of Isotope Effects in Chemical Kinetics. *Advances in Chemical Physics* (2007). doi:10.1002/9780470143476.ch2

47. Boerigter, C., Campana, R., Morabito, M. & Linic, S. Evidence and implications of direct charge excitation as the dominant mechanism in plasmon-mediated photocatalysis. *Nat Commun* **7,** 10545 (2016).

48. Palmer, R. E. & Rous, P. J. Resonances in electron scattering by molecules on surfaces. *Rev. Mod. Phys.* **64,** 383–440 (1992).

49. Yan, J., Jacobsen, K. W. & Thygesen, K. S. First-principles study of surface plasmons on Ag(111) and H/Ag(111). *Phys. Rev. B* **84,** 235430 (2011).

50. Boerigter, C., Aslam, U. & Linic, S. Mechanism of Charge Transfer from Plasmonic Nanostructures to Chemically Attached Materials. *ACS Nano* **10,** 6108–6115 (2016).

51. Wu, K., Chen, J., McBride, J. R. & Lian, T. Efficient hot-electron transfer by a plasmon-induced interfacial charge-transfer transition. *Science* **349,** 632–635 (2015).

52. Hammer, B. & Nørskov, J. K. Theoretical surface science and catalysis—calculations and concepts. in *Advances in Catalysis* (ed. Bruce C. Gates, H. K.) **Volume 45,** 71–129 (Academic Press, 2000).

53. Hammer, B. & Norskov, J. K. Why gold is the noblest of all the metals. *Nature* **376,** 238–240 (1995).

Chapter 3 Experimental and Theoretical Techniques

3.1 Summary

This chapter presents experimental and theoretical techniques used throughout the dissertation. Particular emphasis is placed on methods used to synthesize metal nanoparticles and bimetallic metal nanoparticles as these materials lay the foundation for generating meaningful conclusions from experimental studies. We also discuss spectroscopic techniques used to characterize the optical properties of plasmonic metal nanoparticles and catalysts. Vibrational spectroscopy, X-ray techniques, and electron microscopy tools which are heavily employed to characterize the structure and composition of materials and catalysts at the nanoscale are also discussed. Lastly, we describe the design of reactor studies for testing the photocatalytic performance of plasmonic catalysts.

3.2 Synthesis of Metal Nanoparticles

Metal nanoparticles are typically synthesized using a colloidal, solution-phase approach with four critical ingredients: the solvent, polymeric stabilizer, reducing agent, and metal precursor.[1] A synthesis usually involves combining these ingredients in a single reaction vessel, allowing the reducing agent to reduce the metal precursor into metal nanoparticles which are

quickly capped by the polymeric stabilizing agent to prevent aggregation of individual nanoparticles in solution.

The nature of the solvent often constrains the library of polymeric stabilizers, reducing agents, and metal precursors that can implemented in a synthesis. For example, organic solvents require that all other reagents used in the synthesis are hydrophobic or otherwise can be dissolved in the organic solvent. A very commonly used organic solvent for the synthesis of metal nanoparticles is oleylamine which also solvent acts as its own reducing agent and colloidal stabilizer.[2] Organic metal precursors, such as oxidized metal centers complexed with acetylacetonate moieties, are typically employed in organic solvents. By heating oleylamine to high temperatures (160-300°C), the organic metal precursor slowly decomposes forming metal nanoparticles as a result.[3] The affinity of the amine group on oleylamine for metal surfaces facilitates the capping and stabilization of individual metal nanoparticles in the solution as they form.

Other common solvents for the synthesis of metal nanoparticles include water and ethylene glycol. These are both polar solvents and are commonly paired with hydrophilic/polar stabilizing agents, reducing agents, and metal precursors. This allows for significantly more flexibility in the synthesis of metal nanoparticles with many potential choices of reducing agents (ascorbic acid, ethylene glycol, sodium citrate, sodium borohydride), polymeric stabilizing agents (polyvinyl pyrrolidone (PVP), citrate, polyvinyl alcohol, cetrimonium bromide), and metal precursors (metal nitrates, metal chlorides, transition metal complexes).[4–7] In addition to the variety of possible reagents, other ionic species have also been used to direct the growth of targeted shapes of metal nanoparticles.[8–10] This ability to control the shape of metal nanoparticles has been extensively developed for metal nanoparticles of Ag and Au and has a profound impact on the optical

properties of these materials. For example, the peak plasmon intensity for spherical Ag nanoparticles is roughly centered at 430 nm but shifts to ~530 nm for cubic Ag nanoparticles and can shift as far as ~700 nm for Ag nanoprisms.[7,11,12] In the following section, we discuss specific synthesis recipes used in this dissertation for the synthesis of Ag nanoparticles of controlled shapes.

3.3 Synthesis of Ag Nanoparticles

Throughout this dissertation, we employ Ag nanoparticles of various shapes. The recipe used to make these nanoparticles utilizes ethylene glycol as both the solvent and reducing agent.[13] PVP is used as the polymeric stabilizing agent and silver nitrate ($AgNO_3$) as the metal precursor. We first describe the synthesis of cubic Ag nanoparticles.

3.3.1 Synthesis of Ag Nanocubes

The synthesis of Ag nanocubes starts by first heating 10 mL of ethylene glycol in an uncapped 20 mL glass vial to 140°C for 1 hour. This initial heating of ethylene glycol causes a fraction of the solvent to oxidize into glycol aldehyde.[14] Glycol aldehyde then acts as a reducing agent for the reduction of Ag^+ cations later in the synthesis. Once the solvent is heated for 1 hour, 80 µL of a 36 mM aqueous HCl solution is added to the reaction mixture followed by the addition of 5 mL of a 10 mg/mL solution of PVP in ethylene glycol. Then 2 mL of a 25 mg/mL solution of $AgNO_3$ is added to the reaction mixture and a ventilated cap is placed on the reaction vessel to allow air to enter the system while also refluxing ethylene glycol.

The addition of $AgNO_3$ results in the homogeneous nucleation of small single crystal or twinned Ag nanoparticle seeds.[15] The final shape of the nanoparticles depends heavily on this initial formation of small Ag nanoparticle seeds. For example, the growth of the twinned Ag seeds produces spherically-shaped nanoparticles whereas growth of the single crystal seeds forms cubic

Ag nanoparticles.[16] In order to generate a high quality sample of Ag nanocubes, it is critical to produce a large fraction of single crystal Ag seeds and minimize or otherwise eliminate twinned Ag seeds. This is accomplished by both stabilizing single crystal Ag seeds and continuously dissolving twinned seeds. The polymeric stabilizer, PVP, has a stronger affinity for Ag(100) surfaces and preferentially binds to the single crystal seeds thereby stabilizing those particles in the reaction mixture.[17] In addition, the combination of air exposure, which provides a steady concentration of dissolved oxygen, and chlorine anions in solution act in concert to selectively etch twinned Ag seeds.[18] In order to produce a very high fraction of single crystal seeds, this etching process is allowed to take place for 16-24 hours. The etching of the twinned Ag nanoparticle seeds produces Ag^+ which will again reduce into either twinned or single crystal Ag nanoparticle seeds. The iteration of this process over the course of 16-24 hours guarantees a high purity of single crystal seeds. The reaction vessel is then capped to cut off exposure to oxygen which allows the Ag seeds (which are now exclusively single crystal seeds) to grow into Ag nanocubes. The size of the resulting Ag nanocubes can be tuned from approximately 40 nm to 110 nm in edge length by simply controlling the growth time of the nanocubes. The highest quality nanocubes are formed by allowing the nanoparticles to grow for ~ 8 hours. This solution of nanoparticles transmits a vibrant purple color which is characteristic of Ag nanocubes ~ 75 nm in edge length.

This particular synthesis is highly sensitive to the concentration of iron impurities in the ethylene glycol solvent. The concentration of iron impurities in the solvent should be lower than 0.01 ppm. It is often difficult to meet this specification for stock solutions of ethylene glycol as the solvent is commonly stored or processed in steel containers which inevitably leads to leeching of iron species into the solvent. Fe^{3+} impurities in the solvent will be reduced to Fe^{2+} under reaction

conditions by the reducing agent. Fe^{2+} impurities interfere with the synthesis of Ag nanocubes by scavenging oxygen adsorbed on the surfaces of the Ag nanoparticle seeds.[19] This prevents the selective etching of the twinned Ag nanoparticle seeds by the combined action of oxygen and chlorine which results in significant amounts of spherical Ag nanoparticles being formed. When it was not possible to purchase ethylene glycol which met this stringent iron concentration specification, we employed a method designed to chemically sequester the iron impurities. We added a small amount of ethylene diamine tetra acetic acid (EDTA) to the reaction mixture prior to adding the Ag precursor. EDTA is a hexadentate chelating agent capable of completely engulfing Fe^{3+} moieties through chemical bonds with the two amine groups and four carboxylate groups effectively neutralizing its ability to scavenge oxygen from the surface of the Ag nanoparticle seeds.

Once synthesized, the nanoparticles are washed to remove ethylene glycol and excess reaction reagents. For washing and purification, the Ag nanocubes in ethylene glycol are diluted with acetone to 45 mL and centrifugated for 20 minutes at 8,000 rpm to separate the nanoparticles from excess chemical reagents. The supernatant is discarded and the nanocubes are re-dispersed in 5 mL of deionized (DI) water. The nanoparticles are washed twice more by diluting the re-dispersed nanoparticles to 45 mL with acetone, separating the nanocubes via centrifugation for 20 minutes at 8,000 rpm, and re-dispersing in 10 mL of DI water. The concentration of the nanoparticles can be estimated by measuring the mass of 1 mL of dried Ag nanocubes.

3.3.2 Synthesis of Ag Nanospheres

The synthesis of Ag nanospheres utilizes the same basic ingredients as the Ag nanocube synthesis namely ethylene glycol, PVP, and $AgNO_3$. The primary difference between the two syntheses is that, in the Ag nanosphere synthesis, we are not concerned with the shape of Ag

nanoparticle seeds formed and hence do not need to add hydrochloric acid to the reaction mixture to control the structure of Ag nanoparticle seeds. Instead, our basic approach is burst nucleate a collection of Ag nanoparticle seeds and crowd the surface of the nanoparticles with PVP to allow for the steady, uniform growth of the Ag nanoparticles.

This is done by first preheating a 10 mL of ethylene glycol at 160°C for 1 hour in a uncapped 20 mL glass vial. This allows some fraction of the solvent to oxidize to form glycol aldehyde which acts as the reducing agent. Then, 5 mL of a 100 mg/mL solution of PVP in ethylene glycol is added to the reaction vessel. Note that this is five times greater than the amount of PVP used in the synthesis of the Ag nanocubes. Finally, 2 mL of a 25 mg/mL solution of $AgNO_3$ in ethylene glycol is rapidly injected all at once into the reaction mixture. This leads to the homogeneous nucleation of a collection of small Ag nanoparticles. The high concentration of PVP ensures that the initially-formed small Ag nanoparticles are quickly surrounded by a dense network of polymeric stabilizer. The growth of the Ag nanoparticles is now controlled by the ability of additional Ag atoms to overcome the network of PVP and nucleate on the nanoparticles instead of being controlled by the intrinsic difference in reactivity displayed by the various surface facets expressed by the Ag nanoparticles.[10] This leads to the relatively uniform deposition of Ag atoms onto the Ag nanoparticles and eventual formation of Ag nanospheres with an average diameter of ~ 60 nm.

Once synthesized, the nanoparticles are washed to remove ethylene glycol and excess reaction reagents using a procedure similar to the Ag nanocube wash described earlier. For washing and purification, the Ag nanospheres in ethylene glycol are diluted with acetone to 45 mL and centrifugated for 20 minutes at 8,000 rpm to separate the nanoparticles from excess chemical reagents. The supernatant is discarded and the nanocubes are re-dispersed in 5 mL of ethanol. The

nanoparticles are washed twice more by diluting the re-dispersed nanoparticles to 45 mL with acetone, separating the nanocubes via centrifugation for 20 minutes at 8,000 rpm, and re-dispersing in 10 mL of ethanol. The nanoparticles can also be re-dispersed in DI water; however, the solution tends to form a metal sheen at the liquid-air interface and the nanoparticles have a tendency to aggregate in water. Solutions of Ag nanospheres synthesized using this ethylene glycol synthesis method tend to degrade within a few days and should be used immediately.

In addition to the above-described ethylene glycol synthesis for Ag nanospheres, we also used a room-temperature, water-based synthesis for Ag nanospheres for performing small experiments and tests. The synthesis uses ascorbic acid in the place of ethylene glycol-derived glycol aldehyde as the reducing agent. In brief, 50 mg of $AgNO_3$ and 500 mg of PVP are dissolved in 15 mL of DI water contained in a 50 mL polypropylene centrifuge tube (the reaction vessel). In a separate 50 mL centrifuge tube, 100 mg of ascorbic acid are dissolved in 5 mL of DI water. The pH of the ascorbic acid solution is increased to ~12 through the addition of a sodium hydroxide solution. This causes the equilibrium of the acid dissociation to favor higher concentrations of the conjugate base, ascorbate. Ascorbate anions provide substantial reducing power and can quickly reduce the Ag^+ cations even at room temperature.[20] The reducing solution is added to the reaction mixture in one swift motion while swirling the reaction mixture by hand and the formation of the Ag nanoparticles takes place nearly instantaneously. This synthesis produces Ag nanospheres ~ 30 nm in diameter. Note that glass containers are not used in this synthesis due to the incompatibility of glass containers with basic solutions.

3.4 Synthesis of Bimetallic Metal Nanoparticles

A large part of this dissertation is focused on combining the optical properties of a plasmonic metal (such as Ag) with the catalytic properties of another transition metal (such as Pt).

A promising approach for doing this is by combining the two metals in a single, bimetallic nanostructure. Bimetallic nanoparticles often exhibit hybrid or completely unique physical and chemical properties relative to their constituent metals.[21,22] These properties depend not only on the composition of the bimetallic nanoparticles but also on the level of segregation among constituent metals. The common structures of bimetallic nanoparticles include: (i) core-shell configurations, where the core is composed of one metal and the shell of the other, (ii) phase-segregated structures where the two metals are in general separated from each other with only partial mixing at the interfaces between the metals, and (iii) alloy structures where the two metals exhibit high degree of intermixing. Two general approaches are used to synthesis bimetallic nanoparticles, simultaneous reduction and sequential reduction.

The simultaneous reduction approach starts by adding metal precursors of both metals to the reaction vessel at once. Then, a strong reducing environment is established commonly through the addition of a strong chemical reducing agent and less often by using other reducing stimuli (high energy radiation or high temperatures).[23] The outcome of the synthesis will depend on the susceptibility of the metal precursors to reduce (i.e. the reduction potential of the metal precursors) and the miscibility of the two metals. In the case where the two metals are highly miscible and have similar reduction potentials, the reducing agent will reduce the precursors of both metals at equal rates (i.e. similar reduction kinetics) and the penalty for forming bonds between the two metals is relatively low (i.e. no thermodynamic hinderance to mixing). This results in the formation of well-mixed alloy nanostructures containing both metals. On the other hand, if the precursors of the two metals are significantly different, the more reactive metal precursor (i.e. the one with the higher reduction potential) will reduce first forming monometallic nanoparticles of that metal. The second metal will then slowly reduce onto the first metal resulting in the formation of core-shell

47

nanoparticles. Although the simultaneous reduction method works well for highly-miscible metals, it is often difficult to generate bimetallic nanoparticles made of two immiscible metals. The thermodynamic penalty for creating bonds between the two metals drives the outcome of the synthesis towards the homogeneous nucleation of monometallic nanoparticles of each individual metal.[24] Given that Ag and Pt are immiscible, the synthesis of Ag-Pt alloys cannot be accomplished using conventional synthesis strategies. In chapter 4, we discuss our efforts in a developing a new approach to the synthesis of well-mixed transition metal alloy nanoparticles composed of immiscible metals (in this case, Ag and Pt).

In addition to simultaneous reduction, another widely-used approach for synthesizing bimetallic nanoparticles is to first form nanoparticles of one metal and then introduce a precursor for the second metal.[25] To ensure formation of bimetallic nanoparticles, the reduction of the second metal must be carefully controlled to minimize homogeneous nucleation of the second metal. This is accomplished by using relatively mild reducing conditions and/or a fairly inert metal precursor of the second metal. The surface of the preformed metal nanoparticles act to catalyze the reduction of the second metal onto the nanoparticles thereby creating core-shell nanostructures. This method has seen rapid growth in recent years with the emergence of "seed-mediated" colloidal synthesis recipes.[25–27] Seed-mediated syntheses rely on first forming monometallic nanoparticles of a particular metal, purifying and concentrating the nanoparticles, and using the nanoparticles as seeds onto which a second metal is deposited. In this case, the nanoparticle seeds are essentially an additional synthesis reagent and can be combined with other species (such as ions or chemical capping agents) to direct the growth of the second metal in unique ways. We use this approach in chapters 4 and 5 to synthesis bimetallic nanoparticles of Ag-Pt.

3.5 Preparation of Catalysts from Colloidal Nanoparticles

Metal nanoparticle catalysts are usually prepared via wet impregnation of metal salts in metal oxide supports followed by thermal decomposition of the metal salts into nanoparticles.[28] This approach produces high purity catalysts but does not offer the degree of control over the structure and composition of metal nanoparticles that can be achieved with colloidal synthesis techniques. However, there are several challenges associated with preparing metal nanoparticle catalysts from solutions of colloidal metal nanoparticles. For instance, colloidal solutions of nanoparticles are stabilized with surface-bond surfactants or polymers which must be removed to produce completely clean surfaces. In addition, forcing the nanoparticles to move from the solution phase and attach onto the metal oxide support can be challenging.

In order to circumvent these issues, we developed a method for depositing metal nanoparticles on oxide supports which relies on destabilizing the colloidal solution of metal nanoparticles in a slurry with the metal oxide support. A typical catalysts preparation procedure begins by adding the metal oxide support powder to water under continuous stirring. The solution of metal nanoparticles is then added slowly to the mixing slurry dropwise to ensure good dispersion of the nanoparticles on the oxide support. This solution is allowed to mix for approximately 2 hours. Then 1 mL of a 1 M solution of $NaNO_3$ (or other ionic salts) is added dropwise to the mixture. This causes the ionicity of the solution to dramatically increase which destabilizes the colloidal dispersion of nanoparticles. The metal nanoparticles fall out of solution and deposit onto the metal oxide support. The solution is allowed to mix overnight following the addition of the salt solution. It is then centrifuged at 5000 rpm for 10 minutes to separate the catalyst from the liquid. The catalyst is then washed via centrifugation once more with water to remove excess salt and extract most of the polymeric stabilizing agent off the nanoparticles. The washed catalyst is then dried in a vacuum oven at 40°C. Although this washing procedure removes most of the polymeric

stabilizing agent on the nanoparticles, there may still be some leftover polymer on the catalyst surface. To remove this residual stabilizing agent, the catalyst is pretreated with air at temperatures between 200-300°C for 3-5 hours at the start of every reaction experiment.[29,30] This completes the catalyst preparation procedure.

3.6 Characterizing the Optical Properties of Metal Nanoparticles and Catalysts

A key feature of the metal nanoparticles studied in this dissertation is their ability to interact strongly with visible light. We characterized the optical properties of all metal nanoparticles and metal nanoparticle catalysts using a suite of optical characterization tools and techniques including UV-vis extinction spectroscopy, optical integrating sphere spectroscopy, finite element method electrodynamic simulations, and diffuse reflectance UV-vis spectroscopy.

3.6.1 UV-vis Extinction Spectroscopy

The optical properties of colloidally-synthesized metal nanoparticles is initially characterized using UV-vis extinction spectroscopy. All measurements are taken using a ThermoFisher Scientific Evolution 300 spectrophotometer. To prepare a sample for analysis, a dilute solution of the metal nanoparticles is prepared in a 3 mL polystyrene cuvette. A sample of just the solvent is also prepared and used to set the background. Sample analysis is performed by passing monochromatic light through the sample and collecting all transmitted photons. Photons that are extinct (absorbed or scattered) by the sample are not detected and an extinction spectrum can be generated from the difference in the sample data and the control (solvent only). When performing measurements in transmission mode, the instrument provides the fraction of photons that are transmitted through the sample and the extinction fraction can simply be calculated as

$$Extinction\ fraction = 1 - (transmission\ fraction)$$

3.6.2 Optical Integrating Sphere Spectroscopy

The extinction fraction is the sum of the absorption fraction and scattering fraction. To decouple absorption from scattering, we use an optical integrating sphere combined with a monochromatic visible light source and photodiode detector. In this technique, a dilute 3 mL solution of the colloidal nanoparticles is prepared in a cuvette and the cuvette is positioned in the center of an integrating sphere. The optical integrating sphere is coated with a highly reflective material. Monochromatic light is passed through the center of the sample and any light that transmits through or is scattered by the sample bounces around in the integrating sphere until it hits the photodiode detector. Any light that is not collected by the photodiode detector must have been absorbed by the sample. As such, this technique allows for the absorption of the sample to be measured. The data collected using this technique is the a combination of transmission and scattering from the nanoparticles. The absorption fraction can be calculated from the data as

$$Absorption\ fraction = 1 - (trasmission + scattering\ fraction)$$

Given that the extinction fraction can be measured using UV-vis extinction spectroscopy, the scattering fraction can be calculated as

$$Scattering\ fraction = extinction\ fraction - (absorption\ fraction)$$

3.6.3 Finite Element Method Electrodynamic Simulations

The optical properties of metal nanoparticles are also studied using electrodynamic simulations. The optical extinction, absorption, and scattering efficiencies as well as spatial distribution of absorption within nanoparticles are calculated using COMSOL Multiphysics finite element-based software. We utilized the 'Wave optics' module to calculate the scattered field resulting from a plane wave incident on a model 3-D nanoparticle. The plane wave was defined as: $E = E_0e^{-ikx}$ and was polarized in the z-direction. The optical data for Ag and Pt were taken from COMSOL's Optical Materials database (Rakic et. al)[31] and a region of air was defined around the

51

particle by setting the real part of the dielectric function equal to 1. The width of the region of air around the particle was equal to half the wavelength of the incident plane wave and a perfectly matched layer (PML) was constructed to act as an absorber of the scattered field.

3.6.4 Diffuse Reflectance UV-vis Spectroscopy

To characterize the optical properties of solid powder materials (such as our catalysts), we use couple a Harrick Praying Mantis diffuse reflectance cell with our spectrophotometer. The cell is able to accept powders in sample cups but can also be interfaced with a temperature-controlled Harrick microreactor to perform analysis under various atmospheric and temperature conditions. The spectrophotometer is operated in "absorption" mode and the appropriate background is taken prior to analyzing the sample. In the diffuse reflectance configuration, light from the spectrophotometer enter one side of the diffuse reflectance cell, bounces off of two mirrors used to guide the light to the powder sample. The light than interacts with the sample and diffusely scattered light is collected by two parabolic mirrors situated above the powder samples. The parabolic mirrors direct the light towards two additional mirrors which then pass the light to the detector. The thickness of the sample bed prevents any light from transmitting through the entire bed. As such, light absorbed by the sample and some fraction of light scattered by the sample is not detected. Therefore, this technique mainly measures absorption with some contribution from scattering depending on the sample.

3.7 Characterizing the Structure and Composition of Metal Nanoparticles

In order to develop synthesis methods for well-defined bimetallic nanoparticles, it is critical to perform comprehensive characterize of the structure and composition of the resulting nanoparticles to evaluate the success of the synthesis methods. A suite of characterization tools is employed in this dissertation to paint a comprehensive picture of the structure and elemental

composition of metal nanoparticles. We use vibrational spectroscopy tools to evaluate the surface composition of the nanoparticles using probe molecules which interact with the surface. X-ray techniques are used to capture the bulk structure and surface composition of the nanomaterials. Electron microscopy and the associated energy dispersive X-ray (EDS) spectroscopy techniques are used extensively to characterize the nanoscale structure and composition of nanoparticles and catalysts.

3.7.1 Diffuse Reflectance Infrared Fourier Transform Spectroscopy

Infrared spectroscopy can be used to characterize materials by allowing infrared radiation to interact with the materials through excitations of vibrational modes on. We use this technique to characterize the surface composition of bimetallic nanoparticles. This is done by using a diffuse reflectance configuration and allowing a probe molecule, carbon monoxide, to adsorb onto the surface of the nanoparticles.[32–34] Diffuse reflectance infrared Fourier transform spectroscopy (DRIFTS) is performed using a Nicolet is50 infrared spectrometer with a liquid nitrogen-cooled HgCdTe (MCT) detector coupled with a Harrick high-temperature reactor chamber with a dome cape and KBr windows placed inside a Harrick Praying Mantis diffuse reflectance cell. The spectrometer and diffuse reflectance cell are continuously purged with N_2 gas. Data are collected by averaging 128 scans at a resolution of 4 cm^{-1}.

The nanoparticles are deposited onto a Si chip using forced deposition. The Si chip is placed at the bottom of a container filled with a solution of the nanoparticles. A high concentration salt solution is then added to the solution to destabilize the colloidal dispersion of nanoparticles which forces the nanoparticles to fall out of solution overnight and coat the Si chip. The Si chip is then washed by submerging it in DI water overnight. This procedure is analogous to the catalyst preparation procedure and helps eliminate excess salt and stabilizing agents from the surface of

the nanoparticles. The sample is then positioned inside the Harrick reactor chamber, pretreated with air at 250°C for 3 hours, and pretreated with 20% H_2 in balance N_2 at 200°C for 1 hour. The sample is then brought down to room temperature under N_2 flow. A 10% mixture of carbon monoxide in balance N_2 is then flowed over the nanoparticles for 10 minutes to allow the probe molecule to adsorb onto the surface of the metallic nanoparticles. Excess carbon monoxide is then purged from the reactor with pure N_2.

Gas-phase or free carbon monoxide displays two vibrational features in an infrared spectrum centered at 2120 and 2170 cm^{-1}. When carbon monoxide forms a chemical bond with the surface atoms of a metal, the C-O bond is weakened and displays vibrational features at energies lower than 2120 cm^{-1}. The exact location of the adsorbed C-O features depends on the orientation of the molecule on the metal surface and the strength of the interaction which both depend on the composition of the metal surface.[33,34] Hence, the position of vibrational features of the adsorbed C-O can be used to characterize the surface composition of the metal.

3.7.2 Surface-enhanced Raman Spectroscopy

Raman spectroscopy is another vibrational spectroscopy technique which uses visible light lasers (high intensity light) to force the polarization of the electron cloud around molecules.[35] This is often portrayed in quantum mechanical depictions as an excitation of the molecule to a virtual state. The polarization relaxes in a very short time period and can return the molecule to its original vibrational state (Rayleigh scattering), to a higher energy vibrational state (Stokes Raman scattering), or to a lower energy vibrational state (anti-Stokes Raman scattering). The difference in the energy of the incoming laser radiation and the light scattered from the sample can then be used to determine the energy of the vibrational mode.

The excitation of the molecule to a virtual state is an inherently low probability event and depends on the polarizability of vibrational modes in the molecule. Furthermore, the likelihood of the molecule relaxing to a higher energy vibrational state (thereby having energy deposited in the molecule) is also a low probability event which makes the Raman cross-section of most materials extremely small. However, this process can be significantly amplified through the incorporation of field-confining structures or materials such as plasmonic metal nanoparticles. The ability of plasmonic nanoparticles to collect and concentrate light energy in small volumes in the form of elevated electric field intensities can amplify the strength of weak Raman signals by up to 10^{12} times.[36] When Raman spectroscopy is performed in this way, it is referred to as surface-enhanced Raman spectroscopy (SERS).

We use SERS to characterize the presence of residual stabilizing agent or other molecular impurities on the surface of our nanoparticles. Samples for Raman spectroscopy are prepared by drop casting a small amount of the nanoparticle solution on a Si chip. Raman spectra are collected using a 532 nm diode-pumped solid state laser and a confocal 50x objective lens on a Horiba LabRAM HR system equipped with a Horiba Synapse charge-coupled device (CCD).

3.7.3 X-ray Diffraction

X-ray diffraction is used to characterize the bulk structure and composition of metal nanoparticles. The technique works by shining X-rays at a sample at various angles and measuring the extent to which those X-rays are diffracted by the material. The diffraction of the X-rays by the material is a direct consequence of the crystallography of the material and can be used as a signature of crystallographic features of specific materials. Powder X-ray diffraction data is acquired using a Rigaku Miniflex X-ray Diffractometer with Cu-Kα X-ray source operated at 40 kV and 15 mA and a scan speed of 4°/min.

3.7.4 X-ray Photoelectron Spectroscopy

X-ray photoelectron spectroscopy (XPS) bombards samples with monochromatic X-rays which can penetrate a new nanometers into the material and are high enough in energy to dislodge core electrons from the materials. The electrons are then guided to a detector where the kinetic energy of the electrons can be measured. Since the energy of the incoming radiation, kinetic energy of emitted electrons, and the work function (the energy required to remove an electron from a material to vacuum) of the spectrometer are known, it is possible to calculate the binding energy of the dislodged electron.[37] This binding energy is an intrinsic property of the elements comprising the material. Additionally, the binding energy of electrons in an atom is influenced by the oxidation state of the atoms. For example, an atom in the 2+ oxidation state is missing two electrons and hence has a higher effect nuclear charge which exerts a stronger force on the remaining electrons in the atom (i.e. the electrons have a slightly higher binding energy). Therefore, this technique can be used to characterize the near surface composition and oxidation state of materials.

We used XPS to characterize the near surface composition and oxidation state of alloy nanomaterials. XPS data are acquired using a Kratos Axis Ultra XPS with a monochromatic Al source (energy resolution ~0.5 eV). Regional scans are collected with a dwell time of 60 seconds and averaging of 10 sweeps. Peak fitting and composition calculations are performed using CasaXPS software with built-in relative correction factors.

3.7.5 Scanning Transmission Electron Microscopy

The work horse for characterizing nanomaterials in this dissertation is scanning transmission electron microscopy (STEM). This technique uses a highly-focused electron beam to scan across a thin sample. Electrons transmitted through the sample loss some energy and are collected at the bottom of the instrument where they can be used to generate an image (bright-field

image). Electrons scattered at an angle by materials in the sample are collected using a high-angle annular dark-field (HAADF) detector and provide a dark-field image. The contrast in STEM images is provided by a difference in the thickness of the sample and difference in the atomic weight of atoms in the materials. The scattering of electrons is more strongly impacted by the atomic weight of atoms in the material; therefore, dark-field images provide greater elemental contrast.

The interaction of high energy electrons with the specimen can also force the ejection of core electrons in the material. An outer shell electron can then decay to fill the hole in the inner shell emitting a photon in the process. Photons (X-rays) emitted via this process are collected and analyzed in STEM using energy-dispersive X-ray spectroscopy (EDS). By combining the scanning probe in the electron microscope with EDS, it is possible to perform elemental line scans and 2D maps of features in the sample.

STEM and EDS are performed on a JEOL 3100R05 double Cs corrected TEM/STEM operated at 300 kV accelerating voltage. STEM samples of colloidal nanoparticles are prepared by drop-casting on a carbon-on-copper 200 mesh grid. STEM samples of supported nanoparticle (catalysts) are prepared by sonicating the powder samples in a small amount of ethanol and drop casting on a carbon-on-copper 200 mesh grid. EDS elemental line scans and maps of all Ag-Pt nanoparticles are taken using the Ag Lα and Pt M transition peaks.

3.8 Reactor Studies

The photocatalytic performance of metal nanoparticle catalysts is evaluated by conducting gas-phase reactor studies. For the reactor experiments, we employ a Harrick micro-reactor equipped with a 1 cm^2 SiO_2 window which sits directly above a small cup in which the catalyst rests. The cup is first partially filled with a bed of SiO_2 beads and then is filled completely with

the catalyst. The SiO$_2$ beads provide height for the catalyst so that the catalyst can experience the maximum possible light intensity (intensity decreases with distance away from the light source). The catalyst is typically pretreated with air and H$_2$ to provide a clean surface for surface chemistry. The reactant mixture is then introduced to the reactor and the system is allowed to reach steady state overnight. Data are collected at a range of temperatures under both thermal (no catalyst illumination) and photothermal (catalyst illumination, light intensity of ~400 mW/cm^2) conditions. The intensity of light from the visible light source (Dolan-Jenner Fiber-Lite 180 with a 150 W, 21 V halogen (EKE) lamp) is measured using a thermopile detector. Thermal data are collected at a specific temperature for ~30 minutes followed by the collection of photothermal data for ~30 minutes and finally again collection of thermal data. Then the temperature is increased and the process repeated for the new temperature. Reactions are operated at differential conversion ($< 10\%$ conversion) to minimize mass transport (i.e. diffusion) limitations of the reactants to the catalytic sites and minimize thermal gradients as a result of exothermic reactions. This ensures that we are operating in a kinetically-limited regime and are measuring changes only in the reaction kinetics. The product gases are analyzed using a combination of gas chromatography and mass spectrometry.

3.9 References

1. Thanh, N. T. K., Maclean, N. & Mahiddine, S. Mechanisms of Nucleation and Growth of Nanoparticles in Solution. *Chem. Rev.* **114,** 7610–7630 (2014).

2. Mazumder, V. & Sun, S. Oleylamine-Mediated Synthesis of Pd Nanoparticles for Catalytic Formic Acid Oxidation. *J. Am. Chem. Soc.* **131,** 4588–4589 (2009).

3. Cleve, T. V., Moniri, S., Belok, G., More, K. L. & Linic, S. Nanoscale Engineering of Efficient Oxygen Reduction Electrocatalysts by Tailoring the Local Chemical Environment of Pt Surface Sites. *ACS Catal.* **7,** 17–24 (2017).

4. Christopher, P. & Linic, S. Engineering Selectivity in Heterogeneous Catalysis: Ag Nanowires as Selective Ethylene Epoxidation Catalysts. *J. Am. Chem. Soc.* **130,** 11264–11265 (2008).

5. Li, J., Liu, J., Yang, Y. & Qin, D. Bifunctional Ag@Pd-Ag Nanocubes for Highly Sensitive Monitoring of Catalytic Reactions by Surface-Enhanced Raman Spectroscopy. *J. Am. Chem. Soc.* **137,** 7039–7042 (2015).

6. Wu, X. *et al.* Photovoltage Mechanism for Room Light Conversion of Citrate Stabilized Silver Nanocrystal Seeds to Large Nanoprisms. *J. Am. Chem. Soc.* **130,** 9500–9506 (2008).

7. Jin, R. *et al.* Photoinduced Conversion of Silver Nanospheres to Nanoprisms. *Science* **294,** 1901–1903 (2001).

8. Gilroy Kyle D. *et al.* Shape-Controlled Synthesis of Colloidal Metal Nanocrystals by Replicating the Surface Atomic Structure on the Seed. *Advanced Materials* **0,** 1706312 (2018).

9. Qi, X., Balankura, T., Zhou, Y. & Fichthorn, K. A. How Structure-Directing Agents Control Nanocrystal Shape: Polyvinylpyrrolidone-Mediated Growth of Ag Nanocubes. *Nano Lett.* (2015). doi:10.1021/acs.nanolett.5b04204

10. Wiley, B., Sun, Y., Mayers, B. & Xia, Y. Shape-Controlled Synthesis of Metal Nanostructures: The Case of Silver. *Chem. Eur. J.* **11,** 454–463 (2005).

11. Aslam, U. & Linic, S. Kinetic Trapping of Immiscible Metal Atoms into Bimetallic Nanoparticles through Plasmonic Visible Light-Mediated Reduction of a Bimetallic Oxide Precursor: Case Study of Ag–Pt Nanoparticle Synthesis. *Chem. Mater.* **28,** 8289–8295 (2016).

12. Hooshmand, N., Bordley, J. A. & El-Sayed, M. A. Are Hot Spots between Two Plasmonic Nanocubes of Silver or Gold Formed between Adjacent Corners or Adjacent Facets? A DDA Examination. *J. Phys. Chem. Lett.* **5,** 2229–2234 (2014).

13. Sun, Y. & Xia, Y. Shape-Controlled Synthesis of Gold and Silver Nanoparticles. *Science* **298,** 2176–2179 (2002).

14. Skrabalak, S. E., Wiley, B. J., Kim, M., Formo, E. V. & Xia, Y. On the Polyol Synthesis of Silver Nanostructures: Glycolaldehyde as a Reducing Agent. *Nano Lett.* **8,** 2077–2081 (2008).

15. Im, S. H., Lee, Y. T., Wiley, B. & Xia, Y. Large-Scale Synthesis of Silver Nanocubes: The Role of HCl in Promoting Cube Perfection and Monodispersity. *Angewandte Chemie* **117,** 2192–2195 (2005).

16. Rycenga, M. *et al.* Controlling the Synthesis and Assembly of Silver Nanostructures for Plasmonic Applications. *Chem. Rev.* **111,** 3669–3712 (2011).

17. Im, S. H., Lee, Y. T., Wiley, B. & Xia, Y. Large-Scale Synthesis of Silver Nanocubes: The Role of HCl in Promoting Cube Perfection and Monodispersity. *Angewandte Chemie* **117,** 2192–2195 (2005).

18. Wiley, B., Herricks, T., Sun, Y. & Xia, Y. Polyol Synthesis of Silver Nanoparticles: Use of Chloride and Oxygen to Promote the Formation of Single-Crystal, Truncated Cubes and Tetrahedrons. *Nano Lett.* **4,** 1733–1739 (2004).

19. Wiley, B., Sun, Y. & Xia, Y. Polyol Synthesis of Silver Nanostructures: Control of Product Morphology with Fe(II) or Fe(III) Species. *Langmuir* **21,** 8077–8080 (2005).

20. Yang, Y., Liu, J., Fu, Z.-W. & Qin, D. Galvanic Replacement-Free Deposition of Au on Ag for Core–Shell Nanocubes with Enhanced Chemical Stability and SERS Activity. *J. Am. Chem. Soc.* **136,** 8153–8156 (2014).

21. Cortie, M. B. & McDonagh, A. M. Synthesis and Optical Properties of Hybrid and Alloy Plasmonic Nanoparticles. *Chem. Rev.* **111,** 3713–3735 (2011).

22. Gilroy, K. D., Ruditskiy, A., Peng, H.-C., Qin, D. & Xia, Y. Bimetallic Nanocrystals: Syntheses, Properties, and Applications. *Chem. Rev.* **116,** 10414–10472 (2016).

23. Ferrando, R., Jellinek, J. & Johnston, R. L. Nanoalloys: From Theory to Applications of Alloy Clusters and Nanoparticles. *Chem. Rev.* **108,** 845–910 (2008).

24. Zhang, Z., Nenoff, T. M., Huang, J. Y., Berry, D. T. & Provencio, P. P. Room Temperature Synthesis of Thermally Immiscible Ag−Ni Nanoalloys. *J. Phys. Chem. C* **113,** 1155–1159 (2009).

25. Xia, Y., Gilroy, K. D., Peng, H.-C. & Xia, X. Seed-Mediated Growth of Colloidal Metal Nanocrystals. *Angewandte Chemie* **56,** 60–95 (2017).

26. Burrows, N. D., Harvey, S., Idesis, F. A. & Murphy, C. J. Understanding the Seed-Mediated Growth of Gold Nanorods through a Fractional Factorial Design of Experiments. *Langmuir* **33,** 1891–1907 (2017).

27. Aslam, U. & Linic, S. Addressing Challenges and Scalability in the Synthesis of Thin Uniform Metal Shells on Large Metal Nanoparticle Cores: Case Study of Ag–Pt Core–Shell Nanocubes. *ACS Appl. Mater. Interfaces* **9,** 43127–43132 (2017).

28. Soled, S. Silica-supported catalysts get a new breath of life. *Science* **350,** 1171–1172 (2015).

29. Cargnello, M. *et al.* Efficient Removal of Organic Ligands from Supported Nanocrystals by Fast Thermal Annealing Enables Catalytic Studies on Well-Defined Active Phases. *J. Am. Chem. Soc.* (2015). doi:10.1021/jacs.5b03333

30. Christopher, P., Xin, H. & Linic, S. Visible-light-enhanced catalytic oxidation reactions on plasmonic silver nanostructures. *Nat Chem* **3,** 467–472 (2011).

31. Rakić, A. D., Djurišić, A. B., Elazar, J. M. & Majewski, M. L. Optical properties of metallic films for vertical-cavity optoelectronic devices. *Appl. Opt., AO* **37,** 5271–5283 (1998).

32. Schwank, J., Parravano, G. & Gruber, H. L. An infrared study of CO adsorption on magnesia-supported ruthenium, gold, and bimetallic ruthenium-gold clusters. *Journal of Catalysis* **61,** 19–28 (1980).

33. Kale, M. J. & Christopher, P. Utilizing Quantitative in Situ FTIR Spectroscopy To Identify Well-Coordinated Pt Atoms as the Active Site for CO Oxidation on Al2O3-Supported Pt Catalysts. *ACS Catal.* **6,** 5599–5609 (2016).

34. Alayoglu, S., Nilekar, A. U., Mavrikakis, M. & Eichhorn, B. Ru–Pt core–shell nanoparticles for preferential oxidation of carbon monoxide in hydrogen. *Nat Mater* **7,** 333–338 (2008).

35. Stiles, P. L., Dieringer, J. A., Shah, N. C. & Duyne, R. P. V. Surface-Enhanced Raman Spectroscopy. *Annual Review of Analytical Chemistry* **1,** 601–626 (2008).

36. Moskovits, M. Surface-enhanced Raman spectroscopy: a brief retrospective. *J. Raman Spectrosc.* **36,** 485–496 (2005).

37. Niemantsverdriet, J. W. Photoemission and Auger Spectroscopy. in *Spectroscopy in Catalysis* 39–83 (Wiley-VCH Verlag GmbH & Co. KGaA, 2007).

Chapter 4 Synthesis of Bimetallic Ag-Pt Alloy Nanoparticles

4.1 Summary

In our effort to design bimetallic nanoparticles that exhibit both the optical properties of plasmonic metals and the catalytic properties of other transition metals, we set out to develop a synthesis for bimetallic Ag-Pt alloy nanoparticles. Alloying of two metals is commonly used to create nanomaterials with a mix of chemical properties from each of the constituent metals. The ability to synthesize well-mixed bimetallic alloy nanoparticles, however, can be limited by the intrinsic immiscibility of two metals. To overcome this issue, extreme synthesis conditions, using high energy gamma radiation or very high temperatures, have been employed to trap metal atoms of immiscible metals in well-mixed alloy nanostructures. Herein, we demonstrate a more benign synthesis strategy for creating well-mixed bimetallic nanoparticles of immiscible metals. We demonstrate the formation of Ag-Pt bimetallic alloy nanoparticles through the visible light-mediated reduction of a hollow bimetallic oxide precursor containing Ag and Pt oxide. We exploit the optical properties of Ag by using visible light to excite surface plasmon resonance to drive the reduction of the Pt oxide thereby destabilizing the bimetallic precursor. Under the influence of resonant light the hollow bimetallic precursor restructures forming well-mixed Ag-Pt alloy nanoparticles.

4.2 Introduction

Bimetallic nanoparticles often exhibit a mixture of physical and chemical properties relative to their constituent metals. These properties depend not only on the composition of the bimetallic nanoparticles but also on the level of segregation among constituent metals.[1] The common structures of bimetallic nanoparticles include: (i) core-shell configurations, where the core is composed of one metal and the shell of the other, (ii) phase-segregated structures where the two metals are in general separated from each other with only partial mixing at the interfaces between the metals, and (iii) alloy structures where the two metals exhibit high degree of intermixing.[2] The alloy structures maximize the interaction between the two metals and often display the most unique physical and chemical properties compared to the constituent metals.

The synthesis of bimetallic alloy nanoparticles can be relatively simple if there is a strong thermodynamic driving force for the mixing of constitutive metals, i.e., if metals are inherently miscible. In these cases, bimetallic alloy nanoparticles can be synthesized either through simultaneous or sequential reduction of metal salts.[3] The simultaneous reduction method is possible for metal salts that have similar reduction potentials or when the reducing environment is strong enough to reduce both metals with similar reduction rates. On the other hand, sequential reduction can be used when one metal is more easily reduced than the other thereby forming "seed" particles on which the other metal can deposit. This process of sequential reduction initially forms a phase-segregated structure with interfacial contact between the two metals. By further heating of this structure, mixing of the metals, driven by thermodynamic forces, takes place resulting in an alloy structure.[4]

These methods, however, are only effective in forming alloys of highly miscible metals. Unfortunately, many metals are miscible with very limited numbers of other metals. For example,

silver (Ag) is highly miscible with only two other transition or noble metals (gold and palladium).[5,6] This synthetic constraint limits the utilization of silver-based alloy nanostructures. Forming alloys of immiscible metals generally involves more complex synthesis strategies designed to kinetically trap the two metals in a single nanostructure. These strategies often require extreme conditions (very high temperature or even high fluxes of high energy particles such as gamma rays) to induce rapid reduction of metal salts followed by rapid quenching of the nanoparticles.[7] These strategies can be augmented by a preceding formation of bimetallic precursors, which ensure that the mixing of the metals is achieved before reduction and quenching.[8] In a recent example, Ag-Co nanoparticles, combining immiscible Ag and Co atoms, were synthesized using a water-insoluble bimetallic salt precursor, $Ag_3[Co(CN)_6]$, formed by mixing $AgNO_3$ and $K_3[Co(CN)_6]$.[9] The formation of this bimetallic salt induced atomic scale mixing of Ag and Co atoms. The bimetallic salt precursor was reduced rapidly at 500°C under hydrogen flow and then rapidly cooled, to minimize phase separation of Ag and Co, forming Ag-Co bimetallic nanoparticles. However, even in this case, due to the relatively slow and non-homogeneous temperature-driven reduction process, a significant phase separation between Co and Ag took place allowing for limited Ag-Co mixing. Another issue with these approaches is that the increase in the reduction temperature, required to increase the reduction rates, results in sintering and agglomeration of metal nanoparticles which is highly undesirable for applications that require materials with high metal surface-to-volume ratios, such as heterogeneous catalysis and electrocatalysis.[10]

Herein, we demonstrate an approach to synthesize bimetallic alloys of immiscible metals utilizing a similar strategy of forming a bimetallic precursor state. The novelty of our approach is that this state is reduced using a flux of resonant light rather than temperature. This process leads

to a reduction of the precursor state without significant phase segregation and sintering. We illustrate the approach by synthesizing alloy nanoparticles of immiscible Ag and Pt atoms.[11] We first synthesized a bimetallic Ag/Pt-oxide hollow nanoparticle precursor where Ag and Pt are present in a single hollow nanostructure which is stabilized by the formation of Pt oxides near the nanoparticle surface. We then take advantage of the strong interaction of Ag with visible light, manifested in the excitation of localized surface plasmon resonance (LSPR). The excitation of LSPR drives the reduction of the stabilizing Pt oxides in the bimetallic oxide precursor at room temperature preventing thermal phase separation. The reduction of the Pt oxides destabilizes the bimetallic precursor forcing the nanostructures to reconstruct into well-mixed Ag-Pt alloy nanoparticles. While we illustrate the approach by a concrete example, we believe that the underlying principles are transferable to the synthesis of other alloys containing plasmonic metals such as Au and Ag.

4.3 Methods

4.3.1 Nanoparticle Synthesis

Ag nanoparticle seeds were synthesized using a polyol method. In a typical synthesis, 5 mL of a 0.9 M polyvinylpyrrolidone (PVP, MW = 55,000, Sigma Aldrich) solution in ethylene glycol (VWR International, semi-grade) were added to 10 mL of ethylene glycol (preheated at 160°C for 1 hour). After 10 minutes, 3 mL of a 0.1 M solution of $AgNO_3$ (Acros Organics, ultrapure grade 99.5%) in ethylene glycol were quickly injected into the reaction vessel. The mixture was allowed to react for 30 minutes. For the galvanic replacement reaction, a stir bar was added to the reaction vessel containing the Ag nanoparticle seeds in ethylene glycol at 160°C. 3 mL of a 0.01 M aqueous solution of K_2PtCl_4 (Sigma Aldrich, 99.99%) were added slowly, drop-

wise to the reaction mixture. The reaction mixture was then allowed to reaction for 1 hour producing hollow Ag-Pt nanostructures capped with PVP.

The hollow nanostructures were washed three times in a 4:1 mixture of acetone:ethanol through centrifugation and re-dispersed in 10 mL of ethanol. This solution was allowed to sit overnight to allow AgCl crystals to settle out of solution. The solution of nanoparticles was decanted to remove the AgCl crystals. The solution was diluted to 50 mL with ethanol and 2 mL of a 25% ammonia solution and washed three times again via centrifugation. After the final wash, the solution was re-dispersed in 20 mL of ethanol. 5 mL of this nanoparticle solution was added to a slurry of 50 mg of fumed silica (Sigma Aldrich) in ethanol. This slurry was allowed to mix for 2 hours and then dried at 60°C. The nanoparticles were then heat treated at 300°C under air for 3 hours. At this point, the nanoparticles are ready for the light-mediated reduction as described in the manuscript. The light source used for illumination was a Dolan-Jenner Fiber-Lite 180 with a 150 W, 21 V halogen (EKE) lamp. The intensity of the light source was measured using a Newport thermopile detector.

4.3.2 Characterization

Scanning transmission electron microscopy (STEM) and energy-dispersive x-ray spectroscopy (EDS) were performed on a JEOL 3100R05 double Cs corrected TEM/STEM operated at 300 kV accelerating voltage. STEM samples were prepared colloidal nanoparticles were prepared by drop-casting on a carbon-on-copper 200 mesh grid. STEM samples of SiO_2-supported nanoparticle were prepared by sonicating the powder samples in a small amount of ethanol and drop casting on a carbon-on-copper 200 mesh grid. Elemental line scans of the nanoparticles were taken using a step size of 0.25 nm with a 5 second acquisition at each step. Line profiles were generated using the Ag Lα and Pt M transition peaks.

UV-vis extinction spectra was acquired using a ThermoFisher Scientific Evolution 300 spectrophotometer in transmission mode for colloidal solutions of nanoparticles and with a Harrick Praying Mantis diffuse reflectance accessory for powder samples. The diffuse reflectance spectra was normalized based on a pure silica spectrum and then the silica spectrum was subtracted from the nanoparticle/silica spectra to obtain the contribution solely from the nanoparticles. Samples for Raman spectroscopy were prepared by drop casting 100 μL out of 10 mL of the nanoparticle solution on a SiO_2 substrate. Raman spectra were collected using a 532 nm diode-pumped solid state laser and a confocal 50x objective lens on a Horiba LabRAM HR system equipped with a Horiba Synapse charge-coupled device (CCD). X-ray photoelectron spectra (XPS) were acquired using a Kratos Axis Ultra XPS with a monochromatic Al source (energy resolution ~0.5 eV). The escape depth of Pt4f photoelectrons is expected to be ~2 nm in this system.[12] Regional Pt4f scans were acquired using 10 sweeps with a dwell time of 60 seconds. Peak fitting was performed using CasaXPS software. Composition was calculated using built-in relative sensitivity factors (RSF). Powder x-ray diffraction data was acquired using Rigaku Miniflex x-ray diffractometer with Cu-Kα x-ray source operated at 40 kV and 15 mA and a scan speed of 4°/min.

4.4 Results and Discussion

To synthesize the bimetallic Ag/Pt-oxide nanoparticle precursor, we first used a seed-mediated galvanic replacement reaction to nucleate Pt atoms on premade Ag nanoparticles. Ag nanoparticles were synthesized in ethylene glycol at 160°C using polyvinylpyrrolidone (PVP) as a stabilizing agent and silver nitrate as a silver precursor following a well-established protocol.[13] The mixture was allowed to react for 1 hour, producing PVP-capped, spherical Ag nanoparticles ~ 60 nm in diameter, which acted as seeds for the subsequent deposition of Pt. An aqueous solution of K_2PtCl_4 was added dropwise to the reaction vessel containing the Ag nanoparticle seeds with

stirring at 160°C. Since Pt has a higher reduction potential than Ag, Pt ions galvanically replace Ag atoms from the Ag nanoparticle seeds ($2Ag^0 + Pt^{2+} \rightarrow 2Ag^+ + Pt^0$).[14] Previous reports of the galvanic replacement of Ag with Pt have shown that the reaction results in the formation of hollow Ag nanoparticles decorated with smaller Pt nanoparticles, i.e., Pt atoms galvanically displace bulk Ag atoms and nucleate on the surface.[15,16] To avoid the nucleation of separate Pt nanoparticles, we performed this reaction at an elevated temperature of 160°C, compared to 60-100°C reported in previous studies. In this case, the higher temperature increases the rate of diffusion of the Pt atoms over the Ag nanoparticles which promotes conformal coverage of Pt atoms on the Ag nanoparticles instead of island growth.[17]

The hollow Ag-Pt nanoparticles were washed three times via centrifugation with a 4:1 mixture of acetone and ethanol to remove excess PVP stabilizing agent and ions. We note that AgCl crystals, formed as a by-product of the galvanic replacement reaction, are not completely removed through washing because of the low solubility of AgCl in ethanol and acetone. To remove AgCl, the solution is set aside to allow the AgCl crystals to settle out of the solution and then decanted to remove the crystals. Ammonium hydroxide solution is then added to the solution of nanoparticles to dissolve any remaining AgCl and washed with ethanol via centrifugation.

To characterize the Ag-Pt nanostructures, scanning transmission electron microscopy (STEM) was performed after the removal of the AgCl crystals. The contrast observed in the bright-field image (Figure 4.1a) is evidence of the hollow structure of the Ag-Pt nanoparticles as the centers of the particles are less atomically dense, and hence a lighter shade, than the edges. Higher resolution bright-field images are shown in Figure 4.2. A dark-field image (Figure 4.1b), acquired using a high-angle annular dark-field detector (HAADF) for elemental contrast shows no evidence of individual Pt nanoparticles nucleated on the hollow nanostructures. The elemental composition

of the nanostructures was also studied using energy-dispersive x-ray spectroscopy (EDS). An EDS point spectrum (Figure 4.3) at the center of an individual hollow nanostructure shows that Ag and Pt are both present in the hollow nanoparticles. Data in Figure 4.1c show the elemental profile from the edge to the center of a representative nanoparticle. The elemental mapping data show that the intensity of the Pt signal compared to the intensity of the Ag signal is the highest close to the surface of the nanoparticle. Further into the particle bulk, the Pt intensity drops relative to the intensity of the Ag signal. This suggests that the near-surface region is enriched with Pt atoms compared to more interior regions of the nanoparticle and that Ag and Pt are not homogeneously mixed in these hollow nanostructures.

Ultraviolet-visible (UV-vis) light extinction spectroscopy was also used to characterize the dispersed nanoparticles confirming the conclusions of the STEM imaging. The optical extinction data for both the Ag nanoparticle seeds and the hollow Ag-Pt nanostructures are shown in Figure 4.1d. The optical extinction of the Ag nanoparticle seeds showed a strong peak centered ~ 430 nm attributed to the excitation of Ag localized surface plasmon resonance (LSPR).[18] The LSPR peak position is consistent with those previously reported of Ag nanoparticles of ~ 60 nm diameter.[19] This property is highly sensitive to changes in particle composition and morphology.[20] As the particle composition and structure change upon the introduction of the Pt ions from the solid spheres of monometallic Ag to the hollow structures of bimetallic Ag-Pt, the UV-vis extinction spectrum changes significantly. The hollow Ag-Pt nanostructures display a weak interaction with visible light with a broad extinction feature also attributed to the excitation of LSPR. The red-shifting of the plasmon extinction peak is primarily attributed to the change in particle structure whereas the weakening and broadening of the plasmon peak is attributed to coating and mixing of Pt at the surface.[15]
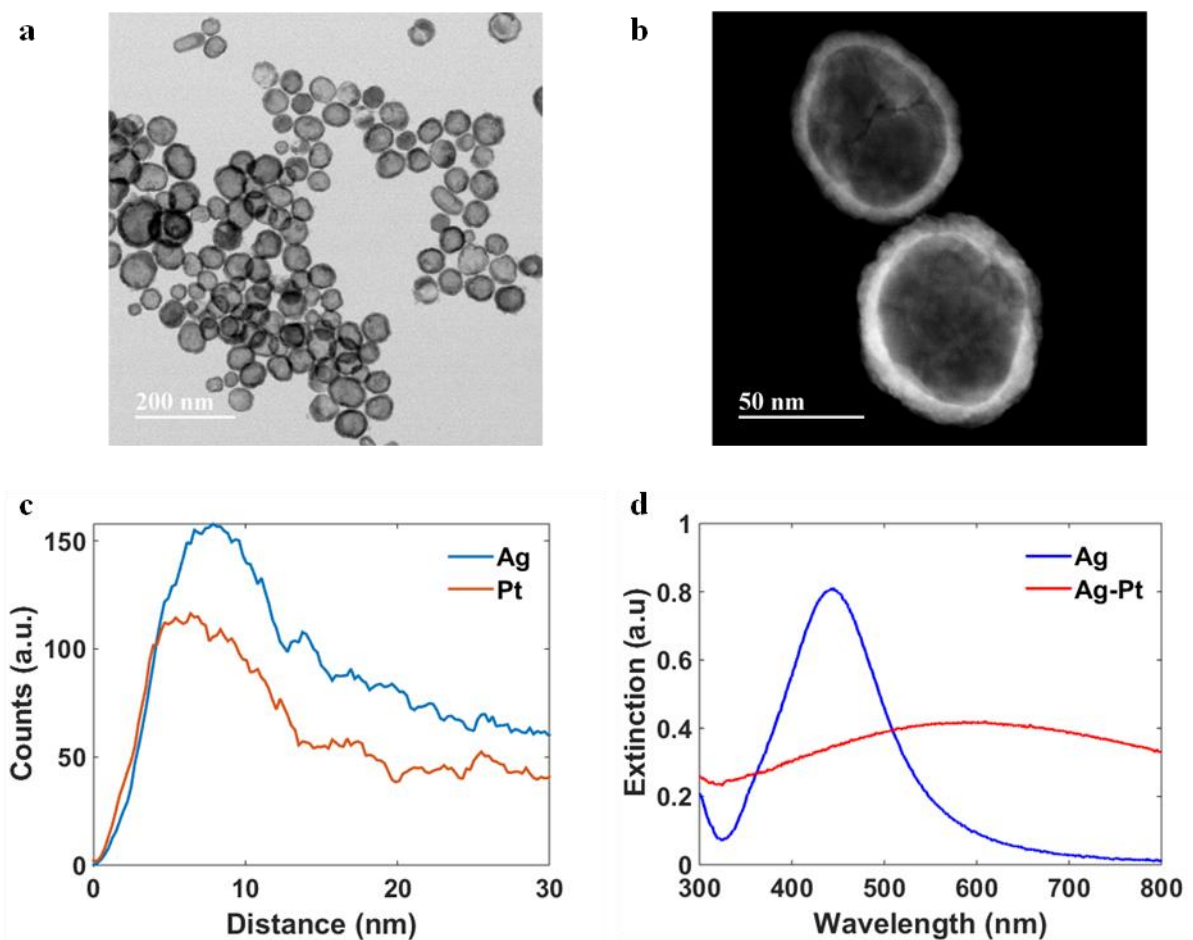
Figure 4.1 Characterization of hollow Ag-Pt nanoparticles. (a) Bright-field and **(b)** dark-field STEM images of hollow Ag-Pt nanostructures. **(c)** EDS line scan from the edge of a nanoparticle to the center. **(d)** Optical extinction of Ag nanoparticle seeds in ethanol and the hollow Ag-Pt nanostructures in ethanol.
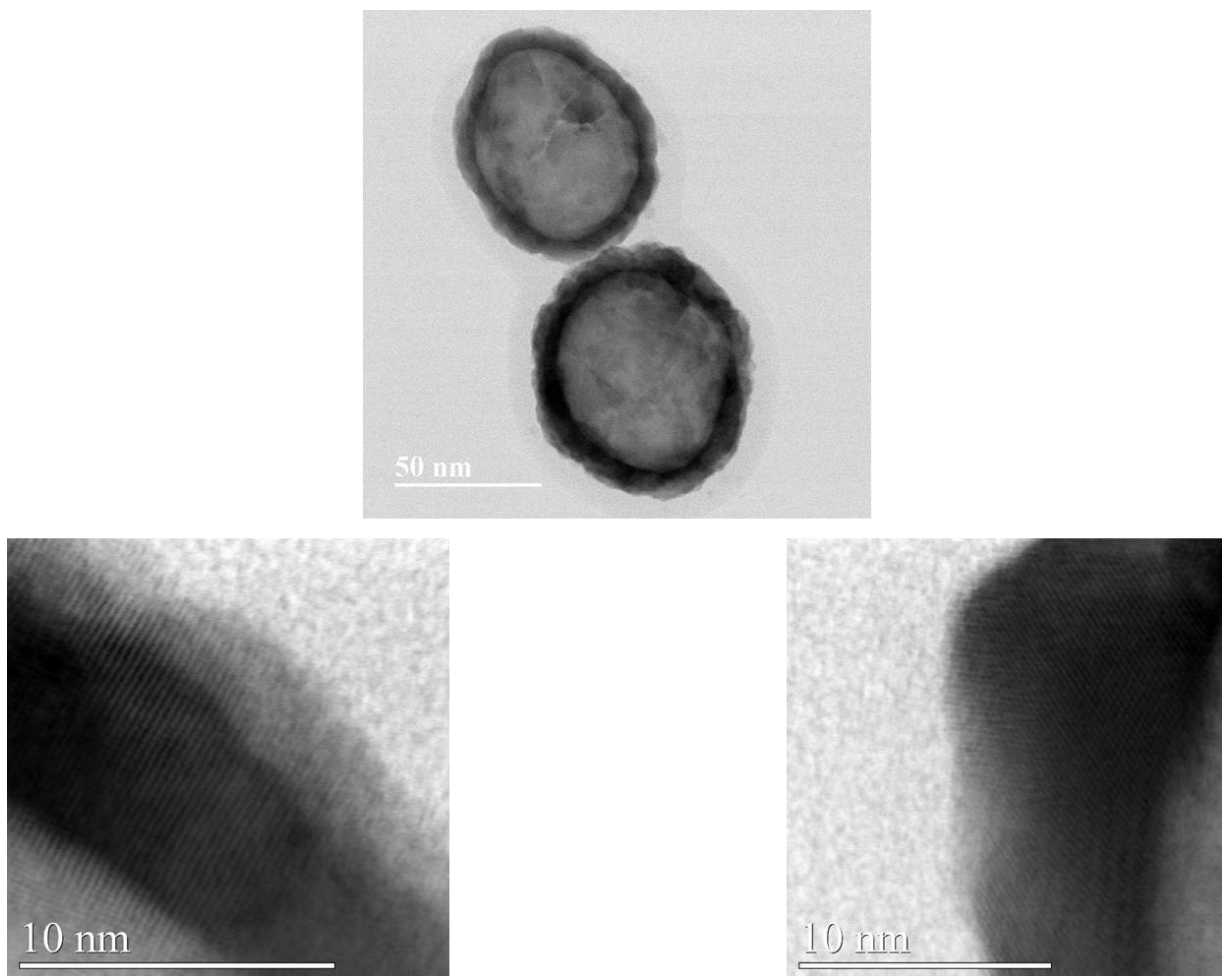
Figure 4.2 Bright field TEM images of hollow Ag-Pt nanoparticles. Bright-field TEM image of Ag-Pt hollow particles after synthesis. The very light shaded material around the nanoparticles is believed to be PVP from the colloidal synthesis. The high resolution bright field images confirm the crystalline nature of the nanoparticles.

Figure 4.3 EDS point scan of Ag-Pt hollow nanoparticles. EDS point spectrum of a hollow Ag-Pt nanostructure as-synthesized. The Pt M and Ag Lα signals are clearly visible in the spectrum. The smaller peaks to the right of the Ag Lα peak are also associated with Ag. The lower energy peaks are from carbon and lithium from EDS detector.

To further characterize the hollow Ag-Pt nanoparticles, the nanoparticles were deposited on a SiO_2 substrate and probed using Rama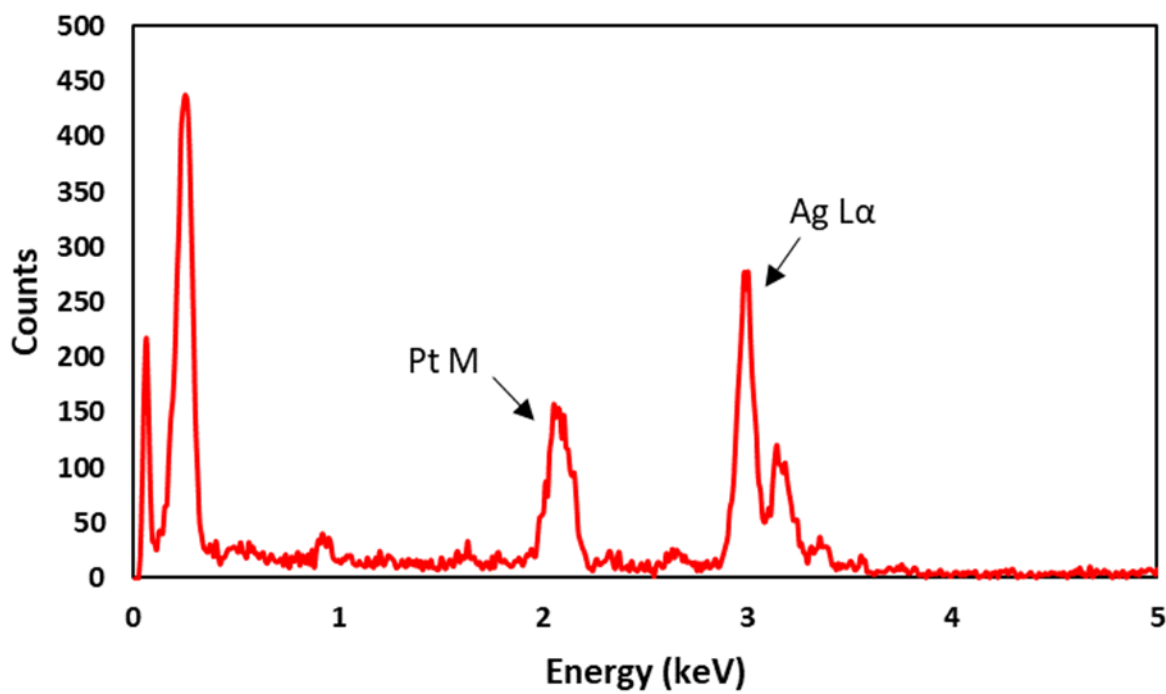n and x-ray photoelectron spectroscopies (XPS). The Raman spectrum in Figure 4.4a displays broad extinction features at ~ 1350 and 1600 cm^{-1}. These features have been assigned to PVP on the surface of the nanostructures.[21] The PVP molecules are most likely strongly bound to the Ag nanoparticles as they were not removed during the above-described washing steps. The XPS data focusing on the core Pt4f electrons (Figure 4.4b) display a single doublet peak, characteristic of Pt atoms in the metallic Pt^0 state. The data in Figure 4.1 and Figure 4.4a-b paint a picture of hollow metallic Ag-Pt nanoparticles, perhaps stabilized with strongly bound PVP molecules.

To remove PVP from the hollow nanoparticles, the nanoparticles were heat treated in air at 300°C for 3 hours. Raman spectrum collected after this heat treatment showed no signs of PVP on the surface of the nanostructure, suggesting that most of the PVP molecules were oxidized in this process. Dark-field STEM characterization shows that the hollow structure of the nanoparticles was not affected by the heat treatment (Figure 4.4c). In contrast, the Pt4f XPS data after thermal removal of PVP show that the chemical signature of the Pt atoms in the hollow nanoparticles changed. The XP spectrum showed five individual peaks which indicate that Pt exists in multiple oxidation states near the surface of the nanoparticles.[22] Through deconvolution of the Pt4f XP spectrum, shown in Figure 4.4d, it was established that Pt atoms exist in Pt^0, Pt^{2+}, and Pt^{4+} oxidation states, indicating the formation of Pt oxides near the surface of the nanoparticles after the thermal treatment.[23] This newly formed Pt oxide at the surface of the hollow structure serve to stabilize the hollow geometry.
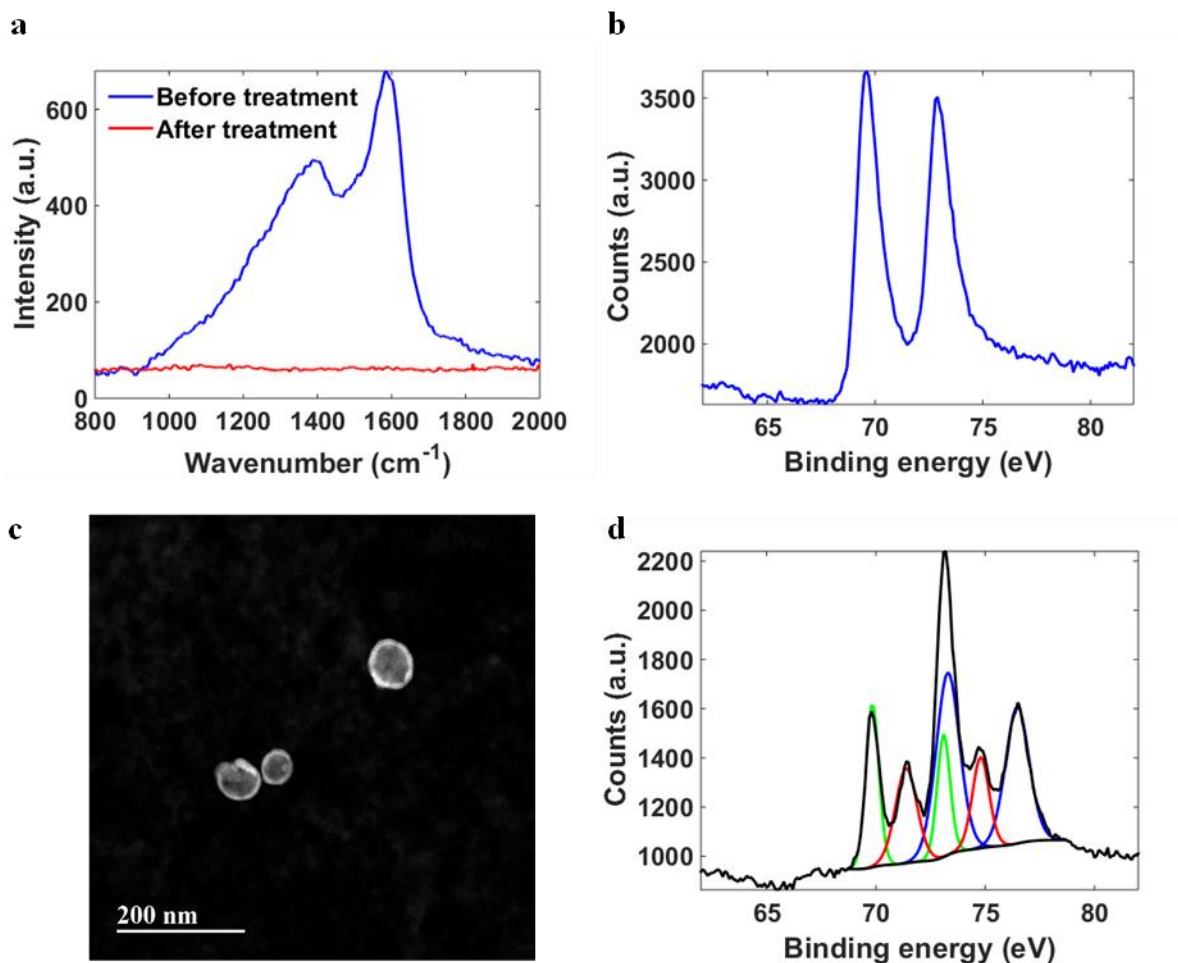
Figure 4.4 Characterization of oxidized hollow Ag-Pt nanoparticles. **(a)** Raman spectra showing PVP present on the surface of the hollow nanostructures and removal of PVP using a thermal treatment in air at 300°C for 3 hours. **(b)** Pt4f XP spectrum for PVP-capped hollow nanoparticles with a single doublet characteristic of Pt metal. **(c)** STEM image of nanoparticles after the thermal treatment shows no significant change in particle morphology. **(d)** Pt4f XP spectrum for hollow Ag/Pt-oxide nanoparticles. Six individual peaks are identified corresponding to Pt^0 (green), Pt^{2+} (red), and Pt^{4+} (blue).

The data in Figures 4.1 – 4.4 above confirm the synthesis of hollow nanostructures containing mixed Ag and Pt atoms stabilized by the presence of Pt oxide near the surface of the nanostructure. To move from this bimetallic hollow nanostructure containing Pt oxide and to form solid bimetallic alloy nanoparticles, it is necessary to reduce the surface oxide, preferably at low temperatures to minimize the thermodynamically-driven phase separation of Pt and Ag. To accomplish this objective we attempt to take advantage of the optical properties of nanostructured Ag, manifested in the excitation of localized surface plasmon resonance (LSPR). Nanostructures of Ag, Au, and Cu undergo an excitation of LSPR when interacting with visible light.[24] The LSPR results in a significant accumulation of electromagnetic energy in the nanostructure.[25] It has been demonstrated previously that this energy can bring about the light-induced reduction of Cu-oxide shell supported on metallic Cu core in Cu/Cu-oxide core/shell nanoparticles.[26] We hypothesize that the excitation of Ag LSPR in the hollow Ag/Pt-oxide nanostructures through visible light irradiation would reduce the Pt oxide thereby destabilizing the particles and collapsing the hollow nanostructure into solid Ag-Pt alloy nanoparticles.

To test this hypothesis, hollow Ag/Pt-oxide nanoparticles supported on SiO_2 were loaded into a gas-tight flow chamber allowing for visible light irradiation. The chamber was kept under N_2 flow at room temperature for 1 hour and subsequently illuminated with visible light at an intensity of ~600 mW/cm^2 for 2 hours at room temperature. The nanoparticles were characterized using diffuse reflectance UV-vis spectroscopy. The diffuse reflectance data in Figure 5a show that the optical properties of the nanoparticles change significantly after visible light illumination. Before visible light irradiation, the data show a broad and relatively featureless optical absorption characteristic of the bimetallic hollow oxide nanostructures. After illumination, a more defined spectral feature at shorter wavelength emerges in the spectrum. This optical feature is consistent

with the LSPR excitations of solid Ag and Ag alloy nanoparticles.[27,28] The changes in the optical properties of the nanostructures suggest that the nanoparticles undergo structural changes after visible light excitation consistent with the formation of solid nanostructures. XPS was used to characterize the LSPR induced changes in the chemical composition of the nanoparticles after visible light excitation (Figure 4.5b). The data show a single doublet for Pt4f near the surface of the nanoparticles confirming that Pt oxide was reduced into metallic Pt. No changes were observed in the Ag3d XPS data (Figure 4.6).
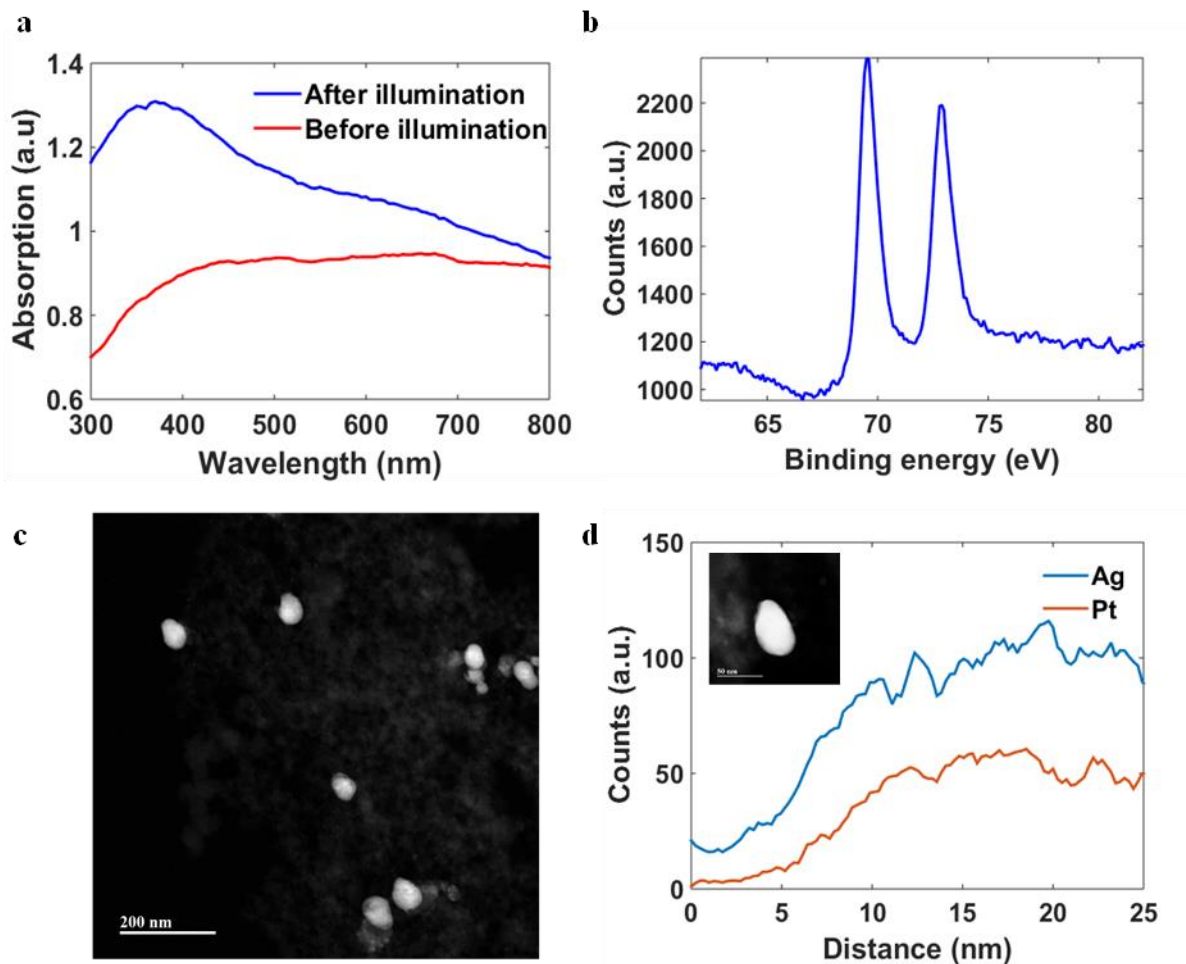
Figure 4.5 Characterization of light-reduced Ag-Pt alloy nanoparticles. (a) Diffuse reflectance UV-vis data for hollow nanostructures before and after visible light excitation. **(b)** Pt4f XPS data of nanoparticles after visible light excitation. **(c)** STEM image of Ag-Pt nanoparticles after visible light-mediated reduction of surface Pt oxides. **(d)** EDS line scan from edge to center of a nanoparticle.

Figure 4.6 XPS data for Ag. (a) Ag3d XPS data of the hollow nanostructures after heat treatment and **(b)** solid alloy nanostructures (right). In both cases, we observe a single doublet characteristic of metallic Ag.

The fraction of Pt atoms near the surface of the nanoparticle, as calculated by quantifying the XPS data, decreased from ~ 14% before to ~ 7% after visible light illumination suggesting that the reduction of the surface Pt oxide was accompanied with the diffusion of Pt atoms into the bulk of the nanostructure and the creat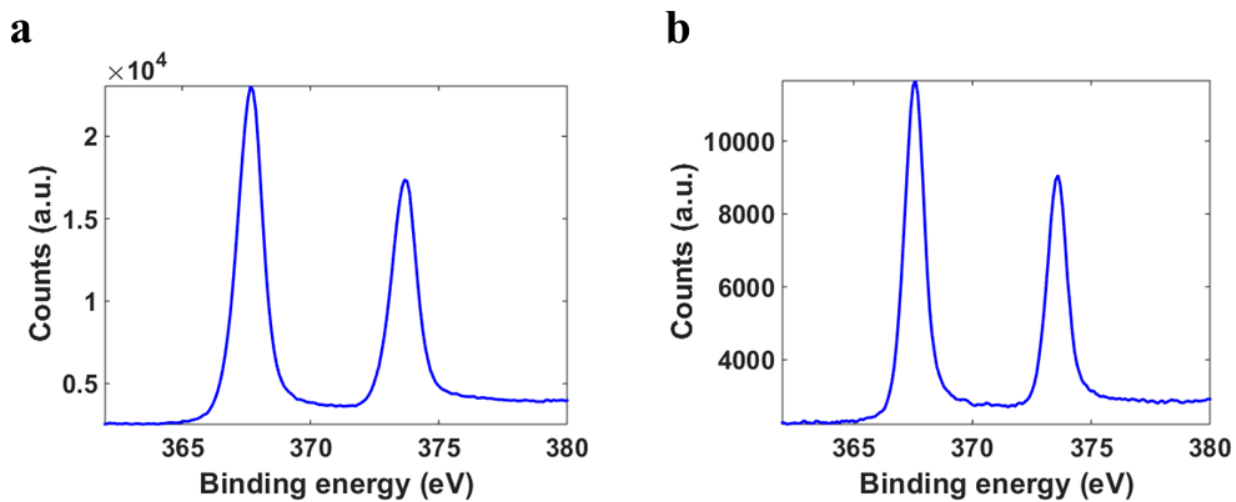ion of mixed solid Ag-Pt alloy nanoparticles. This is supported by the STEM images in Figure 5c which show that the nanoparticles no longer maintained their hollow structure but instead appear to be solid. Additionally, this change in particle morphology was accompanied by a decrease in average particle diameter from 53.5±13.6 nm to 42.6±7.7 nm (Figures 4.7). Powder X-ray diffraction data (Figure 4.8) also suggests the formation of Ag-Pt alloy nanoparticles. An EDS point spectrum at the center of a representative nanoparticle shows the presence of both Ag and Pt in the nanostructure (Figure 4.9). Also, an EDS elemental line profile (Figure 4.5d) from the edge to the center of a representative nanoparticle shows that the ratio of the Ag to Pt signal is fairly constant across the nanoparticle consistent with the formation of homogeneous Ag-Pt bimetallic alloy nanoparticles.
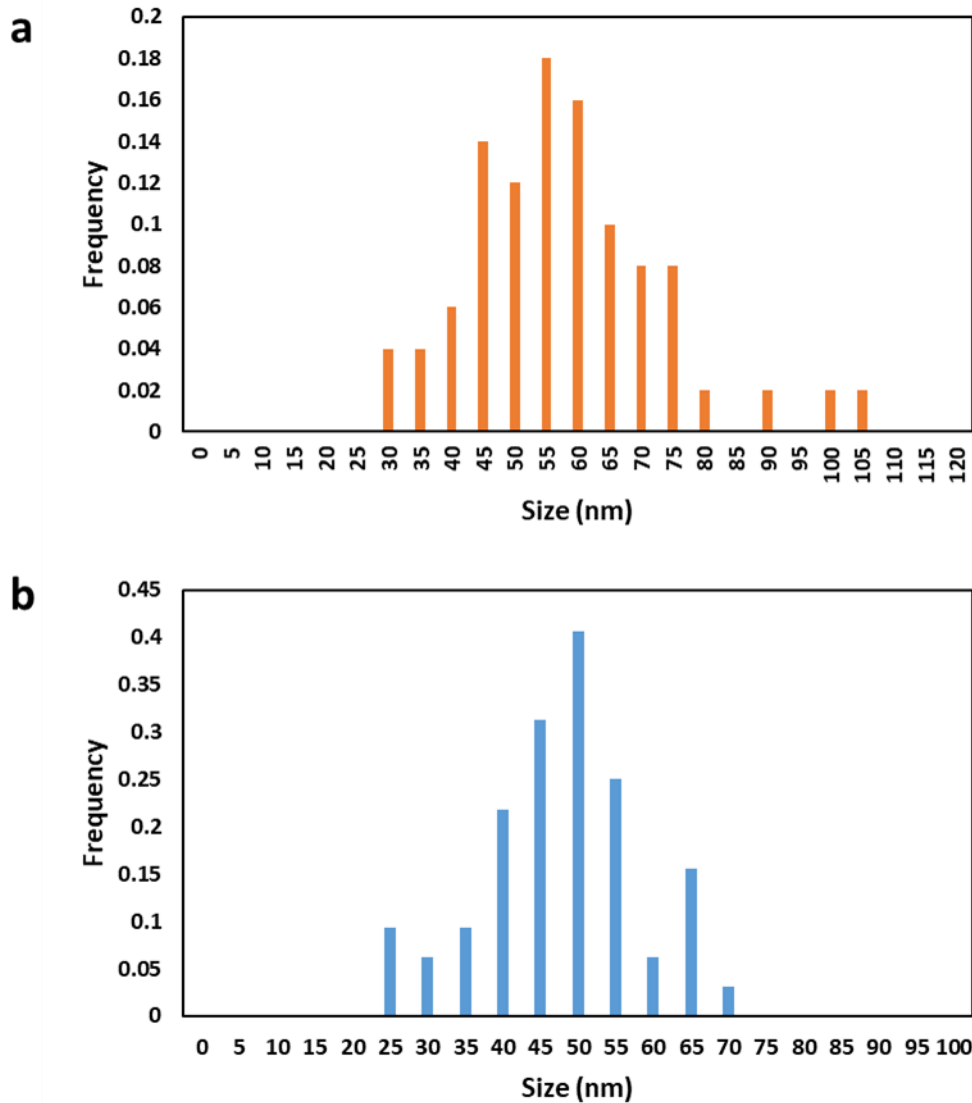
Figure 4.7 Particle size distributions of hollow and alloy Ag-Pt nanoparticles. (a) Particle size distribution for Ag-Pt hollow nanoparticles before illumination. The average diameter of the nanoparticles was 53.5 nm with a standard deviation of 13.6 nm. **(b)** Particle size distribution of Ag-Pt solid alloy nanoparticles. The average diameter of the nanoparticles was 42.6 nm with a standard deviation of 7.7 nm.
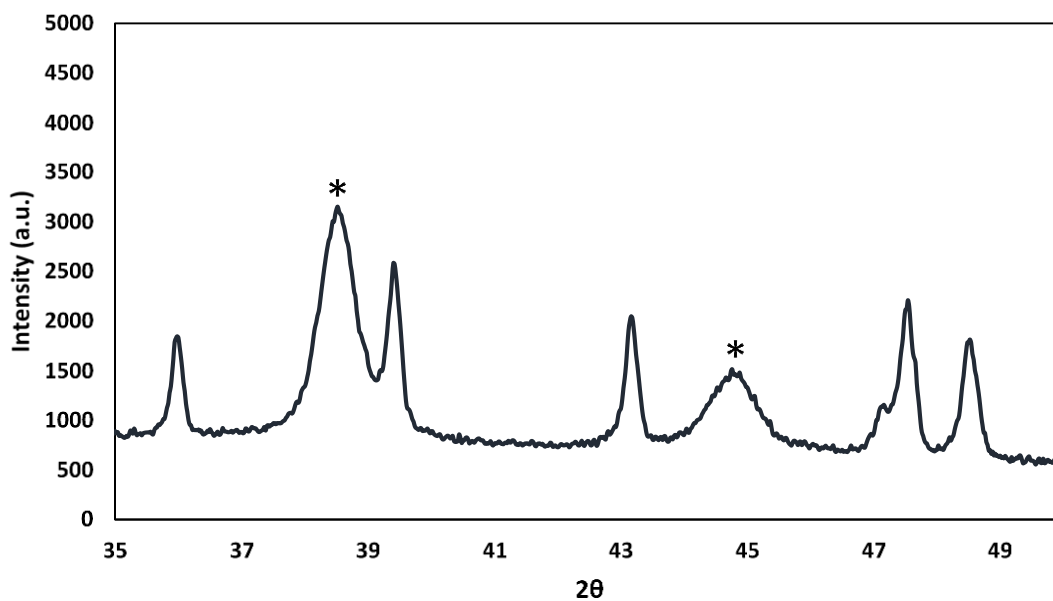
Figure 4.8 XRD data for Ag-Pt alloy nanoparticles. Powder x-ray diffraction of alloyed nanoparticles. The two starred peaks are for the metal nanoparticles whereas the other peaks are from the underlying Si substrate and Al sample holder. The metal diffraction peaks for the alloy are at 2θ values of $38.5°$ and $44.8°$ which is between the diffraction peaks of pure Ag and Pt.
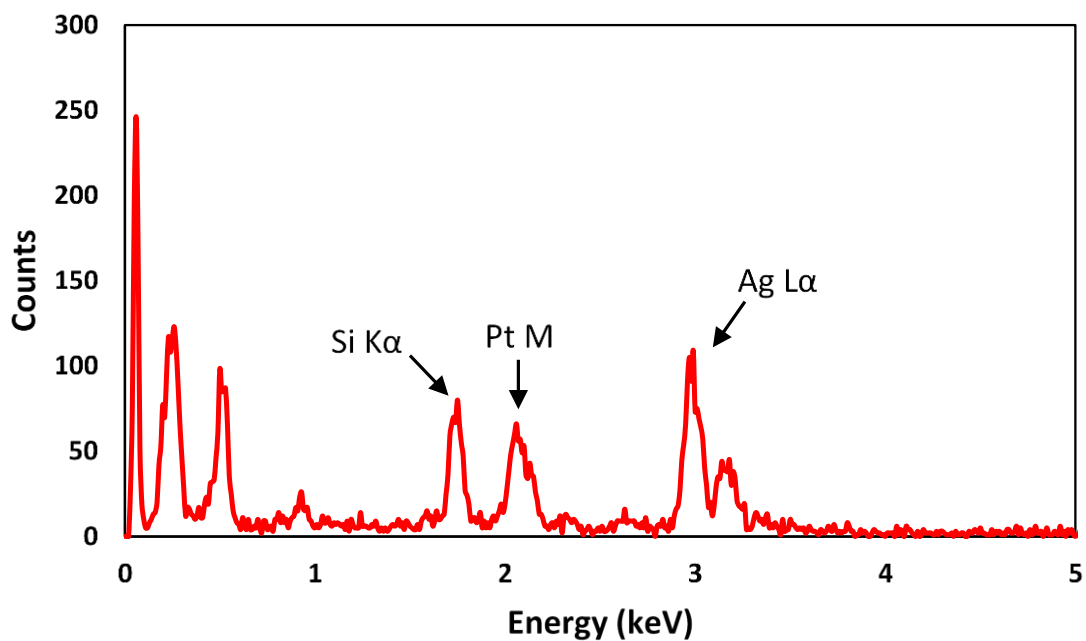
Figure 4.9 EDS point spectrum of alloy Ag-Pt nanoparticles. EDS point spectrum of alloyed Ag-Pt nanoparticle after light exposure. Again, the Pt M and Ag Lα peaks are clearly visible in the spectrum. The other peaks include silicon and oxygen from the SiO_2 support, carbon, and lithium from the EDS detector.

The data above show that solid bimetallic alloy Ag-Pt nanoparticles are formed by the reconstruction of the hollow nanostructures after visible light-mediated reduction of the Pt surface oxides. While the exact mechanism of the particle restructuring has not been investigated in this study, it is obvious that the oxidized surface Pt atoms are essentially pinned to the surface of the hollow nanostructures and that these atoms served to stabilize the hollow structure. It is also clear that the shedding of the surface oxide, induced by the visible light illumination, was accompanied by a prompt mixing of Ag and Pt atoms, which circumvented the phase separation of the two metals. This rapid mixing seems to be driven by the thermodynamic driving force for the hollow nanostructure to minimize its energy by filling the void in the core of the nanoparticles, i.e., coordinating the inner surface of the nanostructure and thus lowering its energy. This leads to the diffusion of metal atoms inwards forcing the surface segregated Pt atoms (from the Pt-oxide shell) to mix with Ag atoms as the nanoparticle restructures eventually forming solid, well-mixed Ag-Pt alloy nanoparticles.

It is important to note that the reduction of the Pt oxide does not take place simply by heating the nanoparticles even when exposed to temperatures as high as 300 °C for several hours. This suggests that the light-mediated reduction of Pt oxide was not due to light-mediated homogeneous heating of the nanostructures.[29] As mentioned earlier, it has previously been demonstrated that visible light can be used to reduce a surface oxide on plasmonic Cu/Cu-oxide core/shell nanoparticles.[26] This reduction was attributed to the excitation of surface plasmon resonance in the metallic core of the nanoparticles. In the case discussed herein, we speculate that the electromagnetic energy concentrated in the hollow Ag-Pt nanoparticle under the LSPR conditions leads to the reduction of the Pt-oxide at the surface of the hollow nanostructures, nucleating the chain of events leading to the formation of solid alloy nanoparticles.

We note that LSPR excitation concentrates the energy of the incoming electromagnetic radiation at the surface of the plasmonic nanostructures in the form of intense, oscillating electric fields.[30] These intense fields can decay by exciting charge carriers within the hollow nanoparticles which can lead to reduction of Pt oxide through population of anti-bonding Pt-O orbitals and weakening Pt-O bonds. There are three potential charge excitation events that can take place and aid in the reduction of the Pt oxide. First excitation of charge carriers can take place exclusively in the Pt oxide where electrons are promoted from Pt-O bonding to the antibonding orbitals. Plasmonic metals have been shown to intensify these charge excitation events by concentrating the incoming photon flux through LSPR excitation.[31,32] Another mechanism involves excitation of charge carriers in Ag, followed by the transfer of energetic charge carriers from Ag to the anti-bonding Pt-O states.[33,34] The net effect would be that the Pt oxide is promoted to a higher-energy, charged state which relieves this energy by reducing the oxide. Finally, the charge excitation can take place at the interface of Ag and Pt oxide. In this case, charge carriers are excited directly from Ag to the oxide under the influence of the high interfacial electric field.[35,36]

4.5 Conclusions

We have demonstrated a method for synthesizing alloy nanoparticles of immiscible Ag and Pt metals through the reduction of a bimetallic precursor at room temperature using visible light. The bimetallic precursor was formed by reducing Pt atoms on Ag nanoparticles through a galvanic replacement reaction, which led to the formation of hollow bimetallic nanoparticles that were stabilized by the presence of Pt-oxide at the surface of the nanoparticles. To form mixed alloy nanoparticles, the surface Pt oxide of the hollow nanostructure was reduced by taking advantage of the optical properties of Ag-based nanoparticles manifested by surface plasmon resonance.

Visible light irradiation resulted in the reduction of the Pt oxide and the restructuring of the hollow nanostructures into solid Ag-Pt bimetallic alloys.

Although we are able to successfully produce Ag-Pt alloy nanoparticles using this method, it is difficult to perform this synthesis at large scales which is necessary to test the catalytic performance of these materials. It is also challenging to perform experiments to probe the optical properties and flow of energy in these nanostructures due to the presence of the SiO_2 support. Ideally, we would like to synthesis Ag-Pt nanoparticles in colloidal solutions which can then be easily analyzed using optical spectroscopy tools to study the flow of energy in bimetallic, plasmonic-catalytic nanoparticles. We discuss our efforts in this endeavor in the next chapter.

4.6 References

1. Gilroy, K. D., Ruditskiy, A., Peng, H.-C., Qin, D. & Xia, Y. Bimetallic Nanocrystals: Syntheses, Properties, and Applications. *Chem. Rev.* **116,** 10414–10472 (2016).

2. Wang, D. & Li, Y. Bimetallic Nanocrystals: Liquid-Phase Synthesis and Catalytic Applications. *Adv. Mater.* **23,** 1044–1060 (2011).

3. Ferrando, R., Jellinek, J. & Johnston, R. L. Nanoalloys: From Theory to Applications of Alloy Clusters and Nanoparticles. *Chem. Rev.* **108,** 845–910 (2008).

4. Cortie, M. B. & McDonagh, A. M. Synthesis and Optical Properties of Hybrid and Alloy Plasmonic Nanoparticles. *Chem. Rev.* **111,** 3713–3735 (2011).

5. Karakaya, I. & Thompson, W. T. The Ag−Pd (Silver-Palladium) system. *Bulletin of Alloy Phase Diagrams* **9,** 237–243 (1988).

6. Okamoto, H. & Massalski, T. B. The Ag−Au (Silver-Gold) system. *Bulletin of Alloy Phase Diagrams* **4,** 30–38 (1983).

7. Zhang, Z., Nenoff, T. M., Huang, J. Y., Berry, D. T. & Provencio, P. P. Room Temperature Synthesis of Thermally Immiscible Ag−Ni Nanoalloys. *J. Phys. Chem. C* **113,** 1155–1159 (2009).

8. Marbella, L. E. *et al.* Description and Role of Bimetallic Prenucleation Species in the Formation of Small Nanoparticle Alloys. *J. Am. Chem. Soc.* **137,** 15852–15858 (2015).

9. Holewinski, A., Idrobo, J.-C. & Linic, S. High-performance Ag–Co alloy catalysts for electrochemical oxygen reduction. *Nat Chem* **6,** 828–834 (2014).

10. Zhang, S. *et al.* Dynamic structural evolution of supported palladium-ceria core-shell catalysts revealed by in situ electron microscopy. *Nat Commun* **6,** 7778 (2015).

11. Karakaya, I. & Thompson, W. T. The Ag-Pt (Silver-Platinum) system. *Bulletin of Alloy Phase Diagrams* **8,** 334–340 (1987).

12. Powell, C. J. & Jablonski, A. Evaluation of Calculated and Measured Electron Inelastic Mean Free Paths Near Solid Surfaces. *Journal of Physical and Chemical Reference Data* **28,** 19–62 (1999).

13. Christopher, P. & Linic, S. Shape- and Size-Specific Chemistry of Ag Nanostructures in Catalytic Ethylene Epoxidation. *ChemCatChem* **2,** 78–83 (2010).

14. Cobley, C. M. & Xia, Y. Engineering the properties of metal nanostructures via galvanic replacement reactions. *Materials Science and Engineering: R: Reports* **70,** 44–62 (2010).

15. Chen, J. *et al.* Optical Properties of Pd−Ag and Pt−Ag Nanoboxes Synthesized via Galvanic Replacement Reactions. *Nano Lett.* **5,** 2058–2062 (2005).

16. Lee, C.-L. & Tseng, C.-M. Ag−Pt Nanoplates: Galvanic Displacement Preparation and Their Applications As Electrocatalysts. *J. Phys. Chem. C* **112,** 13342–13345 (2008).

17. Xie, S. *et al.* Atomic Layer-by-Layer Deposition of Pt on Pd Nanocubes for Catalysts with Enhanced Activity and Durability toward Oxygen Reduction. *Nano Lett.* **14,** 3570–3576 (2014).

18. Marimuthu, A., Christopher, P. & Linic, S. Design of Plasmonic Platforms for Selective Molecular Sensing Based on Surface-Enhanced Raman Spectroscopy. *J. Phys. Chem. C* **116,** 9824–9829 (2012).

19. Evanoff, D. D. & Chumanov, G. Size-Controlled Synthesis of Nanoparticles. 1. "Silver-Only" Aqueous Suspensions via Hydrogen Reduction. *J. Phys. Chem. B* **108,** 13948–13956 (2004).

20. Skrabalak, S. E., Au, L., Li, X. & Xia, Y. Facile synthesis of Ag nanocubes and Au nanocages. *Nat. Protocols* **2,** 2182–2190 (2007).

21. Borodko, Y., Lee, H. S., Joo, S. H., Zhang, Y. & Somorjai, G. Spectroscopic Study of the Thermal Degradation of PVP-Capped Rh and Pt Nanoparticles in H2 and O2 Environments. *J. Phys. Chem. C* **114,** 1117–1126 (2010).

22. Salmerón, M., Brewer, L. & Somorjai, G. A. The structure and stability of surface platinum oxide and of oxides of other noble metals. *Surface Science* **112,** 207–228 (1981).

23. Peuckert, M. & Bonzel, H. P. Characterization of oxidized platinum surfaces by X-ray photoelectron spectroscopy. *Surface Science* **145,** 239–259 (1984).

24. Linic, S., Christopher, P. & Ingram, D. B. Plasmonic-metal nanostructures for efficient conversion of solar to chemical energy. *Nat Mater* **10,** 911–921 (2011).

25. Kelly, K. L., Coronado, E., Zhao, L. L. & Schatz, G. C. The Optical Properties of Metal Nanoparticles: The Influence of Size, Shape, and Dielectric Environment. *J. Phys. Chem. B* **107,** 668–677 (2002).

26. Marimuthu, A., Zhang, J. & Linic, S. Tuning Selectivity in Propylene Epoxidation by Plasmon Mediated Photo-Switching of Cu Oxidation State. *Science* **339,** 1590–1593 (2013).

27. Rycenga, M. *et al.* Controlling the Synthesis and Assembly of Silver Nanostructures for Plasmonic Applications. *Chem. Rev.* **111,** 3669–3712 (2011).

28. Link, S., Wang, Z. L. & El-Sayed, M. A. Alloy Formation of Gold−Silver Nanoparticles and the Dependence of the Plasmon Absorption on Their Composition. *J. Phys. Chem. B* **103,** 3529–3533 (1999).

29. Kale, M. J., Avanesian, T. & Christopher, P. Direct Photocatalysis by Plasmonic Nanostructures. *ACS Catal.* **4,** 116–128 (2014).

30. Linic, S., Aslam, U., Boerigter, C. & Morabito, M. Photochemical transformations on plasmonic metal nanoparticles. *Nat Mater* **14,** 567–576 (2015).

31. Naldoni, A. *et al.* Solar-Powered Plasmon-Enhanced Heterogeneous Catalysis. *Nanophotonics* **5,** 112–133 (2016).

32. Ingram, D. B. & Linic, S. Water Splitting on Composite Plasmonic-Metal/Semiconductor Photoelectrodes: Evidence for Selective Plasmon-Induced Formation of Charge Carriers near the Semiconductor Surface. *J. Am. Chem. Soc.* **133,** 5202–5205 (2011).

33. Frischkorn, C. & Wolf, M. Femtochemistry at Metal Surfaces: Nonadiabatic Reaction Dynamics. *Chem. Rev.* **106,** 4207–4233 (2006).

34. Lindstrom, C. D. & Zhu, X.-Y. Photoinduced Electron Transfer at Molecule−Metal Interfaces. *Chem. Rev.* **106,** 4281–4300 (2006).

35. Boerigter, C., Campana, R., Morabito, M. & Linic, S. Evidence and implications of direct charge excitation as the dominant mechanism in plasmon-mediated photocatalysis. *Nat Commun* **7,** 10545 (2016).

36. Boerigter, C., Aslam, U. & Linic, S. Mechanism of Charge Transfer from Plasmonic Nanostructures to Chemically Attached Materials. *ACS Nano* **10,** 6108–6115 (2016).

Chapter 5 Synthesis of Ag-Pt Core-Shell Nanocubes

5.1 Summary

We hypothesized that one design of bimetallic nanoparticles that would display the optical properties of Ag and perform the surface chemistry of Pt could be obtained by coating ultrathin (~ 1 nm) shells of Pt onto Ag nanoparticle cores. Current synthesis methods for producing such core-shell nanostructures often require incremental addition of a shell metal precursor which is rapidly reduced onto metal cores. Using this approach, we are able to synthesis Ag-Pt core-shell nanoparticles; however, a major shortcoming of this approach is that it necessitates precise concentrations of chemical reagents making it difficult to perform at large scales. To address this issue, we consider an approach whereby the reduction of the shell metal precursor is controlled through in-situ chemical modification of the precursor. We use this approach to develop a highly-scalable synthesis for coating atomic layers of Pt onto Ag nanocubes. We show that Ag-Pt core-shell nanostructures are synthesized in high yields and that these structures effectively combine the optical properties of the plasmonic Ag nanocube core with the surface chemical properties of the thin Pt shell. Additionally, we demonstrate the scalability of the synthesis by performing a 10 times scale up.

5.2 Introduction

A commonly desired configuration of bimetallic nanoparticles is that of core-shell nanostructures in which a "core" metal is surrounded by a thin layer of a second metal.[1–3] There are several appealing features to this architecture, including: (i) the shell metal can provide mechanical, thermal, or chemical stability for the core metal, (ii) the core of an expensive metal can be substituted for a cheap metal to reduce the overall cost, and (iii) the chemical reactivity of a shell metal can be perturbed by a core metal through a combination of ligand and strain effects.[4–8] In this dissertation, we are interested in metallic core/thin-shell nanoparticles in order to combine the optical properties of a metal core with the surface properties of a shell metal. Specifically, we aim to coat a plasmonic metal nanoparticle with a very thin layer of another metal as we hypothesize that these core-shell nanostructures will retain the optical properties of the plasmonic core while exhibiting surface properties associated with the shell metal. Beyond plasmonic catalysis, these hybrid plasmonic structures could also be useful for a number of applications such as surface-enhanced Raman spectroscopy, photothermal plasmonic heating, and cancer therapy.[9–12]

Typically, the synthesis of bimetallic core-shell nanoparticles employs a seed-mediated approach whereby nanoparticles of the core metal are used as seeds and a metal precursor for the shell metal is deposited onto the seeds using a chemical reducing agent.[13–16] Herein, we develop a synthesis for coating a few atomic layers of Pt onto Ag nanocubes using such an approach. We use a dilute solution of Ag nanocube seeds combined with a strong reducing environment to quickly reduce a dilute Pt precursor onto the surface of the nanoparticles over the course of several hours. While this method allows us to synthesize Ag-Pt core-shell nanoparticles, the approach suffers from two major drawbacks. The first issue is related to the scalability. To minimize side reactions

such as uncontrolled homogeneous nucleation of the shell material, it is necessary to keep the concentration of the shell metal precursor in a mixture of seed cores very low. This is accomplished by very slow injection of the precursor into the mixture under strong reducing conditions. It has been widely recognized that it is difficult to implement such a synthesis at large scales as the reaction volume must be increased proportionally to maintain the appropriate low concentrations of all chemical reagents.[17–19] Another issue which affects some combinations of metals (such as Ag and Pt) is related to the spontaneous galvanic replacement of a core metal with the shell metal, which can lead to uncontrollable evolution of the nanostructure.[20,21]

Given that our primary interest lay in performing plasmon-enhanced chemical reactions on these core-shell nanoparticles, we set out to develop a robust and easily-scalable synthesis method for coating a thin layer of Pt onto Ag nanocube seeds. We show that by chemically modifying a Pt metal complex under the condition of synthesis, we can decrease the reduction potential of the Pt precursor, and in doing so prevent homogeneous reduction of the Pt metal precursor and the detrimental galvanic replacement of Ag by Pt. We demonstrate that this approach makes the synthesis much less sensitive to the concentration of chemical reagents in the reaction vessel, allowing large scale syntheses to be performed. We also show that by employing this approach we have excellent control of the Pt shell thickness ranging from 0.6-1.4 nm, and that we are able to synthesize high yields of the core-shell nanostructures with uniform Pt shell thickness.

5.3 Methods

5.3.1 Synthesis of Ag Nanocube Seeds

Ag nanocubes are synthesized using a well-established polyol synthesis, as detailed in Chapter 3.[22,23] The exact recipe used in this work is as follows. A 20 mL glass vial containing 10 mL of ethylene glycol (VWR International, semigrade) is heated to 140°C in an oil bath. After

heating for 1 hour, 80 µL of a 36 mM aqueous HCl solution are added to the reaction mixture followed by the addition of 5 mL of a 10 mg/mL solution of polyvinylpyrrolidone (PVP, MW=55,000 Sigma Aldrich) in ethylene glycol. Then 2 mL of a 25 mg/mL solution of $AgNO_3$ (Acros Organics, ultrapure grade 99.5%) are added to the reaction mixture and a ventilated cap is placed on the reaction vessel to allow air to enter the system while also refluxing ethylene glycol. After ~24 hours, the ventilated cap is exchanged for a sealed cap to prevent air from entering the reaction mixture. The nanocubes are allowed to grow for ~8 hours and then quenched. For washing and purification, the Ag nanocubes in ethylene glycol are diluted with acetone to 45 mL and centrifugated for 20 minutes at 8,000 rpm to separate the nanoparticles from excess chemical reagents. The supernatant was discarded and the nanocubes were redispersed in 5 mL of DI water. The nanoparticles are washed twice more by diluting the redispersed nanoparticles to 45 mL with acetone, separating the nanocubes via centrifugation for 20 minutes at 8,000 rpm, and redispersing in 10 mL of DI water. The concentration of the nanoparticles is estimated by measuring the mass of 1 mL of dried Ag nanocubes.

5.3.2 Small Scale Ag-Pt Core-Shell Nanocube Synthesis

In a typical synthesis, 1/10th of a solution of Ag nanocubes is diluted to 3 mL with water and is mixed with 50 mg of PVP. The Pt precursor is prepared fresh in a separate container by adding 12 mg of K_2PtCl_4 (Sigma Aldrich, 99.99%) to 16 mL of DI water. The reducing agent is also prepared in a separate container by adding 100 mg of ascorbic acid to 3 mL of DI water followed by the addition of 600 µL of an aqueous 1.25 M NaOH solution. The reducing agent mixture is then added to the reaction vessel. The Pt precursor solution is slowly added to the reaction vessel using a syringe pump at a rate of 4 mL/hr. Every 2 hours, 50 µL of an aqueous 1.25 M NaOH solution was added to the reaction vessel to maintain a high pH as the pH was found to

decrease over time. After 4 hours, the nanoparticles are washed twice with DI water via centrifugation. Note, polypropylene centrifuge tubes are used to prepare reagents and a Teflon beaker is used as the reaction vessel. Glass containers are completely avoided as glass can dissolve in basic solutions.

5.3.3 Scalable Synthesis for Ag-Pt Core-Shell Nanocubes

To perform a small scale version of this synthesis for Ag-Pt core-shell nanocubes, 1 mL of the purified Ag nanocubes are mixed with 2 mL of DI water containing 50 mg of PVP. The Pt precursor solution is prepared separately by dissolving 12 mg of K_2PtCl_4 (Sigma Aldrich, 99.99%) in 8 mL of DI water. The pH of this solution is adjusted to ~12 by adding 50 µL of a 1.25 M aqueous NaOH solution. The Pt precursor solution is allowed to sit for 10 minutes before addition to the reaction vessel. The reducing solution is prepared by adding 100 mg of ascorbic acid (Sigma Aldrich, reagent grade) to 3 mL of DI water. The pH of the reducing solution is increased by adding 600 µL of 1.25 M NaOH solution. The reducing solution is then immediately added to the mixture of Ag nanocubes under stirring followed by rapid addition of the Pt precursor solution. Every hour, 50 µL of 1.25 M NaOH are added to the reaction mixture to maintain a high pH. After 2 hours, the reaction mixture is transferred to a centrifuge tube, diluted to 45 mL with pH ~12 DI water, and centrifuged for 20 minutes at 10,000 rpm to separate the nanoparticles. The supernatant is discarded and the nanoparticles are re-dispersed in 5 mL of ~12 pH water. The nanoparticles are washed once more by diluting to 45 mL with ~12 pH water, centrifugated for 20 minutes at 10,000 rpm to separate the nanoparticles, and re-dispersed in 5 mL of ~12 pH water. Note, polypropylene centrifuge tubes are used to prepare reagents and a Teflon beaker is used as the reaction vessel. Glass containers are completely avoided as glass can dissolve in basic solutions.

To perform the 10 times scale up of this synthesis, 200 mg of PVP are mixed with 10 mL of the purified Ag nanocubes. The Pt precursor solution is prepared separately by dissolving 32 mg of K_2PtCl_4 in 5 mL of DI water. The pH of this solution is increased to ~12 by adding 50 μL of 1.25 M NaOH solution. The Pt precursor solution is allowed to sit for 10 minutes prior to addition to the reaction vessel. The reducing solution is prepared by dissolving 250 mg of ascorbic acid in 3.5 mL of DI water. The pH of the reducing solution is increased by adding 1.5 mL of 1.25 M NaOH. The reducing solution is then immediately added to the mixture of Ag nanocubes under stirring followed by rapid addition of the Pt precursor solution. Every hour, 100 μL of 1.25 M NaOH is added to the reaction mixture to maintain a high pH. After 2 hours, the reaction mixture is split into two centrifuge tubes, diluted to 45 mL with ~12 pH water, and centrifuged for 20 minutes at 10,000 rpm to separate the nanoparticles. The supernatant is discarded and one additional wash is performed as described above.

5.3.4 Characterization of Ag and Ag-Pt Nanocubes

Scanning transmission electron microscopy (STEM) and energy dispersive X-ray spectroscopy (EDS) are performed using a JEOL 3100 double CS-corrected TEM/STEM operated at an accelerating voltage of 300 kV. STEM samples are prepared by drop casting a solution of the nanoparticles onto 200 mesh carbon-on-copper grids. Elemental maps and line scans are taken using the Ag Lα and Pt M peaks in EDS.

UV-vis spectroscopy is performed using an Evolution 300 spectrophotometer. To compare the concentrations of nanoparticles produced in the scale up synthesis, 500 μL of the purified Ag-Pt nanocubes is diluted to 3 mL and analyzed using UV-vis spectroscopy.

Diffuse reflectance infrared Fourier transform spectroscopy (DRIFTS) is performed using a Nicolet is50 infrared spectrometer with a liquid nitrogen-cooled HgCdTe (MCT) detector

coupled with a Harrick high-temperature reactor chamber with a dome cape and KBr windows placed inside a Harrick Praying Mantis diffuse reflectance cell. The spectrometer and diffuse reflectance cell are continuously purged with N_2 gas. Data were collected by averaging 128 scans at a resolution of 4 cm^{-1}.

5.4 Approach for Ag-Pt Core-Shell Nanocubes

We first illustrate a shortcoming of a simple synthesis approach where pre-formed Ag nanocubes are used as seeds and a common Pt precursor (K_2PtCl_4) is reduced on the Ag nanocube seeds using a common mild reducing agent (ascorbic acid) at room temperature. If an aqueous solution of K_2PtCl_4 is added to an aqueous mixture of Ag nanocubes and ascorbic acid, atoms of Ag in the metal nanocubes will rapidly be oxidized through galvanic replacement with Pt resulting in the formation of hollow structures (Figure 5.1). This detrimental side reaction is a consequence of the difference in the reduction potentials of Pt and the reduction potential of Ag.[24,25] Since the reduction potential of Pt^{2+} is higher than the reduction potential of Ag, the replacement reaction is favorable.
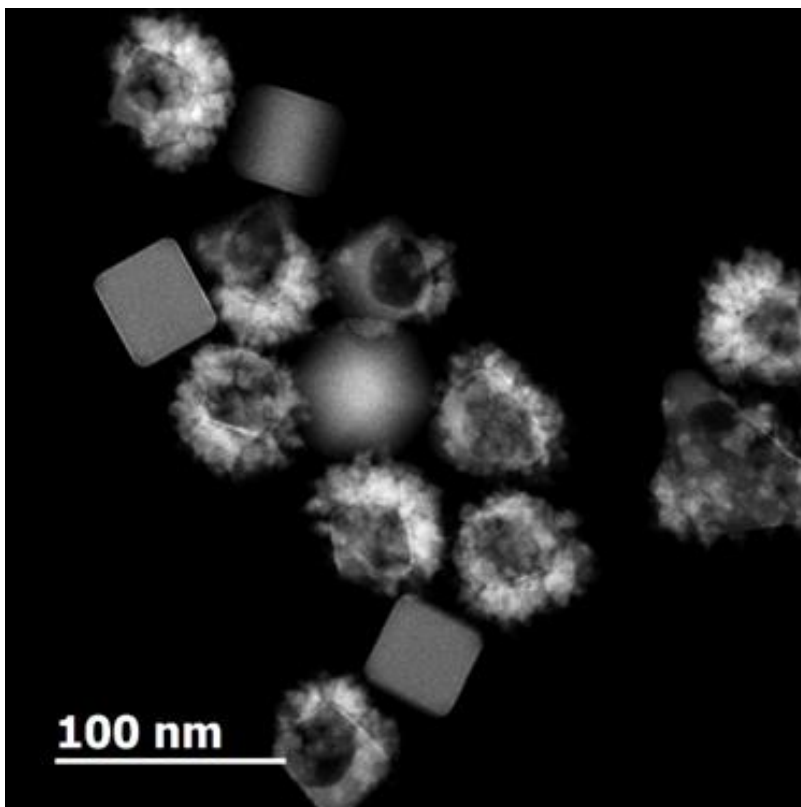
Figure 5.1 STEM image of Ag-Pt nanoparticles following galvanic replacement. Hollow Ag-Pt nanoparticles produced by galvanic replacement of Ag by Pt. The Ag is oxidized out of the nanoparticles and Pt is disorderly deposited around the resulting cages.

An approach for avoiding this detrimental side reaction which emerged in the literature over the last few years is to kinetically outcompete the galvanic replacement reaction with the reduction of the shell metal precursor by a strong reducing agent.[14,26] The concept is illustrated in Figure 5.2. To slow the galvanic replacement reaction, the concentration of the two reactants (Ag nanocubes and Pt^{2+} precursor) should be minimized. The concentration of Ag nanocube seeds can be minimized by using a small fraction of the Ag nanocube seeds and diluting them with water in the reaction vessel. To minimize the concentration of the Pt^{2+} precursor, we prepare a dilute solution of the precursor in water and slowly add the precursor dropwise to the reaction vessel over the course of several hours using a syringe pump. Prior to the dropwise addition of the Pt^{2+} precursor, a strong reducing agent is added to the solution which forces the rapid reduction of the Pt^{2+} onto the Ag nanocubes.
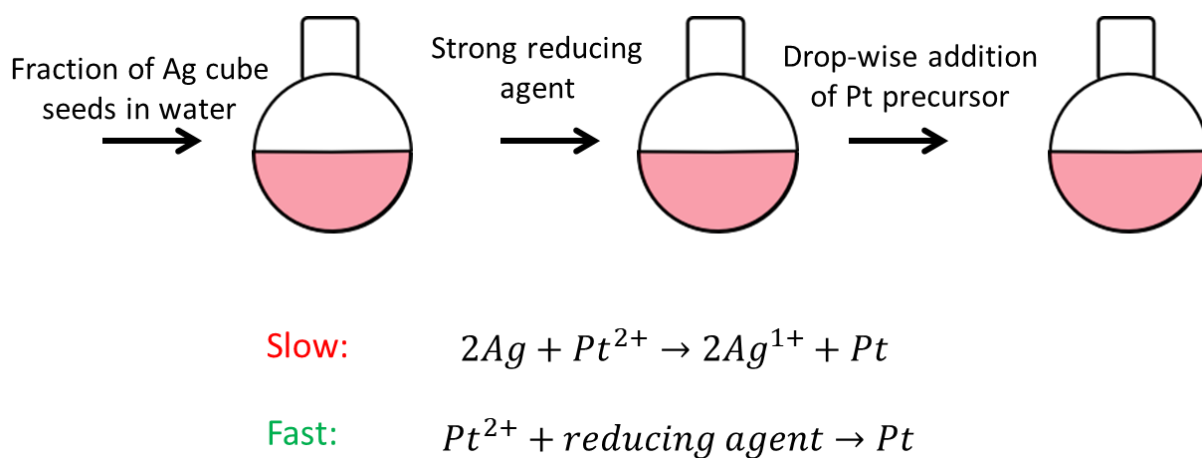
Figure 5.2 Depiction of Ag-Pt core-shell nanocube synthesis. Depiction of synthesis approach used to synthesize Ag-Pt core-shell nanocubes. The strategy is to slow down the galvanic replacement reaction and push the reduction of all Pt^{2+} entering the reaction vessel by the reducing agent. This is accomplished by lowering the concentration of reactants for the replacement reaction and using a strong reducing agent to drive the reduction reaction.

Geometry characterization studies in Figure 5.3 unambiguously show that the synthesis approach yields Ag nanocubes covered by a thin Pt shell. A bright-field transmission electron micrograph (TEM) of a representative Ag-Pt core-shell nanocube is shown in Figure 5.3a. The high resolution TEM image in Figure 5.3c (atomic resolution in Figure 5.3d) shows that the Pt shell thickness in these nanoparticles was approximately 6 atomic layers of Pt which corresponds to 1.2 ± 0.2 nm. A dark-field scanning transmission electron microscope (STEM) image of a core-shell nanoparticle is shown in Figure 5.3e. An energy-dispersive X-ray spectroscopy (EDS) elemental line scan across a single representative nanoparticle (Figure 5.3b) and the EDS elemental mapping of Ag and Pt in Figures 5.3f-h show that Pt atoms are covering the Ag nanocube (75 nm edge length).
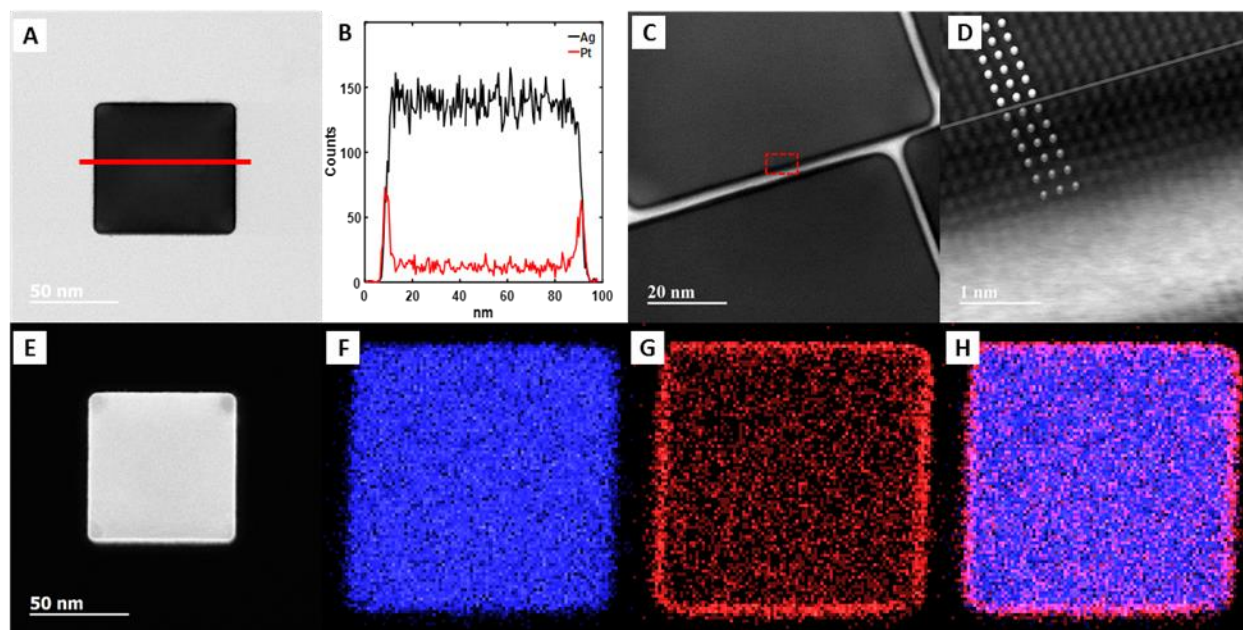
Figure 5.3 Characterization of Ag-Pt nanocubes from unscalable synthesis. (a) Bright-field TEM image of a single Ag nanocube coated with a thin layer of Pt. **(b)** EDS elemental line scan across the Ag-Pt core-shell nanocube demonstrating the elemental composition of the core and shell. **(c)** and **(d)**, High resolution and atomic-resolution bright-field TEM images. The thin Pt shell appears darker in contrast owing to the higher elemental weight of Pt. The Ag and Pt atoms are highlighted in **d** which clearly shows the boundary between the two materials. **(e-h)** Dark-field STEM image of a representative core-shell nanocube and EDS elemental maps of Ag **(f)**, Pt **(g)**, and overlay of the two **(h)** demonstrating the complete coverage of Ag by Pt.

Several dark-field STEM images of the Ag-Pt nanocubes are shown in Figure 5.4. These images show that the core-shell structures are synthesized in high yields with minor etching of Ag at the corners of some nanostructures. The etching at the corners is due to the higher chemical reactivity of low-coordinated Ag atoms at the tips of the nanocubes which are more susceptible to galvanic replacement. Figure 5.4 also shows high resolution images of the edges of three different Ag-Pt core-shell nanocubes. The boundary between the Pt atoms and Ag atoms can clearly be seen in these images. The thickness of the Pt shell can easily be varied by changing the reaction time of the synthesis. For example, we were able to synthesis Ag-Pt nanocubes with Pt shell thicknesses of 0.8 nm ± 0.2, 1.2 nm ± 0.2, and 1.6 nm ± 0.2 by using reaction times of 2 hours, 4 hours, and 8 hours respectively (Figure 5.4).

Although this approach can be used to synthesize Ag-Pt core-shell nanocubes with ultrathin shells, it only produces micrograms of material. In order to perform lab-scale catalytic experiments, we need to be able to produce at least milligrams of material. A crippling feature of this synthesis is that it relies on the careful control of reactant concentrations. Therefore, scaling up the synthesis by 100 times requires that the synthesis be performed in a 2 L reaction vessel to produce milligrams of material. The sheer size of such a synthesis for milligrams of materials is not only difficult to perform in lab but would also present hurdles in the washing and concentration of the nanoparticles.
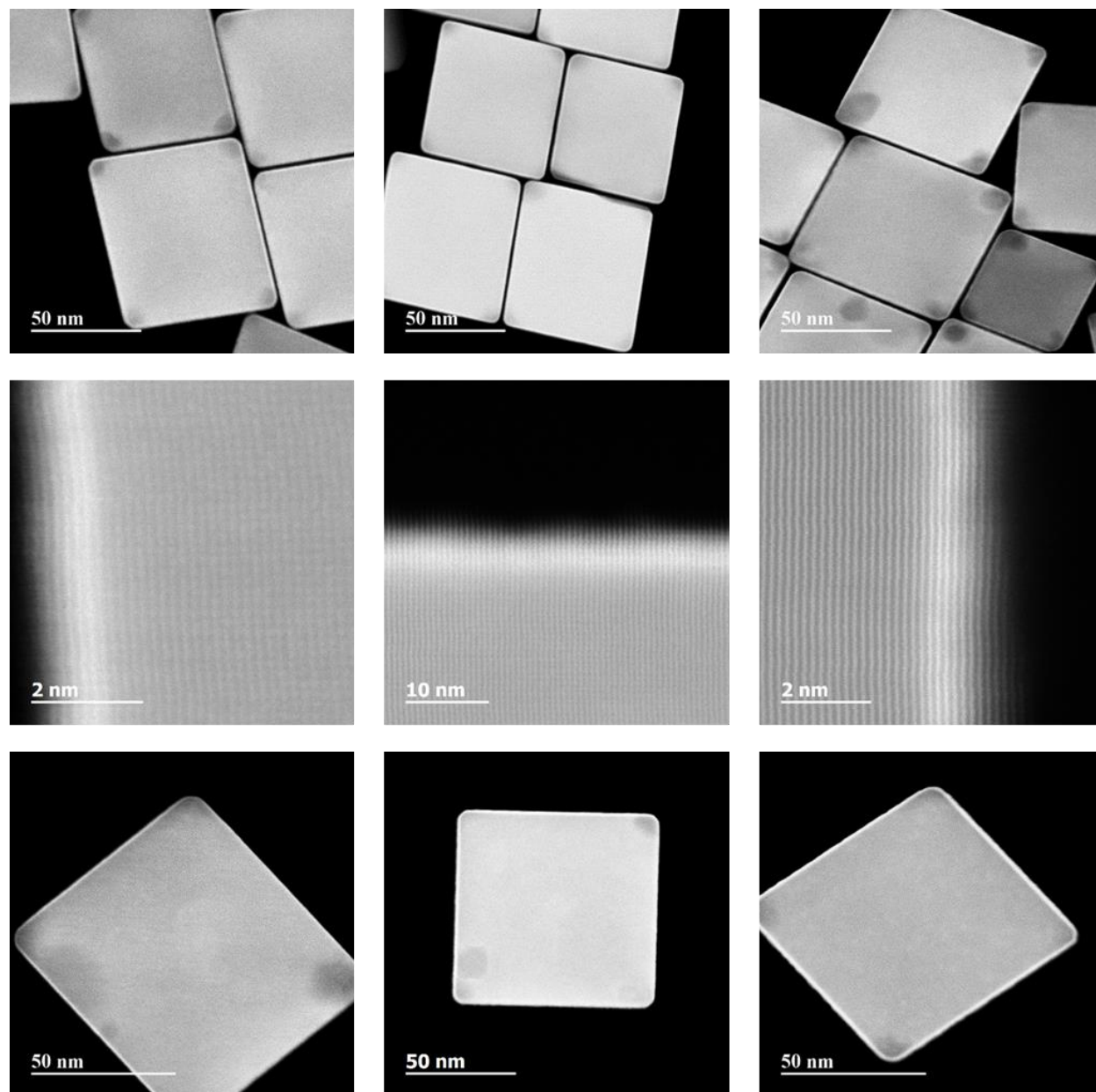
Figure 5.4 STEM images of Ag-Pt nanocubes. Additional STEM characterization of Ag-Pt core-shell nanocubes. (Top row) Dark field STEM images showing the high yield of core-shell nanostructures. (Middle row) High resolution images of the edge of Ag-Pt core-shell nanocubes showing the partitioning of Ag and Pt atoms in the nanostructures (Bottom row) STEM images demonstrating the ability to vary shell thickness from 0.8 nm (left), 1.2 nm (middle), and 1.6 nm (right).

5.5 Scalable Synthesis for Ag-Pt Core-Shell Nanocubes

To address the issue of scalability, we set out to develop a wholly new approach for depositing a thin layer of Pt onto Ag nanocubes. A major obstacle to doing this is the galvanic replacement of the Ag nanoparticles by Pt precursors. The strategy from literature that emerged over the last few years for navigating around this issue focused around kinetically outcompeting the galvanic replacement reaction. We consider a different approach. Instead of kinetically outrunning the reaction, we contemplate methods by which we can thermodynamically suppressing the reaction instead.

To understand how this can be done, we examine the galvanic replacement reaction in more detail. This detrimental side reaction is a consequence of the difference in the reduction potentials of the reacting species. The reaction is commonly portrayed as Ag metal reacting with Pt^{2+} to form Ag^+ and Pt metal. However, we are using K_2PtCl_4 as the shell metal precursor. This salt dissociates into $2K^+$ and $[PtCl_4]^{2-}$. If we now consider the galvanic replacement of Ag by this precursor, the reaction is written as $2Ag + [PtCl_4]^{2-} \rightarrow 2AgCl + Pt + 2Cl^-$. Since the reduction potential of $[PtCl_4]^{2-}$ is higher than the reduction potential of AgCl, the replacement reaction is thermodynamically favorable. To avoid triggering this reaction, we explored using a Pt metal complex with a lower reduction potential than $[PtCl_4]^{2-}$ thereby rendering the galvanic replacement reaction thermodynamically unfavorable.

5.5.1 Identifying a New Pt Precursor

To identify a Pt metal complex with the appropriate reduction potential, we considered a chemical modification of $[PtCl_4]^{2-}$ through ligand exchange of the Cl^- ligands. $[PtCl_4]^{2-}$ is a square planar d^8 metal complex with a Pt^{2+} metal center requiring two electrons for reduction to Pt metal. In the framework of crystal field theory, the splitting of d-orbitals of the Pt^{2+} metal center can be

changed by exchanging Cl⁻ ligands with other ligands thereby changing the energy of the $5d_{x2-y2}$ orbitals (Figure 5.5a).[27] For example, if the Cl⁻ ligands are exchanged with stronger field splitting ligands (such as OH⁻), then the energy level of the $5d_{x2-y2}$ orbital will increase thereby necessitating higher energy electrons to reduce Pt^{2+} to Pt metal (i.e. lowering the reduction potential of the complex), as depicted in Figure 5.5b.

To prepare a Pt metal precursor with lower reduction potential than $[PtCl_4]^{2-}$, we performed ligand exchange of a 4 mM aqueous solution of $[PtCl_4]^{2-}$ with OH⁻ by increasing the pH of the solution to ~12 through addition of a NaOH solution. The high concentration of OH⁻ in solution promotes ligand exchange of the Cl⁻ ligands of $[PtCl_4]^{2-}$ with OH⁻. UV-vis spectroscopy was used to characterize the ligand exchange. The data in Figure 5.5b show that the increase in the pH of the solution was accompanied by changes in the optical extinction by the metal complex suggesting that the electronic structure of the metal complex changed through chemical interactions with OH⁻ ions. The changes to the metal precursor were complete after 10 min.

To test whether this ligand exchange affected the reducibility of the Pt^{2+} metal complex, an experiment was performed in which two aqueous solutions of 4 mM K_2PtCl_4 were reduced with 0.06 M ascorbic acid. The reactions were monitored using UV-vis spectroscopy. In the control sample, the pH of the solution was not adjusted and data in Figure 5.5c show that the reduction of the Pt precursor began taking place within 30 minutes of introducing the reducing agent. In the other sample, the solution pH was adjusted to ~12, and the solution containing the reducing agent (also kept at pH 12) was added after 10 minutes. As discussed above, these conditions allowed the precursor to undergo the above-described ligand exchange before the reducing agent was added. In contrast to the control sample, data in Figure 5.5d show there was no reduction of the Pt

precursor for over 2 hours after addition of the reducing solution. This suggests that the reduction

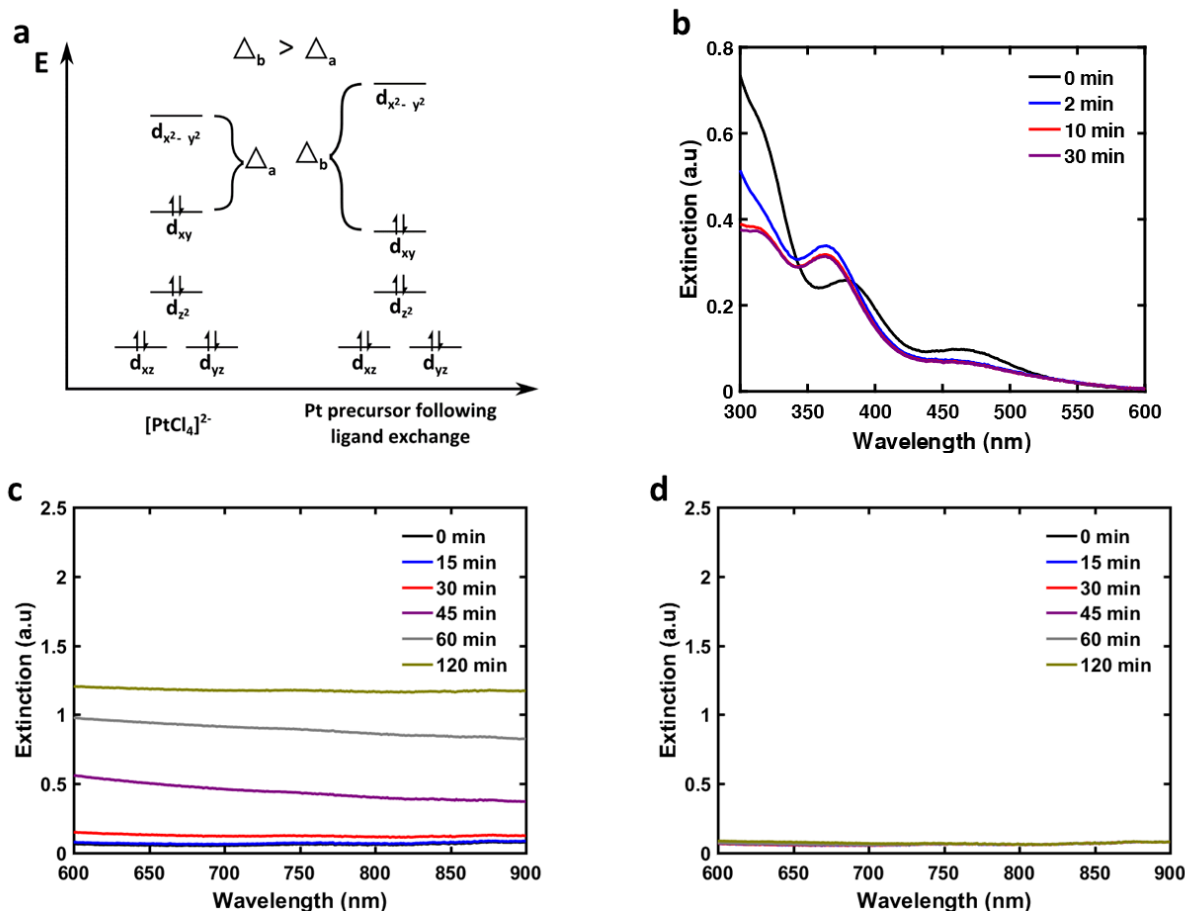potential of the Pt precursor is lowered following ligand exchange of Cl⁻ with OH⁻.

Figure 5.5 Chemical modification of Pt precursor. (**a**) Energy diagram sketch of d-splitting for [PtCl$_4$]$^{2-}$ metal complex and Pt precursor following ligand exchange with OH⁻. Hydroxide is a stronger field ligand than Cl⁻ resulting in a larger splitting between the orbitals. (**b**) UV-vis extinction of aqueous [PtCl$_4$]$^{2-}$ following addition of NaOH solution. (**c**) Characterizing reduction of [PtCl$_4$]$^{2-}$ by ascorbic acid. As the precursor is reduced to Pt metal, the solution turns black and optical extinction in the visible wavelength range increases. (**d**) Characterizing reduction of ligand-exchanged Pt^{2+} precursor. The visible optical extinction of the solution does not change over 2 hours.

5.5.2 Synthesis and Characterization of Ag-Pt Core-Shell Nanocubes

The chemically-modified Pt precursor was then used for the synthesis of Ag-Pt core-shell nanocubes. The synthesis was performed by mixing 1 mL of a solution containing Ag nanocube seeds (~0.7 mg/mL) with a solution of ascorbic acid and polyvinylpyrrolidone (PVP), a polymeric stabilizing agent. We note that we have also performed this synthesis with reducing agents other than ascorbic acid (see the supporting information document for associated discussion and data). The pH of the mixture was adjusted to ~12 with aqueous NaOH. The ligand-exchanged Pt^{2+} precursor was prepared as described above by increasing the pH of a 4 mM aqueous solution of K_2PtCl_4 to ~12 through addition of NaOH solution and allowing ligand exchange to occur for 10 minutes. The ligand-exchanged Pt^{2+} precursor solution was then added to the Ag nanocube mixture under stirring. This brought the final volume of the solution to 16 mL with a concentration of 2 mM ligand-exchanged Pt^{2+} precursor, 36 mM ascorbic acid, and 17 mM PVP at a pH of ~12. The mixture was allowed to react for 2 hours. It was found that the pH of the solution gradually decreased over time possibly due to the consumption of ascorbate anions (i.e. the reducing agent) over time. As ascorbate anions are consumed, ascorbic acid dissociation will increase thereby increasing the concentration of protons and lowering the pH. Because the chemical modification of the Pt^{2+} precursor is driven by a high concentration of OH^- (i.e. high pH), a decrease in pH causes the modified precursor to become unstable resulting in the galvanic replacement of the Ag nanocubes by Pt. To avoid this, 25 μL of a NaOH solution (1.25 M) was introduced to the reaction mixture every hour to maintain a high pH.

Scanning transmission electron microscopy (STEM) was used to characterize the Ag-Pt core-shell nanoparticles. Figure 5.6a shows a collection of Ag-Pt core-shell nanocubes demonstrating that the nanostructures were produced in high yields with some etching at the

corners of the nanocubes due to galvanic replacement of undercoordinated Ag atoms at the corners. A representative nanoparticle is shown in Figure 5.6b. An elemental line scan (Figure 5.6e) and elemental mapping (Figure 5.6f-h) performed using energy-dispersive X-ray spectroscopy (EDS) demonstrate that Pt atoms completely surround the cubic Ag core. The high resolution and atomic resolution images in Figure 5.6c and 5.6d show that the average thickness of the Pt shell was 1.0 ± 0.1 nm which corresponds to 5 atomic layers of epitaxially deposited Pt atoms. The thickness of the Pt shell could also be varied by changing the reaction time of the synthesis. For instance, a reaction time of 0.5 hour produces a Pt shell thickness of 0.6 ± 0.1 nm and a reaction time of 8 hours produces a 1.4 ± 0.1 nm thick shell of Pt. The slow, non-linear increase in shell thickness with reaction time suggests that the initial reduction of Pt^{2+} onto the surface of the Ag nanocubes is relatively fast compared to the subsequent reduction of Pt^{2+} onto Pt surface atoms. This suggests that the surface Ag atoms are quickly coated with a layer of Pt which is followed by a much slower reduction of Pt^{2+} onto Pt surface atoms resulting in the epitaxial growth of the Pt shell.
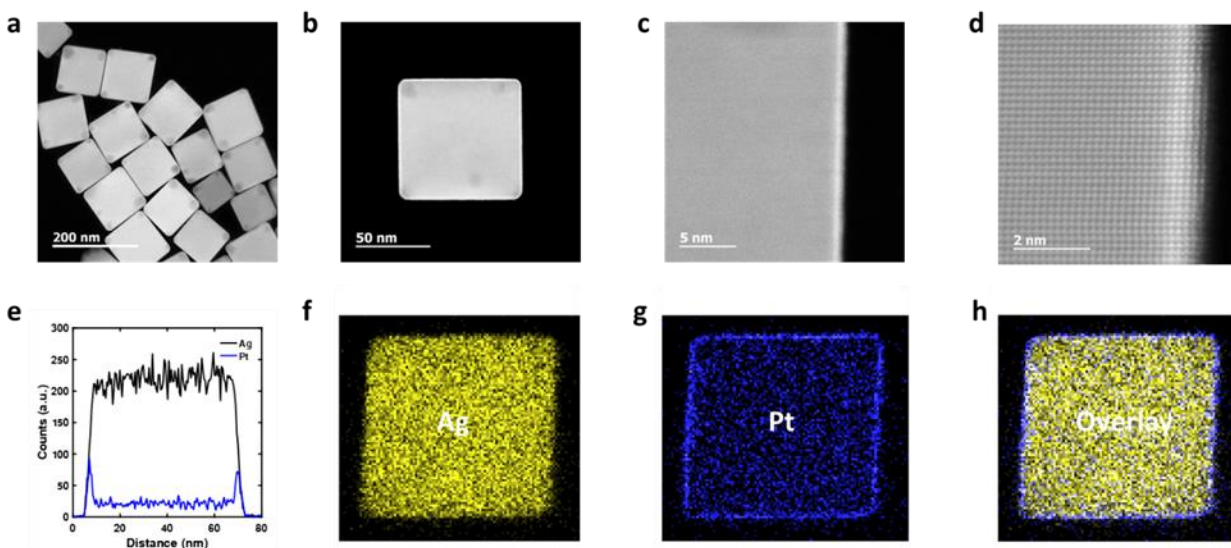
Figure 5.6 Characterization of Ag-Pt nanocubes from scalable synthesis. (a) STEM image of a collection of Ag-Pt core-shell nanocubes demonstrating high yield of core-shell structures, **(b)** a single Ag-Pt nanocube, **(c)** the edge of a single nanocube in which the ~1 nm Pt shell is clearly visible, and **(d)** atomic resolution image showing 5 atomic layers of Pt epitaxially deposited onto the Ag nanocube. **(e)** EDS elemental line scan across a representative Ag-Pt nanocube showing that the shell is made of Pt and the core of Ag. EDS elemental map of **(f)** Ag, **(g)** Pt, and **(h)** the overlay of the two.

5.5.3 Characterizing the Hybrid Optical and Surface Properties of Ag-Pt Nanocubes

The optical properties of the core-shell nanoparticles were characterized using UV-vis extinction spectroscopy (Figure 5.7a). The optical extinction of the Ag nanocube seeds displays multiple peaks associated with dipolar, quadripolar, and higher order plasmon resonances.[28] The data in Figure 5.7a show that when Pt is coated on the Ag nanocubes, the nanoparticles retain their plasmonic properties. The higher order plasmon resonance features are smeared and the main dipolar resonance peak is slightly broadened and red-shifted. The red-shift in the plasmon peak can be attributed to a slight increase in the size of the nanoparticles as it is well-known that larger plasmonic nanoparticles have a lower energy LSPR frequency.[29,30] The width of the peak is related to the decay rate of excited plasmons which increases when Pt is coated onto the Ag nanocubes due to an increase in absorption.[31–33]

The chemical properties of the Ag-Pt nanocube surface were characterized by measuring the vibrational energy of CO adsorbed on the surface using diffuse reflectance infrared Fourier transform spectroscopy (DRIFTS). The nanoparticles were deposited onto a Si chip, treated with air at 250°C for 3 hours, and reduced with pure H_2 at 200°C for 1 hour to clean the surface of the nanoparticles. A mixture of 10% CO in N_2 was then flowed across the nanoparticles at room temperature for 10 minutes to allow CO to adsorb to the surface of the Ag-Pt nanocubes. Excess CO was then purged from the system using pure N_2. Data in Figure 5.7b show a vibrational spectrum for adsorbed CO on Ag-Pt nanocubes. The vibrational frequency of the C-O bond when adsorbed on the surface of the Ag-Pt nanoparticles was measured to be at 2057 cm^{-1} which is characteristic of CO adsorbed on Pt surfaces. We note the vibrational energy of the C-O bond on spherical Pt nanoparticles (dominated by Pt(111) surface facet) is centered at 2060 cm^{-1}.[34] In contrast, the Ag-Pt nanocubes are dominated by the lower coordinated Pt(100) surface facet which

causes the vibrational frequency of CO to be slightly lower.[35] The combination of the optical data and DRIFTS data in Figure 5.7 demonstrate that the Ag-Pt core-shell nanoparticles effectively combine the plasmonic properties of the Ag nanocube core with the surface properties of the Pt shell.
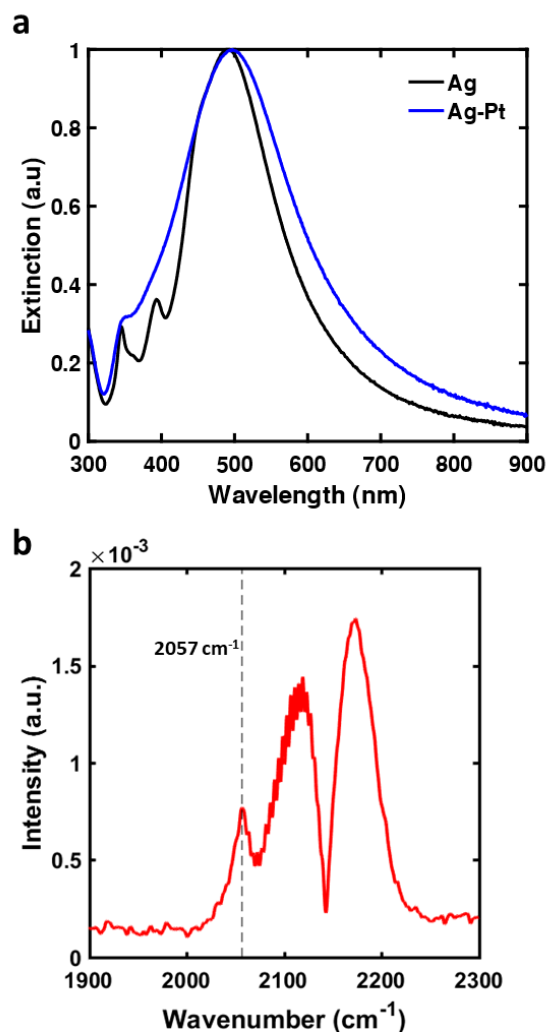
Figure 5.7 Characterizing hybrid properties of Ag-Pt nanocubes. **(a)** Normalized optical extinction spectra of Ag nanocube seeds and Ag-Pt nanocubes. **(b)** DRIFTS data for CO adsorption on the surface of the Ag-Pt nanocubes. The feature centered at 2057 cm^{-1} represents the vibrational frequency of the C-O bond when CO is adsorbed on the surface of the nanoparticles. The peaks at 2120 and 2170 cm^{-1} are for residual gas-phase CO.

5.5.4 Performing a 10 Times Scale Up

We have shown above that Ag-Pt core-shell nanocubes can be synthesized using a chemically-modified Pt^{2+} precursor prepared through ligand exchange with OH^-. The low reduction potential of the modified precursor prevents homogeneous nucleation of monometallic Pt nanoparticles and minimizes galvanic replacement of Ag by Pt. This characteristic makes the synthesis relatively insensitive to the concentration of Ag nanocube seeds or Pt^{2+} precursor allowing for the synthesis to be easily performed at large scales without a substantial increase in the reactor volume. To demonstrate the scalability of the synthesis, a 10 times scale up of the synthesis was performed following the procedure outlined above. After combining all reagents, the final volume of the reaction mixture was 20 mL which contained 10 mL of a solution of Ag nanocube seeds (~0.7 mg/mL), 4 mM of K_2PtCl_4, 70 mM ascorbic acid, and 90 mM of PVP at a pH of ~12. Despite the increase in concentration of the reducing agent, Pt^{2+} precursor, and 10 times increase in the number of Ag nanocube seeds, the epitaxial deposition of Pt onto the Ag nanocubes remained the most selective reaction pathway with no evidence of homogeneous nucleation of Pt nanoparticles and minimal galvanic replacement (Figure 5.8a). UV-vis spectroscopy was used to compare the concentration of the 10 times scale-up Ag-Pt product to the concentration of the small scale (~0.7 mg Ag nanocube seed) Ag-Pt product. Data in Figure 5.8b show that the maximum optical extinction for the scaled-up product was ~15 times higher than the maximum optical extinction for the regular scale product, clearly indicating that the scaled-up synthesis yielded at least a proportionally higher amount of the product Ag-Pt core-shell nanostructures.
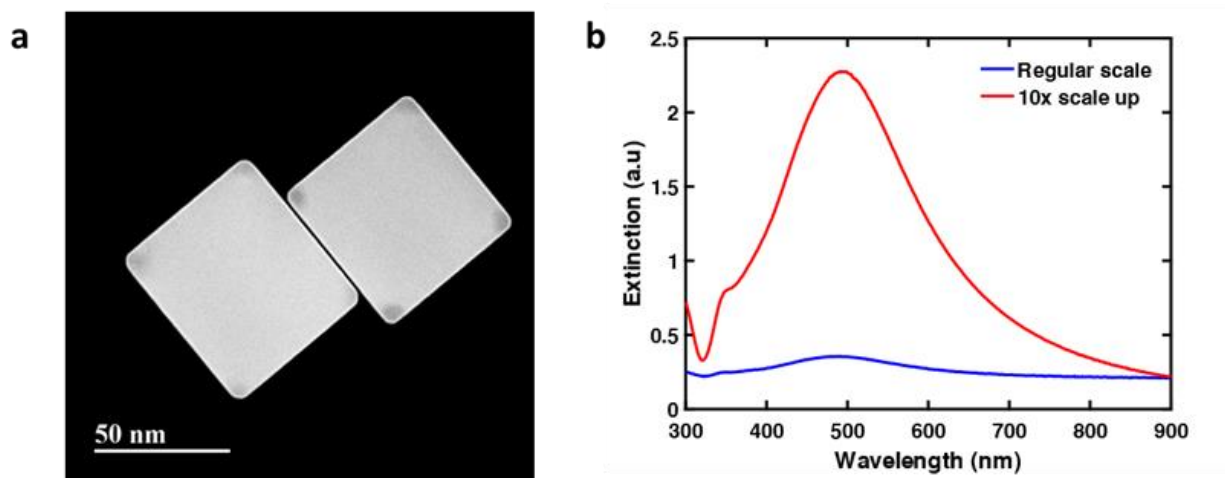
Figure 5.8 Ten times scale up of Ag-Pt nanocube synthesis. (a) STEM image of Ag-Pt nanocubes produced from 10 times scale up synthesis. **(b)** UV-vis extinction spectra of Ag-Pt nanocubes in water demonstrating the success of the 10 times scale synthesis

5.5.5 Use of Other Reducing Agents

To test whether it is possible to perform this synthesis with other reducing agents, we substituted ascorbic acid with the same concentration of glucose or ice-cold $NaBH_4$ as the reducing agent. When ice-cold $NaBH_4$ was used, the color of the reaction mixture slowly began to darken and fade. After 1 hour, the mixture was completely clear. This behavior is characteristic of galvanic replacement reactions in which the Ag nanocube core is oxidized by the Pt precursor.[25] The $NaBH_4$ likely caused the chemically-modified Pt^{2+} precursor to become unstable resulting in the galvanic replacement of Ag by Pt.

In contrast, the synthesis was completely successful when using glucose in place of ascorbic acid as the reducing agent. A STEM image of a representative nanoparticle synthesized using glucose as the reducing agent is shown in Figure 5.9. Because glucose is a weaker reducing agent, the synthesis must be performed for a longer period of time. The resulting Ag-Pt core-shell nanocubes tend to display less etching even at the corners of the nanostructures. When ascorbic acid is used as the reducing agent, the consumption of ascorbate anions pushes the equilibrium of the acid dissociation reaction to produce more H^+ thereby gradually increasing the acidity of the solution. Given that the galvanic replacement reaction is more likely to occur under acidic conditions, base is constantly added to the reaction vessel to compensate for this decrease in the solution pH. By using glucose in place of ascorbic acid, this issue is avoided all together.
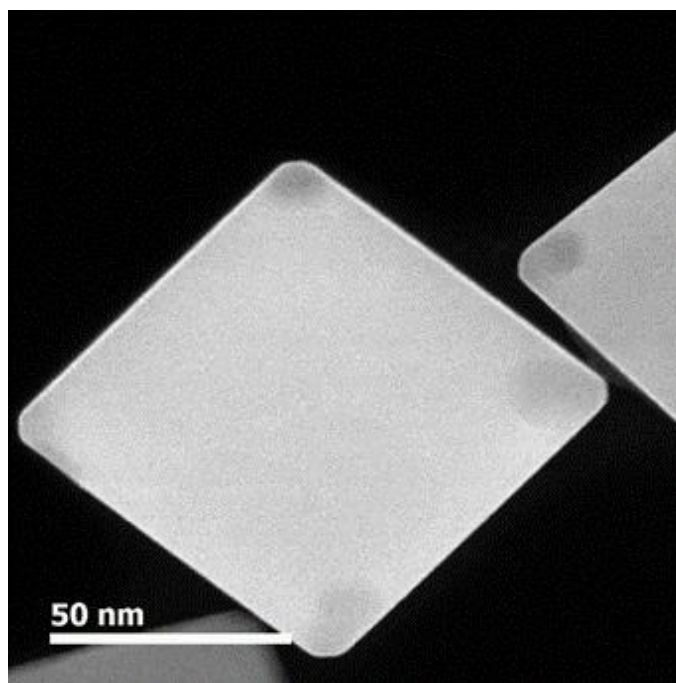
Figure 5.9 STEM image of Ag-Pt nanocube synthesized using glucose. Glucose synthesized Ag-Pt nanocubes appear to undergo less galvanic replacement even at the corners.

5.5.6 Use of Other Shell Metal Precursors

The success of this synthesis approach for coating a few atomic layers of Pt onto Ag nanocubes motivated us to investigate whether this synthesis could be used to coat other metals onto Ag nanocubes. To test whether this synthesis procedure could be used to coat Ag nanocubes with other metals, we performed the synthesis using a Pd (K_2PdCl_4) or Au ($HAuCl_4$) precursor in place of Pt (K_2PtCl_4) with all other reaction conditions constant. Addition of the Au precursor to the reaction mixture containing the Ag nanocubes resulted in an immediate change in the color of the reaction mixture. The mixture was allowed to react for 1 hour followed by washing via centrifugation. The supernatant from centrifugation was a bright red color characteristic of monometallic Au nanoparticles.[36,37] In addition, STEM characterization of the nanoparticles showed that nearly all of the Ag nanocubes underwent galvanic replacement with Au (Figure 5.10). These data suggest that the reduction potential of the Au precursor was too high causing the Au precursor to either quickly reduce to monometallic Au nanoparticles or galvanically replace the Ag nanocubes.
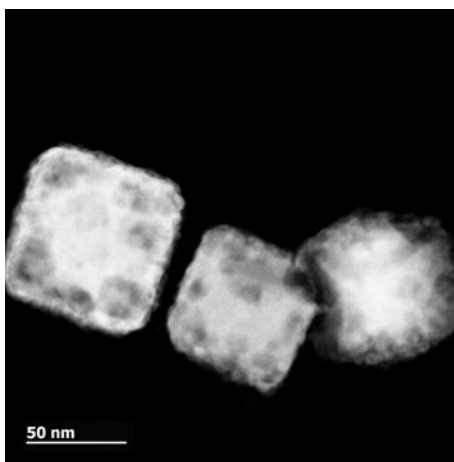

50 nm

Figure 5.10 STEM image of nanocubes produced from Au precursor. The resulting nanoparticles are largely either pure Au nanoparticles galvanically-replaced Ag.

In the case of the Pd precursor, the synthesis proceeded similarly to the Ag-Pt core-shell nanocube synthesis. The mixture was allowed to react for 1 hour and washed via centrifugation. At this point, there were some solid particulates that could not be dispersed in solution (possibly an insoluble Pd salt). STEM characterization of these nanoparticles showed that most of the Ag nanocubes remained intact with minimal galvanic replacement. Because Pd and Ag are very close in atomic weight, it is difficult to distinguish the two materials based on contrast in STEM images (Figure 5.11). An EDS spectra of the edge of a few nanocubes showed the presence of Pd near the surface of the nanoparticles. These data suggest that this approach (i.e. chemical modification of the Pd precursor with OH⁻ and reduction with ascorbic acid) could potentially be used to develop a scalable synthesis for coating Pd onto Ag nanocubes.

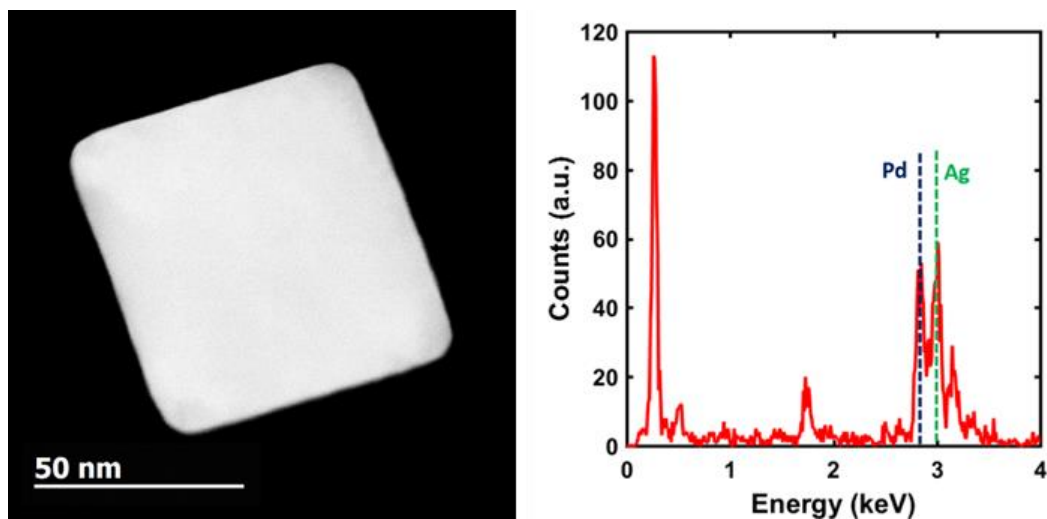

Figure 5.11 STEM image and EDS of Ag-Pd nanocubes. STEM image of a representative nanocube after performing synthesis with Pd precursor. A EDS spectrum collected at the edge of the nanocube displayed signals for both Ag and Pd.

5.6 Conclusions

We have developed a scalable synthesis approach for depositing a thin layer of Pt onto Ag nanocubes. This was accomplished using a synthesis in which the Pt^{2+} precursor was chemically modified through ligand exchange to decrease the precursor reduction potential. The low reduction potential of the modified precursor minimized undesired side reactions such as homogeneous nucleation of Pt nanoparticles and galvanic replacement. This feature of the synthesis makes it relatively insensitive to the concentration of the chemical reagents allowing for the synthesis to be easily scaled. As a demonstration of the scalability of the synthesis, we performed a 10 times scale-up without a substantial increase in the reaction vessel volume, using double the concentration of chemical reagents, and 10 times the amount of Ag nanocube seeds. By performing spectroscopic experiments, we showed that these Ag-Pt core-shell nanocubes display the hybrid optical properties of Ag which expressing the surface chemical properties of Pt. Our next aim is to design experiments aimed to shed light on the influence of the Pt shell on the flow of energy in these hybrid plasmonic materials.

5.7 References

1. Ghosh Chaudhuri, R. & Paria, S. Core/Shell Nanoparticles: Classes, Properties, Synthesis Mechanisms, Characterization, and Applications. *Chem. Rev.* **112,** 2373–2433 (2012).

2. Mitsudome, T. *et al.* Design of Core-Pd/Shell-Ag Nanocomposite Catalyst for Selective Semihydrogenation of Alkynes. *ACS Catal.* 666–670 (2015). doi:10.1021/acscatal.5b02518

3. Amram, D. & Rabkin, E. Core(Fe)–Shell(Au) Nanoparticles Obtained from Thin Fe/Au Bilayers Employing Surface Segregation. *ACS Nano* **8,** 10687–10693 (2014).

4. Niu, Z. *et al.* Ultrathin Epitaxial Cu@Au Core–Shell Nanowires for Stable Transparent Conductors. *J. Am. Chem. Soc.* **139,** 7348–7354 (2017).

5. Cleve, T. V., Moniri, S., Belok, G., More, K. L. & Linic, S. Nanoscale Engineering of Efficient Oxygen Reduction Electrocatalysts by Tailoring the Local Chemical Environment of Pt Surface Sites. *ACS Catal.* **7,** 17–24 (2017).

6. Xin, H., Holewinski, A. & Linic, S. Predictive Structure–Reactivity Models for Rapid Screening of Pt-Based Multimetallic Electrocatalysts for the Oxygen Reduction Reaction. *ACS Catal.* **2,** 12–16 (2012).

7. Schweitzer, N., Xin, H., Nikolla, E., Miller, J. T. & Linic, S. Establishing Relationships Between the Geometric Structure and Chemical Reactivity of Alloy Catalysts Based on Their Measured Electronic Structure. *Top Catal* **53,** 348–356 (2010).

8. Holewinski, A., Idrobo, J.-C. & Linic, S. High-performance Ag–Co alloy catalysts for electrochemical oxygen reduction. *Nat Chem* **6,** 828–834 (2014).

9. Huang, X., El-Sayed, I. H., Qian, W. & El-Sayed, M. A. Cancer Cell Imaging and Photothermal Therapy in the Near-Infrared Region by Using Gold Nanorods. *J. Am. Chem. Soc.* **128,** 2115–2120 (2006).

10. Stiles, P. L., Dieringer, J. A., Shah, N. C. & Duyne, R. P. V. Surface-Enhanced Raman Spectroscopy. *Annual Review of Analytical Chemistry* **1,** 601–626 (2008).

11. Adleman, J. R., Boyd, D. A., Goodwin, D. G. & Psaltis, D. Heterogenous Catalysis Mediated by Plasmon Heating. *Nano Lett.* **9,** 4417–4423 (2009).

12. Brongersma, M. L., Halas, N. J. & Nordlander, P. Plasmon-induced hot carrier science and technology. *Nat Nano* **10,** 25–34 (2015).

13. Park, J. *et al.* Atomic Layer-by-Layer Deposition of Platinum on Palladium Octahedra for Enhanced Catalysts toward the Oxygen Reduction Reaction. *ACS Nano* **9,** 2635–2647 (2015).

14. Yang, Y., Liu, J., Fu, Z.-W. & Qin, D. Galvanic Replacement-Free Deposition of Au on Ag for Core–Shell Nanocubes with Enhanced Chemical Stability and SERS Activity. *J. Am. Chem. Soc.* **136,** 8153–8156 (2014).

15. Sun, X., Yang, Y., Zhang, Z. & Qin, D. Mechanistic Roles of Hydroxide in Controlling the Deposition of Gold on Colloidal Silver Nanocrystals. *Chem. Mater.* **29,** 4014–4021 (2017).

16. Zhang, Y. *et al.* Observing the Overgrowth of a Second Metal on Silver Cubic Seeds in Solution by Surface-Enhanced Raman Scattering. *ACS Nano* **11,** 5080–5086 (2017).

17. Xia, Y., Gilroy, K. D., Peng, H.-C. & Xia, X. Seed-Mediated Growth of Colloidal Metal Nanocrystals. *Angewandte Chemie* **56,** 60–95 (2017).

18. Gao, C. *et al.* Highly Stable Silver Nanoplates for Surface Plasmon Resonance Biosensing. *Angewandte Chemie* **51,** 5629–5633 (2012).

19. Li, J., Liu, J., Yang, Y. & Qin, D. Bifunctional Ag@Pd-Ag Nanocubes for Highly Sensitive Monitoring of Catalytic Reactions by Surface-Enhanced Raman Spectroscopy. *J. Am. Chem. Soc.* **137,** 7039–7042 (2015).

20. Cobley, C. M. & Xia, Y. Engineering the properties of metal nanostructures via galvanic replacement reactions. *Materials Science and Engineering: R: Reports* **70,** 44–62 (2010).

21. Aslam, U. & Linic, S. Kinetic Trapping of Immiscible Metal Atoms into Bimetallic Nanoparticles through Plasmonic Visible Light-Mediated Reduction of a Bimetallic Oxide Precursor: Case Study of Ag–Pt Nanoparticle Synthesis. *Chem. Mater.* **28,** 8289–8295 (2016).

22. Sun, Y. & Xia, Y. Shape-Controlled Synthesis of Gold and Silver Nanoparticles. *Science* **298,** 2176–2179 (2002).

23. Christopher, P. & Linic, S. Shape- and Size-Specific Chemistry of Ag Nanostructures in Catalytic Ethylene Epoxidation. *ChemCatChem* **2,** 78–83 (2010).

24. Xia, X., Wang, Y., Ruditskiy, A. & Xia, Y. 25th Anniversary Article: Galvanic Replacement: A Simple and Versatile Route to Hollow Nanostructures with Tunable and Well-Controlled Properties. *Adv. Mater.* **25,** 6313–6333 (2013).

25. Chen, J. *et al.* Optical Properties of Pd−Ag and Pt−Ag Nanoboxes Synthesized via Galvanic Replacement Reactions. *Nano Lett.* **5,** 2058–2062 (2005).

26. Xie, S. *et al.* Atomic Layer-by-Layer Deposition of Pt on Pd Nanocubes for Catalysts with Enhanced Activity and Durability toward Oxygen Reduction. *Nano Lett.* **14,** 3570–3576 (2014).

27. Atkins, P. *Shriver and Atkins' Inorganic Chemistry*. (OUP Oxford, 2010).

28. Near, R., Hayden, S. & El-Sayed, M. Extinction vs Absorption: Which Is the Indicator of Plasmonic Field Strength for Silver Nanocubes? *J. Phys. Chem. C* **116,** 23019–23026 (2012).

29. Link, S. & El-Sayed, M. A. Size and Temperature Dependence of the Plasmon Absorption of Colloidal Gold Nanoparticles. *J. Phys. Chem. B* **103,** 4212–4217 (1999).

30. Kreibig, U. & Vollmer, M. *Optical Properties of Metal Clusters*. (Springer Science & Business Media, 2013).

31. Maier, S. A. *Plasmonics: Fundamentals and Applications*. (Springer Science & Business Media, 2007).

32. Bosbach, J., Hendrich, C., Stietz, F., Vartanyan, T. & Träger, F. Ultrafast Dephasing of Surface Plasmon Excitation in Silver Nanoparticles: Influence of Particle Size, Shape, and Chemical Surrounding. *Phys. Rev. Lett.* **89,** 257404 (2002).

33. Kreibig, U. Interface-induced dephasing of Mie plasmon polaritons. *Appl. Phys. B* **93,** 79–89 (2008).

34. Alayoglu, S., Nilekar, A. U., Mavrikakis, M. & Eichhorn, B. Ru–Pt core–shell nanoparticles for preferential oxidation of carbon monoxide in hydrogen. *Nat Mater* **7,** 333–338 (2008).

35. Kale, M. J. & Christopher, P. Utilizing Quantitative in Situ FTIR Spectroscopy To Identify Well-Coordinated Pt Atoms as the Active Site for CO Oxidation on Al2O3-Supported Pt Catalysts. *ACS Catal.* **6,** 5599–5609 (2016).

36. El-Sayed, M. A. Some Interesting Properties of Metals Confined in Time and Nanometer Space of Different Shapes. *Acc. Chem. Res.* **34,** 257–264 (2001).

37. Link, S. & El-Sayed, M. A. Spectral Properties and Relaxation Dynamics of Surface Plasmon Electronic Oscillations in Gold and Silver Nanodots and Nanorods. *J. Phys. Chem. B* **103,** 8410–8426 (1999).

Chapter 6 Ascertaining the Effects of Catalytic Metals on the Flow of Energy in Hybrid Catalytic-Plasmonic Nanoparticles

6.1 Summary

In this chapter, we design optical spectroscopy experiments to uncover the effects of catalytic metals on the energy flow in multicomponent photoexcited plasmonic materials. We use our well-defined Ag-Pt core-shell nanocubes as the ideal model system for performing these studies. By decomposing the optical extinction of these materials into its constituent absorption and scattering components, we show that coating a thin layer of Pt onto Ag nanocubes drastically alters the energy dissipation pathway from LSPR excitation towards absorption. We use electrodynamic simulations to spatially resolve the flow of energy in these systems showing that most of the absorption in Ag-Pt nanocubes occurs in the thin 1 nm shell of Pt. We conclude by presenting a tangible physical framework for explaining this dramatic re-routing of energy flow in hybrid plasmonic materials.

6.2 Introduction

We conceptualized the design of a hybrid plasmonic metal nanostructure that can efficiently harvest electromagnetic energy and then direct this energy towards a catalytic site on the plasmonic nanostructure where a chemical reaction can efficiently takes place. We postulated that a hybrid nanostructure that would meet the critical requirements of such a system should

contain a core plasmonic nanoparticle (a metal with low imaginary dielectric function at the LSPR (visible light) frequencies) surrounded by a very thin shell of a more chemically active material (catalytic surface sites), characterized by significantly larger imaginary dielectric function at the LSPR frequency. A material with these dielectric properties has two desired physical features: (i) due to the presence of a large plasmonic core, it can concentrate electromagnetic energy in the LSPR modes, and (ii) the energy stored in the LSPR modes can be selectively dissipated by forming energetic charge carriers (energetic e-h pairs) in the thin shell of the metal with the large imaginary dielectric function. We note that the larger imaginary dielectric function implies that the rate of energy dissipation (i.e., the decay of LSPR modes) through the formation of energetic charge carriers is larger compared to the material with a lower imaginary dielectric function.[1] We hypothesized that this hybrid nanostructure design would allow for a strong concentration of electromagnetic energy and its preferential dissipation through the surface atoms that are performing the chemical transformation.[2]

In chapter 5, we showed that we are able to synthesize such hybrid nanostructures by developing a synthetic approach that allows us to completely surround Ag nanocube cores (~ 75 nm in length) with thin Pt shells (~ 1 nm thickness).[3] Herein, we perform experimental and theoretical studies to follow the flow of energy in these hybrid materials. We aim to understand the effects of the Pt shell on the collection and dissipation of light energy by the plasmonic Ag core and uncover underlying physical mechanisms by which energy could be channeled into the thin Pt shell.

6.3 Methods

6.3.1 Extinction, Absorption, and Scattering Measurements

Ag-Pt core-shell nanoparticles for optical measurements were all synthesized from the same sample of Ag seed nanoparticles. Samples for optical measurements were prepared by diluting samples of Ag and Ag-Pt nanocubes in 3 mL of DI water in cuvettes. These samples were prepared to give roughly the same fractional extinction. A sample of just DI water was also prepared, and any contributions from the solvent were subtracted in all measurements. Extinction measurements were performed using a UV-vis spectrophotometer. The instrument passes monochromated light through the sample and measures the fraction of light that is transmitted and the extinction fraction can simply be calculated as

$$Extinction\ fraction = 1 - (transmission\ fraction)$$

The extinction fraction is the sum of the absorption fraction and scattering fraction. To decouple absorption from scattering, we use an optical integrating sphere combined with a monochromatic visible light source and photodiode detector. The optical integrating sphere is coated with a highly reflective coating which allows for the collection of scattered and transmitted light. The absorption fraction can be calculated from this data as

$$Absorption\ fraction = 1 - (transmission + scattering\ fraction)$$

Lastly, the scattering fraction can be calculated as

$$Scattering\ fraction = extinction\ fraction - (absorption\ fraction)$$

6.3.2 COMSOL Finite Element Method (FEM) Model Set-up

The extinction, absorption and scattering efficiencies, as well as the absorption ratios in the particle cores vs the particle shells were calculated using COMSOL Multiphysics finite-element based software. We utilized the 'Wave optics' module to calculate the scattered field resulting from a plane wave incident on a model 3-D nanoparticle. The plane wave was defined as: $E = E_0 e^{-ikx}$ and was polarized in the z-direction. Core-shell nanocubes with a 75 nm core edge length and

a 1.2 nm shell were defined and the free space wavelength range from 300 nm to 900 nm was simulated. The corners of the nanocubes in the simulations were smoothed to reflect the particle geometry observed in TEM characterization. Three different particles were simulated: pure Ag, pure Pt and Ag-Pt core-shell particles. Pure Ag and pure Pt were simulated by defining both the core and the shell of the particles as either Ag or Pt respectively. The optical data for Ag and Pt were taken from COMSOL's Optical Materials database (Rakic et. al)[4] and a region of air was defined around the particle by setting the real part of the dielectric function equal to 1. The width of the region of air around the particle was equal to half the wavelength of the incident plane wave and a perfectly matched layer (PML) was constructed to act as an absorber of the scattered field. Specific calculations are discussed in the following sections.

6.3.3 Simulation Extinction, Absorption, and Scattering Calculations

The absorption cross section as a function of wavelength was calculated by integrating the resistive heating losses over the volume of the nanoparticles. The scattering cross section as a function of wavelength was calculated by integrating the dot product of the scattered intensity vector and the normal vector pointing outwards from the particle surface across the entire particle surface. The extinction cross section was calculated by summing the absorption and scattering cross sections. The cross sections were then converted into efficiencies by dividing by the geometric cross section. The absorption in the particle core vs. the particle shell were calculated by integrating the resistive heating losses over volume of the core and the shell respectively.

6.3.4 Calculations of Shell-to-Core Absorption Ratios

We calculated the ratio of energy dissipation in the shell to the energy dissipation in the core from our optical simulations by integrating the total rate of absorption in the core and the shell with respect to photon energy and dividing by the respective volumes of the core and shell. We

estimated this shell-to-core energy dissipation ratio using our experimental integrating sphere data as well. This was done using the absorption data for Ag-Pt core-shell nanocubes with varying shell thickness. Assuming that the increase in absorption with increasing shell thickness was due only to the additional layers of Pt, we calculated an absorption per nm for the Pt shell. Using this, we calculated Pt shell absorption for a 1.2 nm thick shell. This shell absorption was subtracted from the total experimental absorption for Ag-Pt core-shell nanoparticles with 1.2 nm thick shells to give us the approximate absorption in the Ag core. Integrating the Pt shell and Ag core absorption with respect to energy and dividing by the respective volumes of the shell and core provides a total energy absorption in the shell and core per volume.

6.4 Experimental Study of Plasmon Decay Pathways in Ag and Ag-Pt Nanocubes

We analyzed the optical properties of the hybrid Ag-Pt nanostructures by measuring their extinction, absorption and scattering characteristics and comparing them to the optical behavior of Ag nanocubes of identical size and shape. Data in Figure 6.1a show that the introduction of the thin Pt shell on the Ag core only slightly affects the optical extinction of the nanostructures. The extinction peak due to the excitation of LSPR is clearly preserved. Small shifts in the position and width of the LSPR peak compared to pure Ag nanocubes are due to the Pt-induced changes in the dielectric environment from the presence of the Pt shell.[5,6] To determine whether the thin Pt shells themselves contribute to the optical extinction, acid leeching was used to remove Ag from the cores of the Ag-Pt nanoparticles in a representative sample, leaving behind thin-shelled Pt cages (Figure 6.1b).[7] Optical characterization of these cages showed that the Pt shell does not display any optical extinction in the visible range (Figure 6.1c).
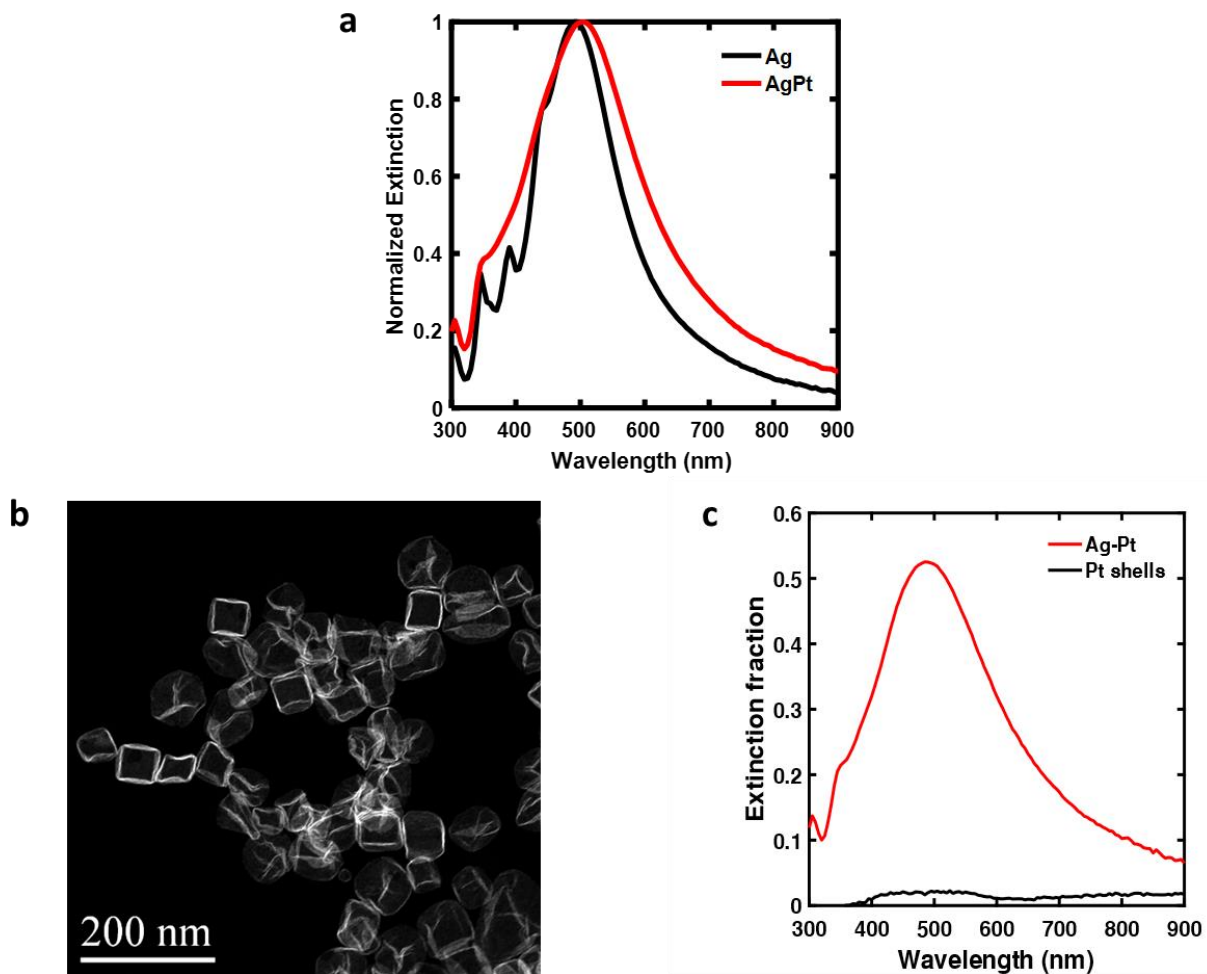
Figure 6.1 Characterizing optical properties of Ag-Pt nanocubes. (a) Normalized UV-vis optical extinction spectra for Ag and Ag-Pt nanocubes. The data show that Ag retains its plasmonic properties when coated with a thin layer of Pt. **(b)** STEM image of Pt boxes produced by leeching the core of Ag-Pt nanocubes using acid. **(c)** Optical extinction fraction for Ag-Pt nanocubes before and after leeching of the Ag core. The data show that the Pt shells do not contribute to the optical extinction of the Ag-Pt nanocubes.

Furthermore, we used an integrating optical sphere to measure the absorption and scattering of the pure Ag nanocubes and the Ag-Pt core-shell nanocubes. Data in Figure 6.2a and 6.2b show that the introduction of even a very thin Pt shell fundamentally changes the dominant channel for plasmon decay. Data in Figure 6.2a show that photon scattering is the dominant pathway for plasmon decay in pure Ag nanocubes which is consistent with previous measurements for Ag nanoparticles of this size.[8–10] Data in Figure 6.2b show that by introducing a thin Pt shell in our design, photon absorption (formation of energetic e-h pairs) becomes a critical plasmon decay pathway. Based on these experimental data, we hypothesized that the introduction of Pt introduces a faster plasmon decay channel through the Pt shell and that a large fraction of the electromagnetic energy concentrated in the nanostructure is dissipated through the thin Pt shell via the formation of energetic charge carriers (e-h pairs).

To build more evidence for this, we synthesized Ag-Pt core-shell nanocubes of varying shell thickness (0.8, 1.2, and 1.6 nm) and performed optical extinction and integrating sphere experiments to characterize the optical properties of these materials (Figures 6.2 c-e). These data show that as the thickness of the Pt shell increases, a larger fraction of the optical extinction comes from absorption. These data strongly suggest that energy collected by Ag is being directly dissipated in Pt.
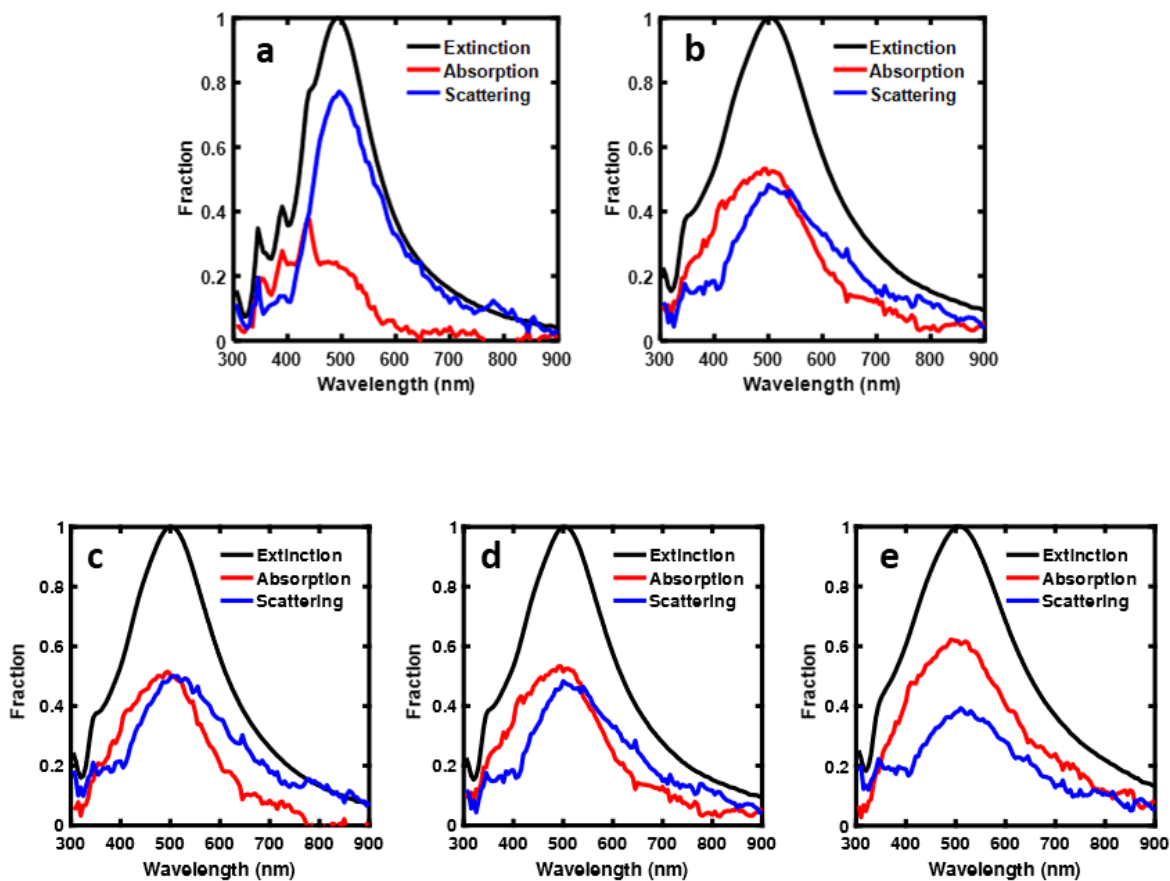
Figure 6.2 Decomposition of Ag-Pt optical extinction. (**a**) Measured fractional Ag nanocubes absorption and scattering. (**b**) Measured fractional Ag-Pt nanocubes absorption and scattering. (**c**) Measured fractional absorption and scattering for Ag-Pt nanocubes with 0.8 nm shell thickness. (**d**) Measured fractional absorption and scattering for Ag-Pt nanocubes with 1.2 nm shell thickness. (**e**) Measured fractional absorption and scattering for Ag-Pt nanocubes with 1.6 nm shell thickness.

6.5 Theoretical Study of Plasmon Decay Pathways in Ag and Ag-Pt Nanocubes

To further shed light on the optical behavior of these systems, we performed electro-dynamic finite element method (FEM) simulations. The model system used in our FEM simulations is identical to the nanoparticle geometry measured in the TEM studies. We first calculated the extinction efficiency (ratio of extinction cross section to geometric cross section) for the pure Ag, pure Pt, and Ag-Pt core-shell nanoparticles. Figure 6.3 shows the simulated extinction, absorption and scattering efficiencies for the three systems. The LSPR peak for the monometallic Ag particle is around 475 nm and plasmon decay is dominated by radiative scattering. This agrees very well with the experimental optical data for Ag nanoparticles presented in the manuscript, with the experimental red-shift due to the higher dielectric environment of water (used in experiments) compared to air (used in simulations). The data for monometallic Pt shows a much lower extinction efficiency than for Ag. This result is expected given that Pt is not a plasmonic metal.[11–14] The Ag-Pt particle shows a distinct LSPR peak at similar wavelengths to the pure Ag nanoparticle. The LSPR peak is also broadened compared to the Ag nanoparticle. These changes to the optical extinction of Ag nanoparticles coated with a thin layer of Pt are consistent with the changes observed experimentally. The extinction efficiency is slightly lower for the Ag-Pt nanocubes compared to pure Ag nanocubes likely because of the dielectric properties of Pt metal.[15,16]
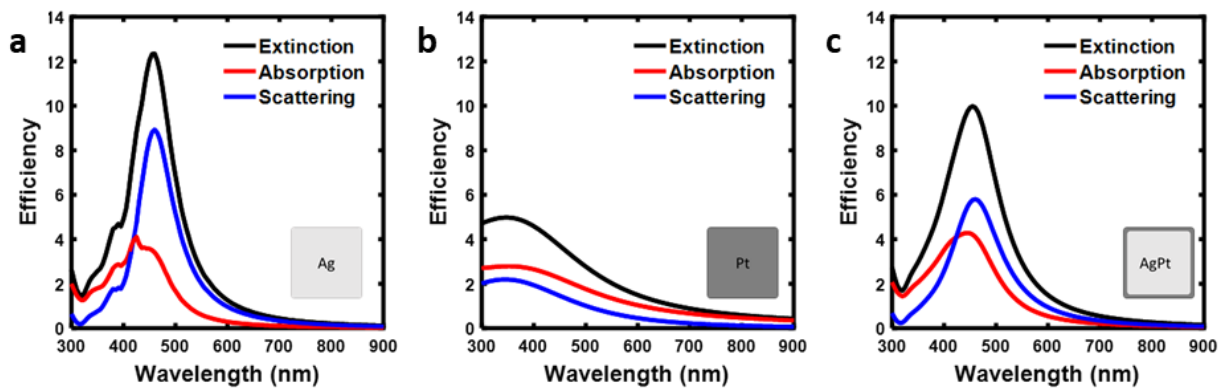
Figure 6.3 Simulated optical extinction efficiencies. Calculated extinction efficiencies for a **(a)** monometallic Ag nanocube, **(b)** monometallic Pt nanocube, and **(c)** Ag-Pt core-shell nanocube.

To directly compare the simulated data to the experimental data, we normalized the extinction of Ag and Ag-Pt nanocubes to 1 and calculated the absorption and scattering fractions. The calculated extinction, absorption and scattering fraction for pure Ag and Ag-Pt core-shell nanocubes (Figure 6.4a, b and c) are fully consistent with the experimental measurements, showing that the extinction is largely unchanged with the introduction of a thin Pt shell and that the absorption is more dominant in the nanomaterials that contain Pt compared to pure Ag.

We have also used these simulations to analyze the power dissipated (i.e., the rate of photon absorption through the formation of energetic charge carriers, e-h pairs) through the thin Pt shell of an Ag-Pt core-shell nanocube and an Ag shell of the equivalent dimensions on a pure Ag nanocube. Data in Figure 6.5 show contour plots of the power dissipated in a quarter of a nanocube for Ag and Ag-Pt. For Ag, there is some concentration of power dissipation at the corners of the nanocube, but most of the energy is uniformly distributed throughout the nanostructure. In contrast, when Pt is coated onto an Ag nanocube, most of the power dissipation occurs in the thin 1 nm shell of Pt at the surface of the nanoparticles.
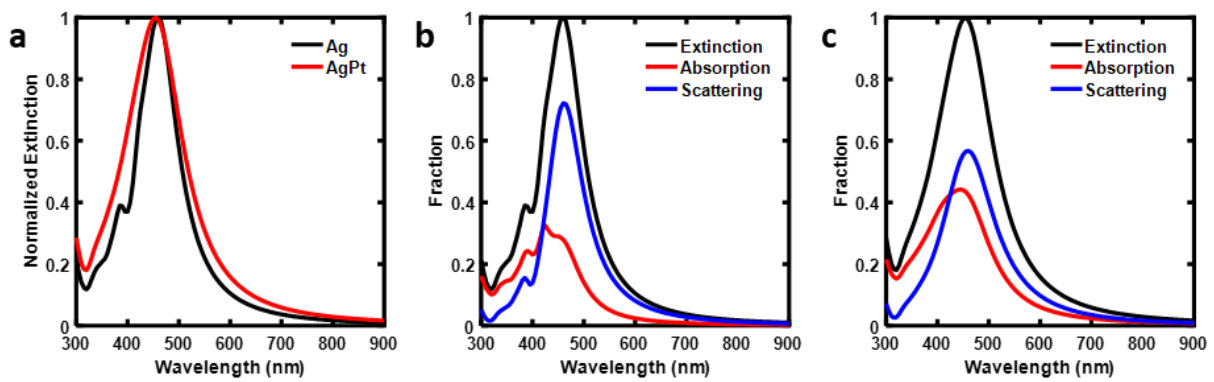
Figure 6.4 Simulated extinction fractions. **(a)** Simulated normalized extinction fraction spectra for Ag and Ag-Pt nanocubes. **(b)** Simulated breakdown of extinction fraction in absorption and scattering for a Ag nanocube. **(c)** Simulated breakdown of extinction fraction into absorption and scattering for a Ag-Pt nanocube.
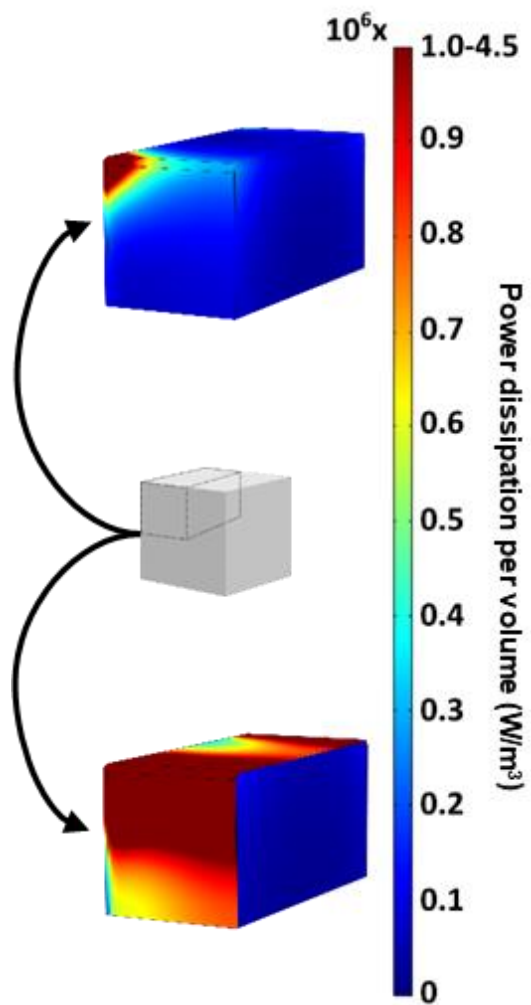
Figure 6.5 Contour plot of power dissipation. Contour plot of power dissipation in a quarter of a Ag (top) and Ag-Pt (bottom) nanocube.

To breakdown the absorption further, we normalized the peak absorption of a pure Ag, pure Pt, and Ag-Pt nanocube and decomposed the absorption into core (i.e. the inner 75 nm of the particles) or shell (i.e. the outermost 1.2 nm) components. For the cases where we have monometallic Ag and Pt nanocubes, nearly all of the absorption in these materials takes place in the 75 nm core of the nanoparticles. One the other hand, for the Ag-Pt nanocubes, we see a drastic switch in the spatial distribution of absorption where most of the absorption now takes place in the thin 1.2 nm of Pt at the surface of the nanocube. The rate of absorption per unit volume in the Pt shell is ~ 22 times larger than the rate of absorption in the core over the visible light wavelength range (300-900 nm). In comparison, for the same thickness of an Ag shell in an Ag nanoparticle of identical size and shape, the rate of absorption per unit volume in the shell is only ~ 3 times larger than the rate of absorption in the core. We note that a similar analysis of our integrating sphere experimental data shows the rate of absorption per unit volume in a thin Pt shell (1.2 nm) was ~ 18 times larger than the rate of absorption in the Ag core, in relative agreement with the FEM simulations.

6.6 Mechanism of Energy Transfer from Plasmonic Materials to Catalytically Active Sites

The data above strongly suggest that the energy of light captured by the plasmonic Ag core is directly dissipated through the thin Pt shell. This challenges the commonly accepted mechanism of energy transfer from plasmonic materials to catalytic active sites. In the conventional mechanism, light interacts with the plasmonic metal exciting LSPR. Plasmon decay in the metal then excites energetic charge carriers which can transfer to the catalytic metal thereby donating a portion of the energy collected via plasmon excitation.[17–19] The experiments presented in this chapter allow us to rule out charge transfer from the plasmonic metal (Ag) to the catalytic metal (Pt). The integrating sphere measurements show that the absorption rates (e/h formation rates)

increases when Ag is coated with Pt. If charge transfer from Ag played a role, we would not expect the absorption to change when Pt is coated on the Ag nanoparticles. This Pt-induced increase in nanoparticle absorption can be explained by charge carriers being produced directly in the Pt atoms through electronic excitations in Pt. This is further supported by our integrating sphere measurements of Ag-Pt nanocubes with varying shell thicknesses. These data show that the absorption increases as the thickness of the Pt shell increases. This cannot be explained by charge transfer from Ag to Pt since charge transfer should be independent of the thickness of the Pt shell. Instead, the absorption increases because it is taking place directly in Pt. Additionally, all experimental data are strongly supported by the electrodynamic simulations which do not account for the movement of charge in materials (i.e. all movement of energy is facilitated by electromagnetic fields).

We have also recently investigated this energy transfer mechanism in more detail. From this work, it is clear that the two main requirements for energy transfer are (1) high electric field intensities provided by LSPR excitation of plasmonic metals and (2) the availability of direct, momentum-conserved electronic transitions in the catalytic material at the LSPR excitation frequencies. By positioning the catalytic material at the positions where the electric field intensities are the highest (i.e. at the surface of the plasmonic metal), the energy transfer from the plasmonic metal to the catalytic metal can be maximized. A crucial feature of this mechanism is that it avoids, to a large extent, the loss of energy via absorption in the plasmonic metal allowing for high energy carriers to be generated directly in the catalytic metal.[20,21]

6.7 Conclusions

We have demonstrated the ability to control the energy flow in plasmonic systems at the nanoscale through the targeted synthesis of multicomponent plasmonic nanostructures. By

completely coating a plasmonic metal (Ag) nanocube possessing low imaginary dielectric function with a few atomic layers of a catalytic metal (Pt) possessing high imaginary dielectric function, a channel for plasmon decay was introduced leading to the dissipation of light energy through the thin Pt shell. In the next chapter, we design photocatalytic reactor studies to test whether this transfer of energy enables plasmon-enhanced reactions to take place on non-plasmonic metal surfaces.

6.8 References

1. Amendola, V., Saija, R., M. Maragò, O. & Antonia Iatì, M. Superior plasmon absorption in iron-doped gold nanoparticles. *Nanoscale* **7,** 8782–8792 (2015).

2. Linic, S., Aslam, U., Boerigter, C. & Morabito, M. Photochemical transformations on plasmonic metal nanoparticles. *Nat Mater* **14,** 567–576 (2015).

3. Aslam, U. & Linic, S. Addressing Challenges and Scalability in the Synthesis of Thin Uniform Metal Shells on Large Metal Nanoparticle Cores: Case Study of Ag–Pt Core–Shell Nanocubes. *ACS Appl. Mater. Interfaces* **9,** 43127–43132 (2017).

4. Rakić, A. D., Djurišić, A. B., Elazar, J. M. & Majewski, M. L. Optical properties of metallic films for vertical-cavity optoelectronic devices. *Appl. Opt., AO* **37,** 5271–5283 (1998).

5. Fales, A. M., Yuan, H. & Vo-Dinh, T. Silica-Coated Gold Nanostars for Combined Surface-Enhanced Raman Scattering (SERS) Detection and Singlet-Oxygen Generation: A Potential Nanoplatform for Theranostics. *Langmuir* **27,** 12186–12190 (2011).

6. Antosiewicz, T. J., Wadell, C. & Langhammer, C. Plasmon-Assisted Indirect Light Absorption Engineering in Small Transition Metal Catalyst Nanoparticles. *Advanced Optical Materials* **3,** 1591–1599 (2015).

7. Zhang, L. *et al.* Platinum-based nanocages with subnanometer-thick walls and well-defined, controllable facets. *Science* **349,** 412–416 (2015).

8. Evanoff, D. D. & Chumanov, G. Size-Controlled Synthesis of Nanoparticles. 2. Measurement of Extinction, Scattering, and Absorption Cross Sections. *J. Phys. Chem. B* **108,** 13957–13962 (2004).

9. Langhammer, C., Kasemo, B. & Zorić, I. Absorption and scattering of light by Pt, Pd, Ag, and Au nanodisks: Absolute cross sections and branching ratios. *The Journal of Chemical Physics* **126,** 194702 (2007).

10. Jain, P. K., Lee, K. S., El-Sayed, I. H. & El-Sayed, M. A. Calculated Absorption and Scattering Properties of Gold Nanoparticles of Different Size, Shape, and Composition:

Applications in Biological Imaging and Biomedicine. *J. Phys. Chem. B* **110,** 7238–7248 (2006).

11. Kreibig, U. & Vollmer, M. *Optical Properties of Metal Clusters*. (Springer Science & Business Media, 2013).

12. Linic, S., Christopher, P. & Ingram, D. B. Plasmonic-metal nanostructures for efficient conversion of solar to chemical energy. *Nat Mater* **10,** 911–921 (2011).

13. Link, S. & El-Sayed, M. A. Spectral Properties and Relaxation Dynamics of Surface Plasmon Electronic Oscillations in Gold and Silver Nanodots and Nanorods. *J. Phys. Chem. B* **103,** 8410–8426 (1999).

14. Kelly, K. L., Coronado, E., Zhao, L. L. & Schatz, G. C. The Optical Properties of Metal Nanoparticles: The Influence of Size, Shape, and Dielectric Environment. *J. Phys. Chem. B* **107,** 668–677 (2002).

15. Kreibig, U. Interface-induced dephasing of Mie plasmon polaritons. *Appl. Phys. B* **93,** 79–89 (2008).

16. Linnert, T., Mulvaney, P. & Henglein, A. Surface chemistry of colloidal silver: surface plasmon damping by chemisorbed iodide, hydrosulfide (SH-), and phenylthiolate. *J. Phys. Chem.* **97,** 679–682 (1993).

17. Zheng, Z., Tachikawa, T. & Majima, T. Single-Particle Study of Pt-Modified Au Nanorods for Plasmon-Enhanced Hydrogen Generation in Visible to Near-Infrared Region. *J. Am. Chem. Soc.* **136,** 6870–6873 (2014).

18. Sarina, S. *et al.* Enhancing Catalytic Performance of Palladium in Gold and Palladium Alloy Nanoparticles for Organic Synthesis Reactions through Visible Light Irradiation at Ambient Temperatures. *J. Am. Chem. Soc.* **135,** 5793–5801 (2013).

19. Lou, Z., Fujitsuka, M. & Majima, T. Pt–Au Triangular Nanoprisms with Strong Dipole Plasmon Resonance for Hydrogen Generation Studied by Single-Particle Spectroscopy. *ACS Nano* **10,** 6299–6305 (2016).

20. Boerigter, C., Campana, R., Morabito, M. & Linic, S. Evidence and implications of direct charge excitation as the dominant mechanism in plasmon-mediated photocatalysis. *Nat Commun* **7,** 10545 (2016).

21. Boerigter, C., Aslam, U. & Linic, S. Mechanism of Charge Transfer from Plasmonic Nanostructures to Chemically Attached Materials. *ACS Nano* **10,** 6108–6115 (2016).

Chapter 7 Performing Plasmonic Catalysis on Non-Plasmonic Metal Surfaces

7.1 Summary

Having shown that LSPR excitation of the Ag-Pt nanocubes leads to the dissipation of energy through the thin Pt shell, we design reactor studies to test whether this funneling of energy to the Pt shell enables plasmon-driven reactions to take place on this non-plasmonic metal surface. We prepare a catalyst from the Ag-Pt core-shell nanocubes and perform preferential oxidation of carbon monoxide in excess hydrogen as a probe reaction. We show that illuminating the catalyst with low intensity visible light under reaction conditions results in an increase in the rate of the reaction. By using mass spectrometry to characterize the residence time of an inert gas in our system, we show that this increase in reaction rate is essentially instantaneous. Furthermore, wavelength-dependent experiments show that the increase in the reaction rate on the Pt surface is driven by plasmon excitation from the particle core. Collectively, these data demonstrate that the energy capture by the Ag core can be used drive plasmon-mediated chemical reactions on the surface of Pt.

7.2 Introduction

The excitement surrounding plasmonic catalysis stems from the ability to use the excitation of energetic charge carriers (as opposed to heat) to drive surface chemistry.[1–3] This offers the

opportunity to potentially discover new, more selective reaction pathways that cannot be accessed in temperature-driven catalysis.[4–6] A major limitation in the nascent field of plasmonic catalysis is that the plasmonic metals (Cu, Ag, and Au) are inherently catalytically-limited which significantly shrinks the phase space of chemical transformations that could benefit from this phenomenon.[7,8] Ideally, we would like to be able to perform plasmon-driven (or charge carrier-driven) reactions on the surfaces of catalytically-relevant metals (such as Pt, Pd, etc.), but these materials do not undergo plasmon excitation with visible light photons and thus have small optical cross sections.[9,10]

In the previous chapters, we outlined the design of a hybrid bimetallic nanostructure that could potentially combine the optical properties of plasmonic metals with the catalytic properties of other transition metals to enable plasmonic catalytic on non-plasmonic metals. We developed a highly-scalable synthesis procedure for making such materials (Ag-Pt core-shell nanocubes) and performed detailed spectroscopic experiments showing that the hybrid materials displayed the surface chemical properties of Pt and optical properties of Ag.[11] Furthermore, we designed optical experiments and simulations to show that the energy of the plasmon excitation in the Ag core was dissipated in Pt through direct electronic excitations (formation of energetic charge carriers) in the thin Pt shell.

Herein, we test the photocatalytic performance of these materials in reactor studies using the preferential oxidation of CO in excess H_2 as a probe reaction. This reaction is commonly performed to purify H_2 gas following steam reforming where the goal of the reaction is to oxidize harmful CO to CO_2 and minimize any oxidation of the valuable product, H_2.[12] Pt surfaces are typically used to perform this chemical transformation as they display high selectivity towards the oxidation of CO.[13,14] In contrast, Ag surfaces provide very low selectivity toward CO oxidation

and mainly oxidize H_2. As such, the selectivity of this reaction can be used as a chemical indicator of which metal is performing surface chemistry. We design experiments to test whether plasmon excitation from the Ag core can be used to drive Pt surface chemistry.

7.3 Methods

7.3.1 Catalyst Preparation

The Ag/Al_2O_3 catalyst was prepared by mixing 100 mg of α-Al_2O_3 (Alfa Aesar) in water followed by the dropwise addition of an entire sample of Ag nanocubes. After 1 hour of mixing, 300 μL of a 1 M aqueous $NaNO_3$ solution was added to the 25 mL mixture of Ag nanocubes and α-Al_2O_3. The addition of the salt destabilizes the colloidal solution of Ag nanocubes and causes the nanoparticles to deposit onto the α-Al_2O_3 support. The slurry is allowed to mix for 3 hours, and the Ag/Al_2O_3 catalyst is then separated from the liquid and washed in water via centrifugation. The metal loading of the catalyst was estimated by measuring the mass of nanoparticles in 1/10th of a sample. The estimated metal weight loading of the Ag/Al_2O_3 catalyst was ~7%.

The Ag-Pt/Al_2O_3 catalyst was prepared in the same way as the Ag/Al_2O_3 catalyst, but before the dropwise addition of the Ag-Pt nanoparticles, 300 μL of 1.25 M aqueous NaOH solution was added to the Al_2O_3 slurry. The estimated metal weight loading of the Ag-$Pt/Al_2O_3$was ~4%.

7.3.2 Thermal and Photothermal Preferential CO Oxidation

For the reactor experiments, 40 mg of the catalyst were loaded on top of 20 mg of SiO_2 beads in a Harrick micro-reactor. The reactor is equipped with a SiO_2 window through which the catalyst can be illuminated. The catalyst was pretreated in the reactor with air at 250°C for 3 hours. The reactor was then cooled down to 200°C under N_2 flow. The reactants mixture (3% CO, 2% O_2, 75% H_2, balance N_2) was then introduced at a flow rate of 100 sccm and the system was allowed to reach steady state overnight (~12 hours). Data were collected at a range of temperatures

under both thermal (no catalyst illumination) and photothermal (catalyst illumination, light intensity of ~400 mW/cm^2. More specifically, thermal data was collected at a specific temperature for ~30 minutes followed by the collection of photothermal data for ~30 minutes and finally again collection of thermal data. Then the temperature was increased and the process repeated for the new temperature. The reaction was operated at differential conversion ($<$ 10% conversion of O_2) to minimize mass transport (i.e. diffusion) limitations of the reactants to the catalytic sites and minimize thermal gradients as a result of the exothermic oxidation of H_2 and CO.[11] This ensures we are operating in a kinetically-limited regime and are measuring changes only in the reaction kinetics. The product gases were analyzed using a combination of gas chromatography and mass spectrometry. The reaction rate was calculated in terms of O_2 consumption per gram of metal catalyst per second. The selectivity towards CO_2 was calculated as

$$S_{CO_2} = \frac{P_{CO_2}}{P_{CO_2} + P_{H_2O}}$$

where S_{CO2} is the selectivity towards CO_2 and P_n is molar flow rate of product n. The error bars on all data represent one standard deviation from the mean.

7.3.3 Wavelength-Dependent Photothermal CO Preferential Oxidation

A combination of shortpass and longpass filters were used in conjunction with a broadband visible light source to perform the wavelength-dependent photothermal reaction experiments. The intensity of light through the stacked filters was measured using a thermopile detector positioned to provide an accurate measurement of light intensity at the top of the catalyst bed. The common maximum attainable light intensity through the filters was ~180 mW/cm^2. The reaction study was performed using the same startup procedure as the variable-temperature reactor study detailed earlier, but this experiment was performed at a single temperature (160°C) and different sets of filters were used for the photothermal measurements. The visible light passing through the filters

140

was measured using transmission UV-vis spectroscopy and centered at 512 nm, 525 nm, 550 nm, 575 nm, 600 nm, and 625 nm for the six different sets of filters.

7.3.4 Catalyst Absorption Spectrum

The absorption spectrum of the catalyst under operating conditions was measured using in situ diffuse reflectance UV-vis spectroscopy. A spectrum of α-Al$_2$O$_3$ was also acquired and subtracted from the Ag-Pt/Al$_2$O$_3$ spectrum to obtain only the absorption from the Ag-Pt nanoparticles. This absorption was then normalized by subtracting the minimum and dividing to set the maximum to a value of 1.

7.4 Catalyst Synthesis

To test the photocatalytic performance of the Ag-Pt core-shell nanocubes, we must first prepare a catalyst from the colloidal solution of nanoparticles. We prepare two catalysts for the photocatalytic reactor studies, a control catalyst consisting of Ag nanocubes supported on α-Al$_2$O$_3$ and our test catalyst of Ag-Pt nanocubes deposited on α-Al$_2$O$_3$. Alumina was chosen as the support material as it does not absorb light in the visible range, is inert in the preferential oxidation of CO in excess H$_2$, and is commonly used to support metal catalysts for oxidation reactions.[15]

It can often be challenging to deposit colloidal nanoparticles onto support materials. We developed a method to do this by mixing α-Al$_2$O$_3$ powder with our colloidal nanoparticles. We then add a set amount of an aqueous salt solution to the mixture under stirring. The salt increases the ionicity of the dispersion causing the electrical double layer surrounding the colloidal nanoparticles to become unstable. This forces the colloidal dispersion to collapse which causes the nanoparticles to stick onto any available surface in the slurry (i.e. the α-Al$_2$O$_3$). For depositing the Ag nanocubes onto α-Al$_2$O$_3$, we use a sodium nitrate (NaNO$_3$) solution as our salt (also known as a flocculent). After the nanoparticles are deposited, the catalyst is washed via centrifugation twice

to remove excess salt and stabilizing agent. An STEM image of the resulting Ag/α-Al$_2$O$_3$ catalyst

is shown in Figure 7.1. This image shows that the Ag nanocubes are successfully deposited with
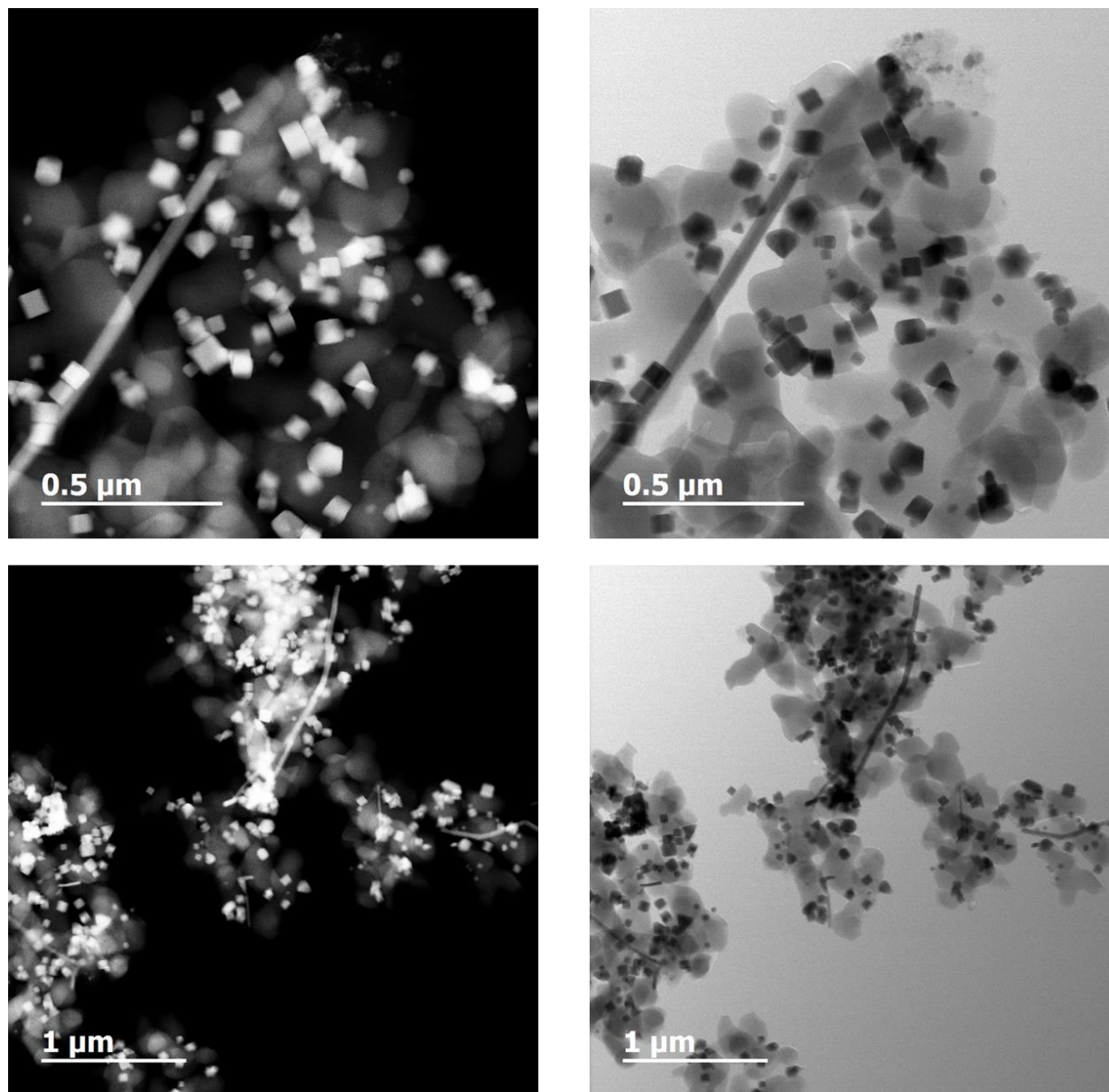
relatively good dispersion onto the α-Al$_2$O$_3$ support.

Figure 7.1 STEM images of as-prepared Ag catalyst. STEM images of Ag nanocubes deposited on α-Al$_2$O$_3$ following the catalyst preparation process.

To prepare the Ag-Pt/α-Al$_2$O$_3$ catalyst, we initially tried using NaNO$_3$ as the salt flocculent; however, the resulting catalyst displayed no reactivity. Upon further investigation using STEM to characterize the catalyst, it was found that the Ag-Pt nanocubes became unstable during the catalyst preparation process. The STEM image in Figure 7.2 shows that the Ag from the core of the nanocubes appears to have leeched out and messily redeposited on the surface of the nanocubes. Through prior experience with these Ag-Pt nanocubes, we knew that the nanocubes were highly sensitive to acidic conditions and always needed to be stored in base to stay stable. We hypothesized that the instability of the nanocubes during the catalyst preparation was a consequence of neutral pH conditions used in the process. This may have resulted in pockets of slightly low pH forming in the mixture causing the Ag to leech from the cores. To prevent this, we begin the catalyst preparation by adding NaOH to a slurry of α-Al$_2$O$_3$ in water to increase the pH to ~12. Then, we use NaOH as our salt flocculent in place of NaNO$_3$. Using this deposition process, we were able to successfully deposit the Ag-Pt nanocubes onto the α-Al$_2$O$_3$ support. The STEM image in Figure 7.3 shows that the nanocubes are deposited with good dispersion onto the oxide support. Furthermore, by locating Ag-Pt nanocubes that are oriented properly in the microscope, we see that the Pt shells remains intact on the Ag nanocube cores.
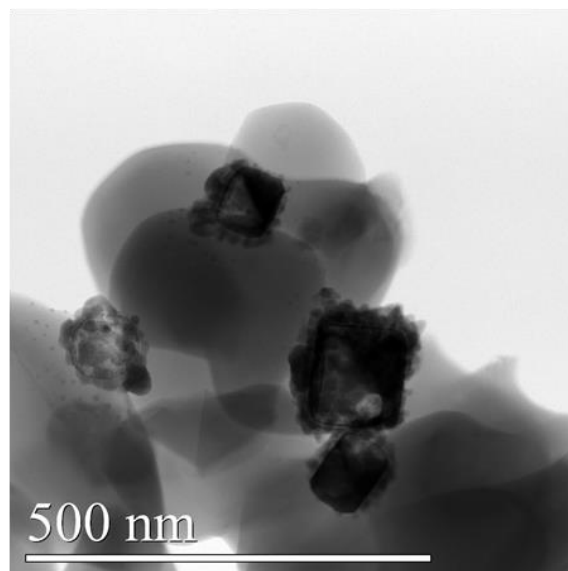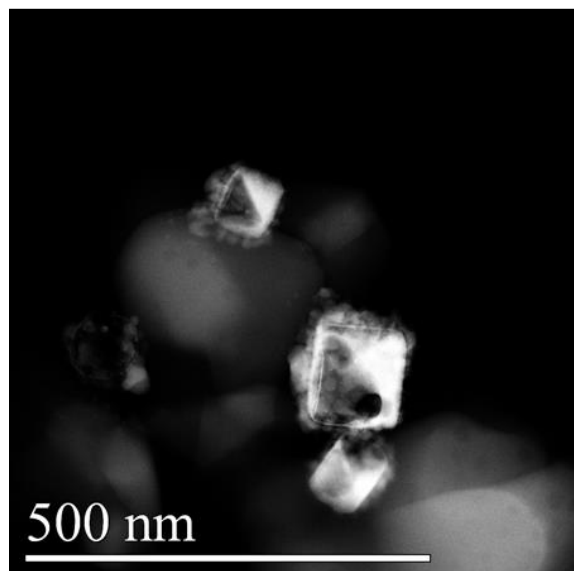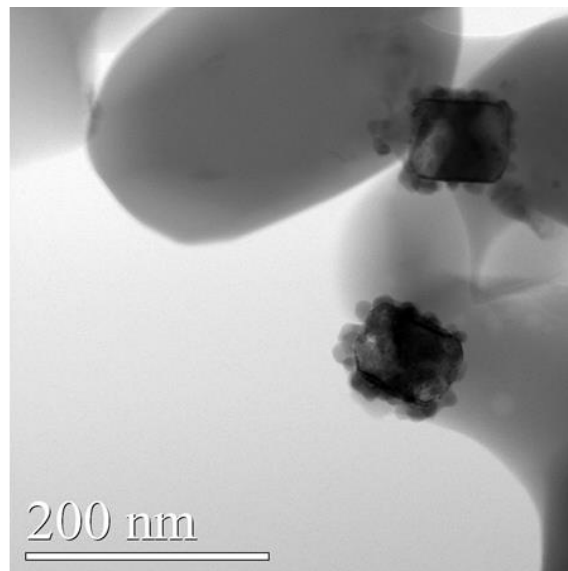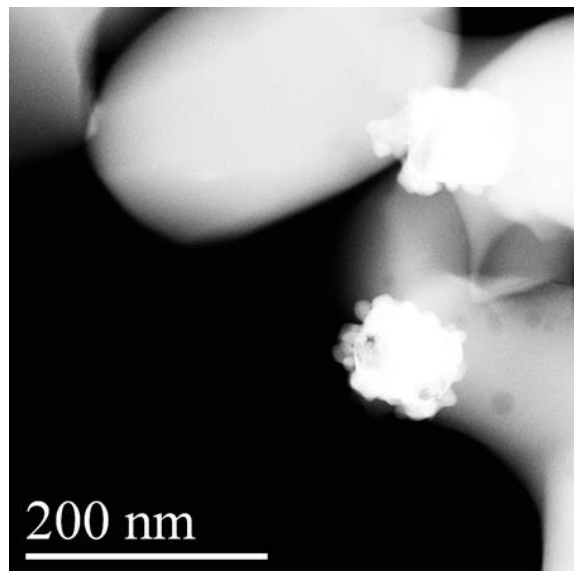
Figure 7.2 STEM images of failed Ag-Pt catalyst preparation. Ag-Pt core-shell nanocubes on α-Al$_2$O$_3$ following the catalyst preparation procedure using NaNO$_3$ as a flocculent. The Ag core leeches out of the core-shell nanocubes.
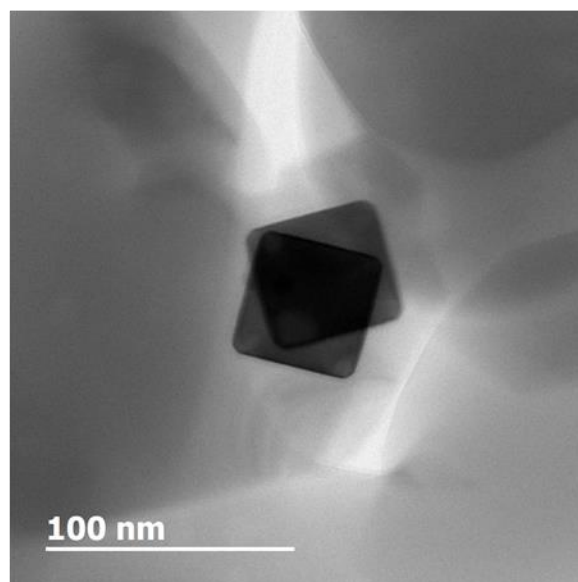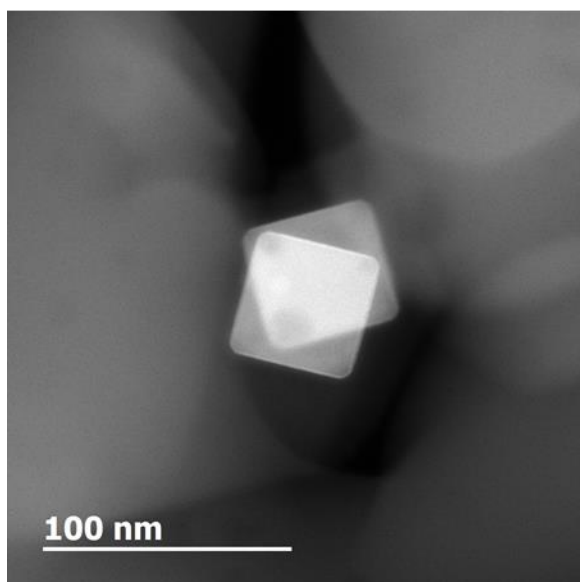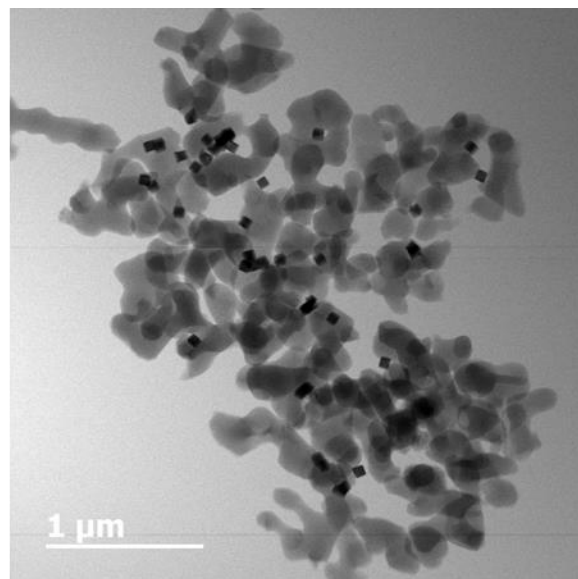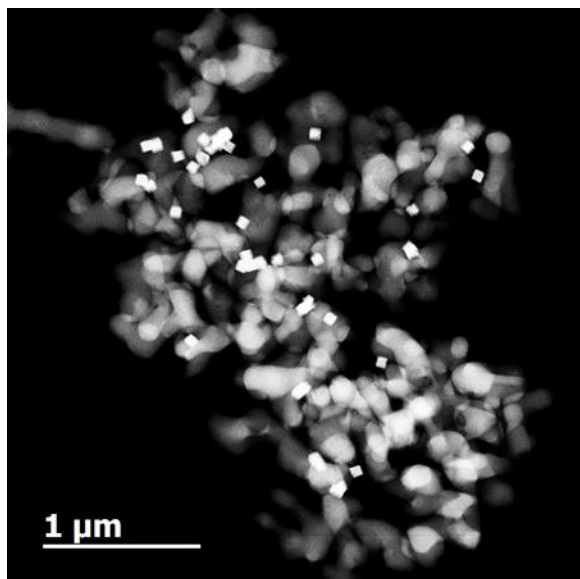
Figure 7.3 STEM images of as-prepared Ag-Pt catalyst. Ag-Pt core-shell nanocubes on α-Al$_2$O$_3$ following the catalyst preparation procedure using NaOH as a flocculent. The nanocubes retain their cubic structure and separation of Ag and Pt.

7.5 Reactor Studies

We perform photocatalytic reaction experiments in a packed-bed reactor equipped with a glass window for catalyst illumination using a broadband visible light source at an intensity of ~ 400 mW/cm^2. Once the catalyst is loaded into the reactor, we pretreat the catalyst with 100 sccm of air at 250°C for 3 hours to burn off any residual organics and other contaminants. This is followed by a treated with 20% H_2 in N_2 at a flowrate of 100 sccm for 1 hour at 200°C to reduce any potential oxides formed during the air treatment. Preferential CO oxidation in excess H_2 is performed on the Ag-Pt catalyst with 75% H_2, 2% O_2, 3% CO, and balance N_2 at temperatures ranging from 130-180°C at differential reactant conversions (below 10%). This is done to ensure that we are operating in a kinetically-limited regime which allows us to attribute any photocatalytic increase in the reaction rate to an increase in reaction kinetics.[16,17] In addition, control experiments are performed on a monometallic Ag catalyst under the same flow conditions at temperatures ranging from 200-260°C. Higher temperatures are necessary for the Ag catalyst because Ag surfaces are less active for the reaction.

Data in Figure 7.4a show the activity of the control Ag/α-Al$_2$O$_3$ catalyst versus temperature under both thermal and photothermal conditions. These data show an exponential increase of reaction rate with temperature, as we would expect when operating in the kinetically-limited reaction regime.[15] Furthermore, we observe no significant increase in the reaction rate upon illumination of the catalyst under operating conditions. It has been shown that photoexcitation of plasmonic Ag nanostructures can enhance the rates of oxidation reactions for which O_2 dissociation is rate limiting.[18,19] The Ag catalysts in these experiments are mainly performing H_2 oxidation. We believe that the Ag nanocubes are mainly covered with hydrogen and that O_2 dissociation is not rate controlling for H_2 oxidation on Ag.

In contrast to the Ag catalyst performance, activity data for the Ag-Pt/α-Al$_2$O$_3$ catalyst show a marked increase in the reaction rate under illumination at every temperature tested. These data show that the Ag-Pt core-shell nanocubes are effectively able to harness the energy of visible light to drive chemical reactions. Furthermore, the lack of any reaction rate increase for the Ag control catalyst implies that illumination of the catalyst bed does not result in bulk heating of the reactor or catalyst bed by the light source. This suggests that the photo-enhanced reaction rates are a product of plasmon excitation.

To test whether the reaction is taking place on the Pt surface, we analyzed the selectivity of the catalyst towards CO_2. As mentioned earlier, it is well-established that Pt can execute the preferential oxidation of CO in excess H_2 with high CO oxidation selectivity, while Ag shows very poor reaction selectivity (i.e. on Ag, H_2 is selectively oxidized).[12,20] The selectivity data in Figure 7.4c show that our control Ag/α-Al$_2$O$_3$ catalyst displays almost no selectivity towards CO oxidation as expected. In contrast, the Ag-Pt nanocubes express very high CO oxidation selectivity at low reaction rates. The selectivity then decreases as the reaction rate increases. This selectivity behavior is typical of preferential CO oxidation on Pt surfaces. At low reaction rates, the Pt surface is completely covered in CO which allows for only the oxidation of CO at low reaction rates. As the reaction rate increases, free Pt surface sites become abundant allowing for H_2 to adsorb onto the surface and react with O_2 thereby driving down the selectivity towards CO oxidation at high reaction rates. Collectively, the data in Figure 7.4 suggest that the Ag-Pt core-shell nanocubes are effectively able to collect the energy of visible light and use that energy to drive Pt surface chemistry.
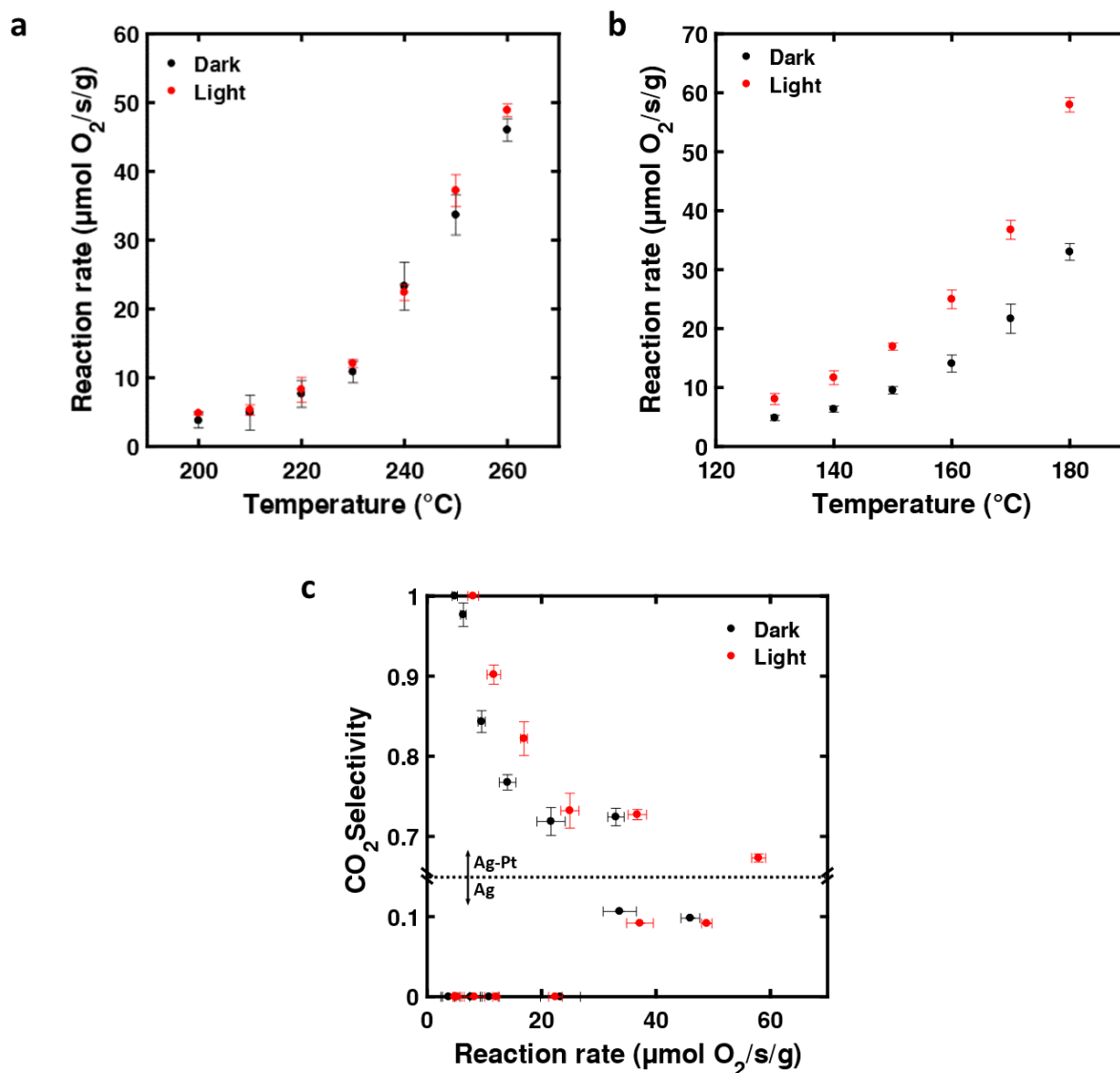
Figure 7.4 Reactivity data for Ag and Ag-Pt catalysts. (a) Reaction rate vs temperature for preferential CO oxidation in excess H_2 on Ag nanocubes under light-off and light-on conditions. **(b)** Reaction rate vs temperature for preferential CO oxidation in excess H_2 on Ag-Pt core-shell nanocubes under light-off and light-on conditions. **(c)** Selectivity towards CO oxidation vs reaction rate on Ag-Pt core-shell nanocubes and Ag nanocubes. Note the break in the vertical axis. There was no CO_2 detectable at low reaction rates on Ag, i.e., this catalyst preferentially oxidizes H_2 rather than CO. Error bars in all plots represent one standard deviation from the average.

7.6 Post-Reaction Characterization

Given the stability issues experienced with the Ag-Pt core-shell nanocubes during the catalyst preparation, we characterized both the control Ag/α-Al$_2$O$_3$ and the Ag-Pt/α-Al$_2$O$_3$ catalysts following the high temperature reaction study. The STEM image of the Ag/α-Al$_2$O$_3$ catalyst post reaction (Figure 7.5a) shows that the Ag nanocubes did not maintain their structure during the experiment. Instead, the nanocubes appear to have reshaped into spherical Ag nanoparticles. This is not surprising given the relatively low melting temperature of Ag and the tendency for Ag nanoparticles to sinter.[21] In contrast, the Ag-Pt nanocubes (Figure 7.5b) retain their cubic morphology and maintain the separation of the Ag core and Pt shell. These data show that the Ag-Pt nanocubes not only remained stable throughout the photocatalytic reactor study but that the Pt shell also seems to provide some thermal stability to the cubic Ag core.
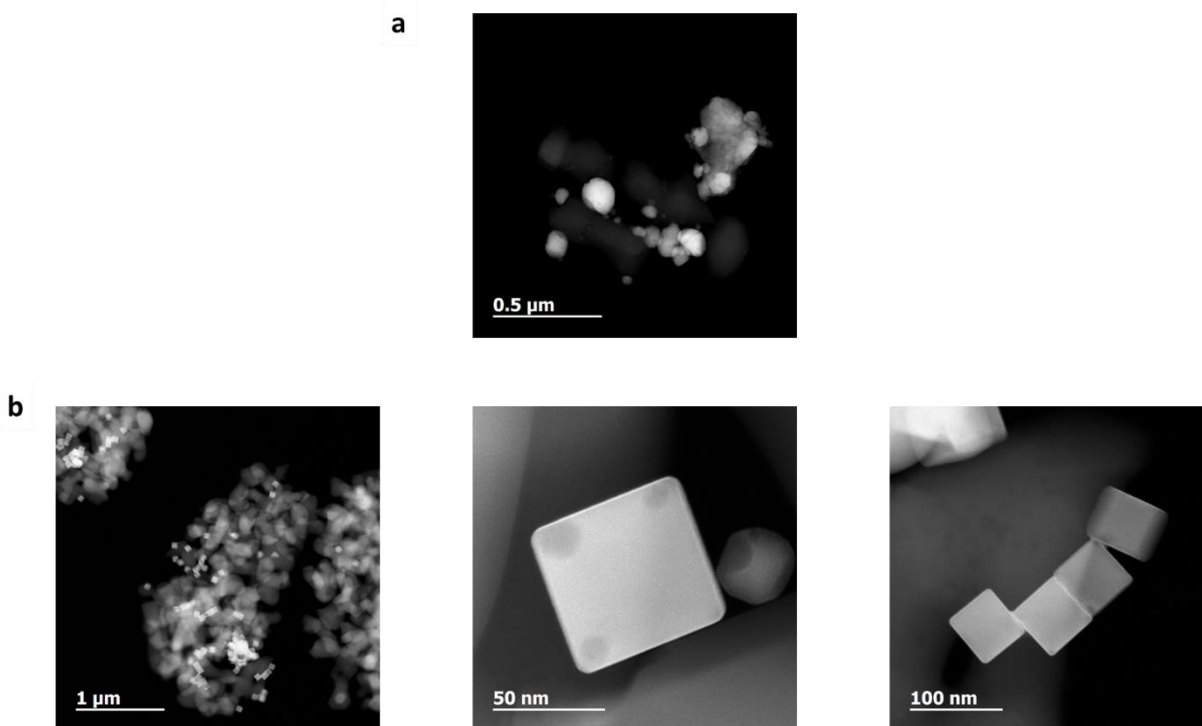
Figure 7.5 STEM images of catalysts post-reaction. (a) STEM image of Ag nanocube catalyst post-reaction. The nanocubes loss their cubic structure and form spherical particles. **(b)** STEM images of Ag-Pt nanocubes post-reaction. The core-shell nanocubes maintain both their morphology and the segregation of the Ag core and Pt shell.

150

7.7 Characterizing the Time Response of the Photocatalytic Enhancement

To build more evidence for the role of plasmon excitation in the observed photocatalytic rate enhancement on the Ag-Pt nanocube catalyst, we designed mass spectrometry experiments to characterize the temporal response of the catalyst to visible light illumination. In the case of bulk heating of the catalyst bed by the visible light source, we would expect a gradual increase in the reaction rate upon illumination as the catalyst bed slowly gains thermal energy. One the other hand, if plasmon excitation is playing the dominant role, we expect the increase in the reaction rate to be instantaneous as the processes associated with plasmon-enhanced reactions (summarized in Chapter 2) take place on the femtosecond-to-picosecond timescales.[22–24]

The experiment is performed by analyzing mass 44 (for CO_2) on-line using a mass spectrometer with a sampling rate of 1 s. The signal for CO_2 is allowed to reach steady state at a constant temperature of 150°C followed by visible light illumination (~400 mW/cm^2) of the catalyst. Data in Figure 7.6a show that the CO_2 signal quickly increases upon visible light illumination. We then switched off the light source and the signal returned to the dark baseline. This was repeated several times to show that the increase in the reaction rate was both repeatable and reversible. However, upon close inspection of the data in Figure 7.6a, it is clear that there is a short delay between when the light source is switched on and when the signal for CO_2 increases. This delay could be due to bulk heating of the catalyst by the light source or from the time it takes the gases to leave the reactor and reach the mass spectrometer.

To distinguish between these two and better characterize the time response of the system to visible light irradiation, we performed a pulse experiment through our reactor setup. These experiments are used to characterize the residence time of gases through a reactor setup.[25] We introduce a pulse of He gas to the inlet of the reactor for 1 s. This pulse is detected by the mass

spectrometer, as shown in the data in Figure 7.6b. The maximum of the He signal is normalized to match the intensity of the CO_2 signal maximum. Then, by integrating the pulse signal over time, we can directly compare the residence time of the He pulse through the reactor setup to the time response of the CO_2. This comparison shows that the increased production of CO_2 upon illumination of the catalyst is essentially instantaneous within the sampling rate of our system (< 1 s, Figure 7.6c). This instantaneous increase in the reaction rate rules out bulk heating of our catalyst bed by the light source and supports our hypothesis that the increase in reaction rate under visible light illumination is a result of plasmon excitation by the Ag nanocube core.

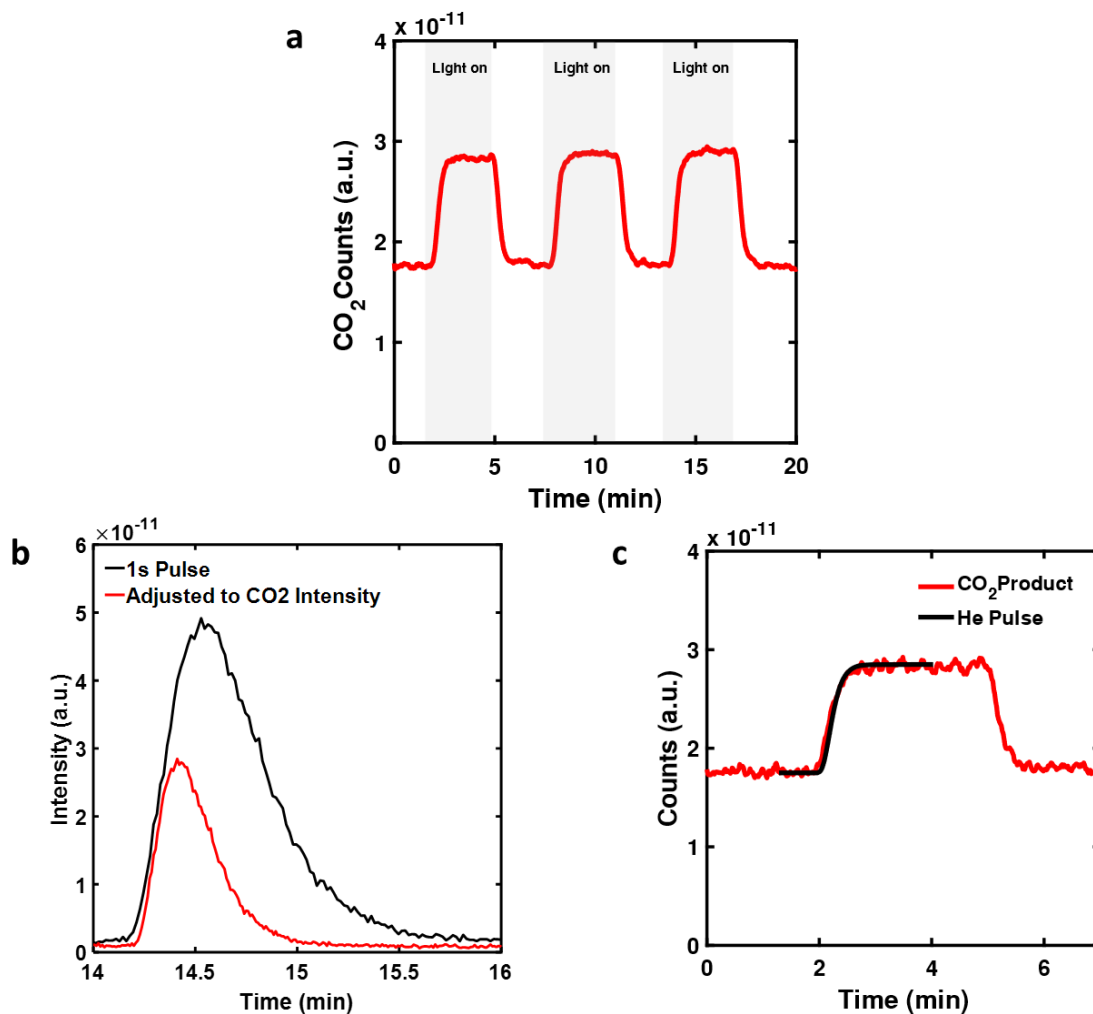**Figure 7.6 Mass spectrometry experiments.** **(a)** Fast-response mass spectrometry analysis of CO_2 product during cycling of light-on and light-off conditions. **(b)** He pulse signal detected by mass spectrometer. **(c)** Pulse experiments characterizing the time response of the Ag-Pt catalyst to illumination compared with the time response of the system to an inert He pulse introduced at the inlet of the reactor.

7.8 Wavelength-dependent Experiments

The data in Figures 7.4 and 7.6 suggest that some nanoscale electronic excitation phenomenon (such as plasmon excitation) is producing the enhanced rates of reaction on the Pt surface. To build more evidence for the role of plasmon excitation in these photocatalytic reactor studies, we perform photocatalytic reactor studies in which the wavelength of visible light is limited to specific ranges. The photocatalytic reaction rate under these conditions can then be matched with the absorption spectrum of the plasmonic catalysts under operating conditions to see if the largest photocatalytic rates are produced for wavelengths where the plasmon intensities are the greatest.[26,27]

We first measure the absorption spectrum of the Ag-Pt/α-Al$_2$O$_3$ catalyst under operating conditions using diffuse reflectance UV-vis spectroscopy. Data in Figure 7.7a show that the absorption spectrum of the catalyst shows a strong plasmon peak centered at ~420 nm. This is significantly blue-shifted from the plasmon peak for the colloidal Ag-Pt nanocubes due to the change in the dielectric constant of the medium from water to air.[18,28] We then measured the photocatalytic reaction rate for preferential CO oxidation on the Ag-Pt/α-Al$_2$O$_3$ using various sets of filters. The reaction rates are normalized to give the number of additional molecules produced per photon entering the reactor. This data is then overlaid on the catalyst absorption spectrum (Figure 7.7b). These data show a one-to-one mapping between the normalized photocatalytic rate and the nanoparticles optical absorption due to LSPR. This combined with the results from the reactor studies and mass spectrometry experiments conclusively demonstrates that the excitation of LSPR from the Ag nanocube core is directly responsible for the observed increase in the reaction rate for preferential CO oxidation on the Pt shell.
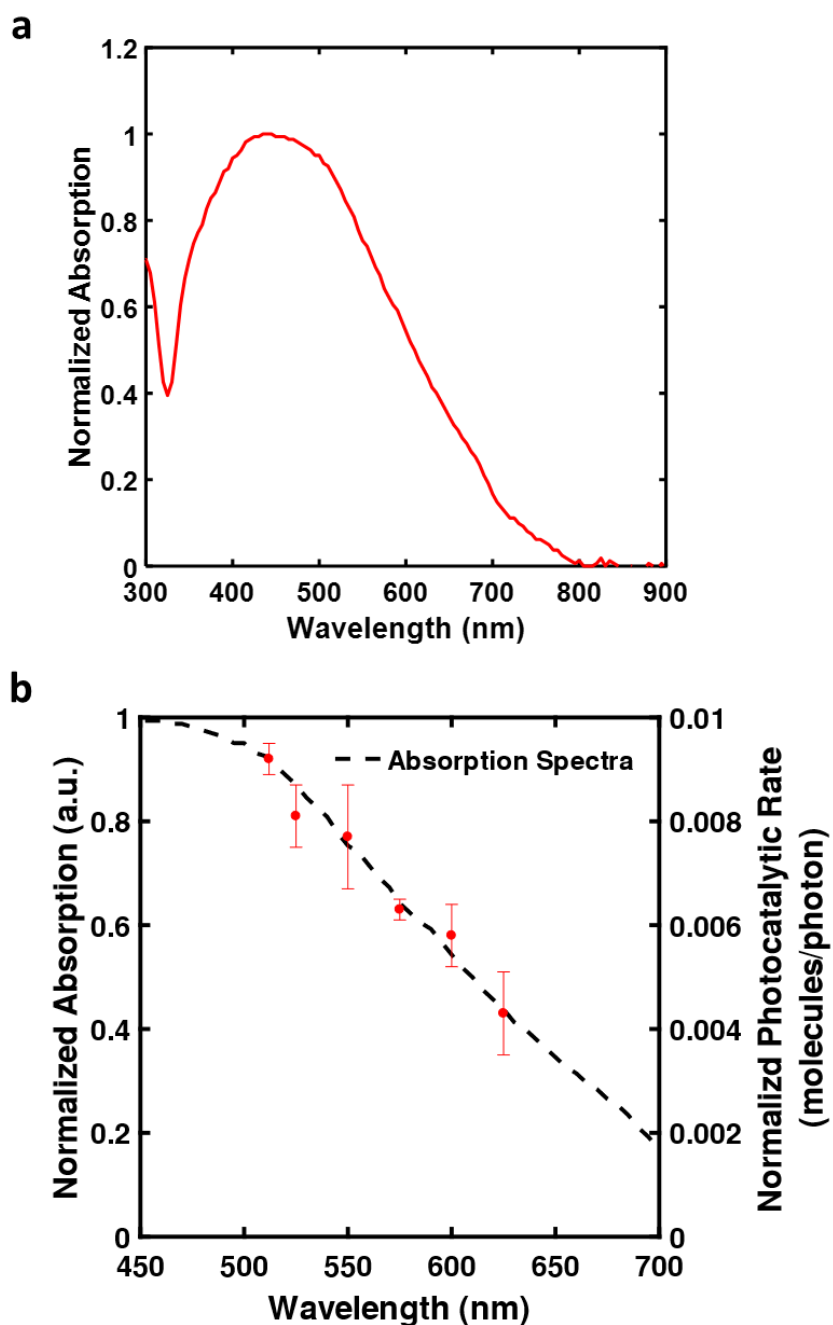
Figure 7.7 Wavelength-dependent experiments. (a) Diffuse reflectance UV-vis spectrum of Ag-Pt core-shell nanocube catalyst taken under preferential CO oxidation conditions. **(b)** Normalized absorption spectra of Ag-Pt nanocube catalyst, obtained under reaction conditions, plotted as a function of wavelength-dependent photo-catalytic reaction rate. The photocatalytic reaction rate was normalized by dividing by the photon flux at each wavelength. Error bars in all plots represent one standard deviation from the average.

7.9 Conclusions

Based on the optical data (chapter 6) and catalytic data presented in this chapter, we can shed light on the flow of energy in these multicomponent systems leading to plasmon-driven reactions on non-plasmonic active sites. The incoming electromagnetic radiation excites LSPR of the multicomponent plasmonic nanostructures, resulting in high overall extinction and elevated electric field intensities near the surface of the nanoparticles. The energy of the LSPR is dissipated through various available dissipation pathways. These dissipation pathways include photon scattering as well as absorption events (excitation of energetic charge carriers) at various parts of the nanostructure. In metal nanoparticles, these scattering and absorption events have their characteristic rates, with direct, vertical electronic excitations (in metals these are the excitations from d-states below the Fermi level to s-states above the Fermi level) being the fastest plasmon decay channel.[6,29] At visible photon energies, Ag does not allow for the direct, vertical d-to-s transitions since the d-states in Ag are well below the Fermi level and these electrons cannot be excited by visible photons.[30] On the other hand, Pt supports these fast electronic excitations. By positioning few layers of Pt on an Ag nanoparticle, we are effectively directing the LSPR energy towards selective dissipation through these Pt sites. Furthermore, this LSPR-decay channel is also enhanced by the presence of very high LSPR-induced electric field intensities at the surface layers of these nanostructures. This flow of energy concentrates a large fraction of electro-magnetic energy in the surface Pt atoms, effectively "energizing" these active Pt surface sites. We postulate that this selective LSPR-induced energizing of the Pt active centers ultimately leads to the selective heating of the most abundant reaction intermediate (CO) on the catalyst surface which results in elevated reactions rates. This heating of adsorbed CO can take place either through direct phonon-

phonon interactions with the hot Pt atoms or a LSPR-field mediated vibronic coupling induced by

direct, vertical electronic excitations in the Pt-CO surface complexes.

7.10 References

1. Linic, S., Christopher, P. & Ingram, D. B. Plasmonic-metal nanostructures for efficient conversion of solar to chemical energy. *Nat Mater* **10,** 911–921 (2011).

2. Boerigter, C., Campana, R., Morabito, M. & Linic, S. Evidence and implications of direct charge excitation as the dominant mechanism in plasmon-mediated photocatalysis. *Nat Commun* **7,** 10545 (2016).

3. Linic, S., Christopher, P., Xin, H. & Marimuthu, A. Catalytic and Photocatalytic Transformations on Metal Nanoparticles with Targeted Geometric and Plasmonic Properties. *Acc. Chem. Res.* **46,** 1890–1899 (2013).

4. Bonn, M. *et al.* Phonon- Versus Electron-Mediated Desorption and Oxidation of CO on Ru(0001). *Science* **285,** 1042–1045 (1999).

5. Linic, S., Aslam, U., Boerigter, C. & Morabito, M. Photochemical transformations on plasmonic metal nanoparticles. *Nat Mater* **14,** 567–576 (2015).

6. Boerigter, C., Aslam, U. & Linic, S. Mechanism of Charge Transfer from Plasmonic Nanostructures to Chemically Attached Materials. *ACS Nano* **10,** 6108–6115 (2016).

7. Hammer, B. & Norskov, J. K. Why gold is the noblest of all the metals. *Nature* **376,** 238–240 (1995).

8. Hammer, B. & Nørskov, J. K. Theoretical surface science and catalysis—calculations and concepts. in *Advances in Catalysis* (ed. Bruce C. Gates, H. K.) **Volume 45,** 71–129 (Academic Press, 2000).

9. Kelly, K. L., Coronado, E., Zhao, L. L. & Schatz, G. C. The Optical Properties of Metal Nanoparticles: The Influence of Size, Shape, and Dielectric Environment. *J. Phys. Chem. B* **107,** 668–677 (2002).

10. Link, S. & El-Sayed, M. A. Spectral Properties and Relaxation Dynamics of Surface Plasmon Electronic Oscillations in Gold and Silver Nanodots and Nanorods. *J. Phys. Chem. B* **103,** 8410–8426 (1999).

11. Aslam, U. & Linic, S. Addressing Challenges and Scalability in the Synthesis of Thin Uniform Metal Shells on Large Metal Nanoparticle Cores: Case Study of Ag–Pt Core–Shell Nanocubes. *ACS Appl. Mater. Interfaces* **9,** 43127–43132 (2017).

12. Nilekar, A. U., Alayoglu, S., Eichhorn, B. & Mavrikakis, M. Preferential CO Oxidation in Hydrogen: Reactivity of Core−Shell Nanoparticles. *J. Am. Chem. Soc.* **132,** 7418–7428 (2010).

13. Manasilp, A. & Gulari, E. Selective CO oxidation over Pt/alumina catalysts for fuel cell applications. *Applied Catalysis B: Environmental* **37,** 17–25 (2002).

14. Alayoglu, S., Nilekar, A. U., Mavrikakis, M. & Eichhorn, B. Ru–Pt core–shell nanoparticles for preferential oxidation of carbon monoxide in hydrogen. *Nat Mater* **7,** 333–338 (2008).

15. Chorkendorff, I. & Niemantsverdriet, J. W. *Concepts of Modern Catalysis and Kinetics*. (John Wiley & Sons, 2017).

16. Christopher, P. & Linic, S. Shape- and Size-Specific Chemistry of Ag Nanostructures in Catalytic Ethylene Epoxidation. *ChemCatChem* **2,** 78–83 (2010).

17. Christopher, P. & Linic, S. Engineering Selectivity in Heterogeneous Catalysis: Ag Nanowires as Selective Ethylene Epoxidation Catalysts. *J. Am. Chem. Soc.* **130,** 11264–11265 (2008).

18. Christopher, P., Xin, H. & Linic, S. Visible-light-enhanced catalytic oxidation reactions on plasmonic silver nanostructures. *Nat Chem* **3,** 467–472 (2011).

19. Christopher, P., Xin, H., Marimuthu, A. & Linic, S. Singular characteristics and unique chemical bond activation mechanisms of photocatalytic reactions on plasmonic nanostructures. *Nat Mater* **11,** 1044–1050 (2012).

20. Pozdnyakova, O. *et al.* Preferential CO oxidation in hydrogen (PROX) on ceria-supported catalysts, part I: Oxidation state and surface species on Pt/CeO2 under reaction conditions. *Journal of Catalysis* **237,** 1–16 (2006).

21. Hu, A. *et al.* Low temperature sintering of Ag nanoparticles for flexible electronics packaging. *Appl. Phys. Lett.* **97,** 153117 (2010).

22. Bosbach, J., Hendrich, C., Stietz, F., Vartanyan, T. & Träger, F. Ultrafast Dephasing of Surface Plasmon Excitation in Silver Nanoparticles: Influence of Particle Size, Shape, and Chemical Surrounding. *Phys. Rev. Lett.* **89,** 257404 (2002).

23. Lindstrom, C. D. & Zhu, X.-Y. Photoinduced Electron Transfer at Molecule−Metal Interfaces. *Chem. Rev.* **106,** 4281–4300 (2006).

24. Frischkorn, C. & Wolf, M. Femtochemistry at Metal Surfaces: Nonadiabatic Reaction Dynamics. *Chem. Rev.* **106,** 4207–4233 (2006).

25. Fogler, H. S. *Essentials of Chemical Reaction Engineering*. (Pearson Education, 2011).

26. Zheng, Z., Tachikawa, T. & Majima, T. Single-Particle Study of Pt-Modified Au Nanorods for Plasmon-Enhanced Hydrogen Generation in Visible to Near-Infrared Region. *J. Am. Chem. Soc.* **136,** 6870–6873 (2014).

27. Xiao, Q. *et al.* Visible Light-Driven Cross-Coupling Reactions at Lower Temperatures Using a Photocatalyst of Palladium and Gold Alloy Nanoparticles. *ACS Catal.* **4,** 1725–1734 (2014).

28. Stiles, P. L., Dieringer, J. A., Shah, N. C. & Duyne, R. P. V. Surface-Enhanced Raman Spectroscopy. *Annual Review of Analytical Chemistry* **1,** 601–626 (2008).

29. Khurgin, J. B. How to deal with the loss in plasmonics and metamaterials. *Nature Nanotechnology* **10,** 2–6 (2015).

30. Kreibig, U. & Vollmer, M. *Optical Properties of Metal Clusters*. (Springer Science & Business Media, 2013).

Chapter 8 General Conclusions and Future Directions

8.1 Summary

In this dissertation, we set out to push the boundaries of chemical reactions that can be performed using plasmonic catalysis. Specifically, we aimed to understand and design multicomponent plasmonic catalysts which could both collect the energy of visible light and direct that energy into catalytically-active sites. To do this, we considered the case of multimetallic plasmonic nanostructures composed of a plasmonic metal and a catalytically-active metal. We developed new synthesis approaches for Ag-Pt alloy and Ag-Pt core-shell nanoparticles. Using these materials, we performed spectroscopic and reactor experiments to show that these materials displayed the optical properties of plasmonic metals and the surface chemical properties of catalytic metals thereby enabling plasmonic catalysis on non-plasmonic metal surfaces. This work now opens the door for several exciting new directions in the areas of nanoparticle synthesis, multicomponent plasmonic catalysis, and venturing out into fields such as mimicking photosynthesis.

8.2 Overall Conclusions

When we started this dissertation, the burgeoning field of plasmonic catalysis was looking for ways to expand beyond surface chemistry on noble metal surfaces.[1,2] One strategy for doing so

involved coupling plasmonic metals with other catalytically-active materials to create multicomponent plasmonic catalysts capable of collecting the energy of visible light through plasmon excitation and using that energy to perform the catalytic chemistry of some other material. Based on our understanding of energy transfer mechanisms in plasmonic metal-molecule systems, we hypothesized that the energy of light concentrated through LSPR excitation in a plasmonic nanoparticle could be transferred to a catalytic material, attached to the nanoparticle, via LSPR-induced direct electronic excitations in the catalytic material.[3,4] In the case of catalytically-active metals, this hypothesis relied on the fact that the electronic structure of most catalytic metals (Pt, Pd, Ru, etc.) feature d-bands at the Fermi level which allow for direct, momentum-conserved interband excitations in the visible range. We postulated that this enables catalytic metals to act as absorption sinks for the electromagnetic energy concentrated by plasmonic metals. This would allow for energy to be transferred to the catalytic metal through the excitation of energetic charge carriers which could then be used to perform plasmonic photochemical reactions on the catalytic metal.

We laid out a set of design criteria based on our physical understanding of energy flow in plasmonic nanomaterials and settled on synthesizing Ag-Pt alloy and core-shell nanoparticles as model platforms for studying multicomponent plasmonic catalysts. We developed a creative, new synthesis approach for creating bimetallic alloy nanoparticles of immiscible metals (Ag-Pt alloy nanoparticles) through the intermediate synthesis of a bimetallic-oxide precursor. This precursor was made through galvanic replacement of Ag by Pt ions and oxidation of the resulting hollow nanostructures. The surface Pt oxides were then reduced by leveraging the optical properties of Ag. We used visible light as a mild stimulant for the reduction of the stabilizing surface oxide.

Once the oxide was reduced, the nanoparticles became unstable and collapsed which forced the mixing of Pt atoms with Ag to create solid, kinetically-stable Ag-Pt alloys.[5]

Although we were successful in synthesizing Ag-Pt alloy nanoparticles, the resulting materials were not conducive to performing systematic mechanistic experiments. According, we turned our attention to the more well-defined structure of Ag-Pt core-shell nanoparticles. We hypothesized that by coating a thin layer (~ 1 nm) of Pt onto a large core (50-100 nm) of Ag, we could create a bimetallic nanostructure with the hybrid optical properties of Ag and surface chemical properties of Pt. We initially developed a synthesis for such core-shell nanoparticles using an emerging approach from the nanomaterial synthesis literature. However, this synthesis was significantly limited in terms of scalability. We tackled this issue by developing a new, inherently-scalable synthesis approach for the synthesis of core-shell metal nanoparticles. We showed that by chemically modifying a Pt metal complex, we could tune the reactivity of the precursor to favor the slow, epitaxial growth of a thin 1 nm Pt shell on 75 nm Ag nanocubes. Optical UV-vis spectroscopy and probe molecule infrared spectroscopy were used to demonstrate that these bimetallic core-shell nanoparticles displayed both the optical properties of the Ag core and the surface chemical properties of the Pt shell.[6]

We then used these core-shell nanoparticles as model systems to test our hypothesis of re-directing plasmon energy from Ag to Pt. We designed detailed spectroscopic experiments and electrodynamic simulations to study the flow of energy in these hybrid materials. Optical integrating sphere experiments showed that coating this thin 1 nm layer of Pt onto the Ag nanocube cores resulted in a drastic increase in the absorption-to-scattering ratio. These data suggested that the thin Pt at the surface was providing an efficient pathway for the dissipation of plasmonic energy thereby redirecting plasmon energy to the thin Pt shell. Electrodynamic simulations were used to

spatially resolve the flow of energy in the core-shell nanocubes. These data not only confirmed that the Pt shell was biasing the flow of energy towards absorption but also that majority of the absorption in the nanostructure was taking place in the thin 1 nm of Pt at the surface of the nanoparticles.[7]

Lastly, to test whether this redistribution of plasmonic energy could allow for plasmon-driven chemical reactions on non-plasmonic surfaces, we prepared catalysts from our Ag-Pt core-shell nanocubes. We tested the performance of the catalyst using the preferential oxidation of CO in excess H_2 as a probe reaction. Photocatalytic reactivity data showed that illumination of the catalyst under reaction conditions resulted in an increase the rate of the reaction on the Pt surface. Time-resolved and wavelength-depend experiments were then used to demonstrate that the increased reaction rate under visible light irradiation was the product of plasmon excitation by the plasmonic Ag core.[7] Ultimately, this work presents a clear physical framework for controlling energy flow in multicomponent plasmonic systems, summarized in Figure 8.1.
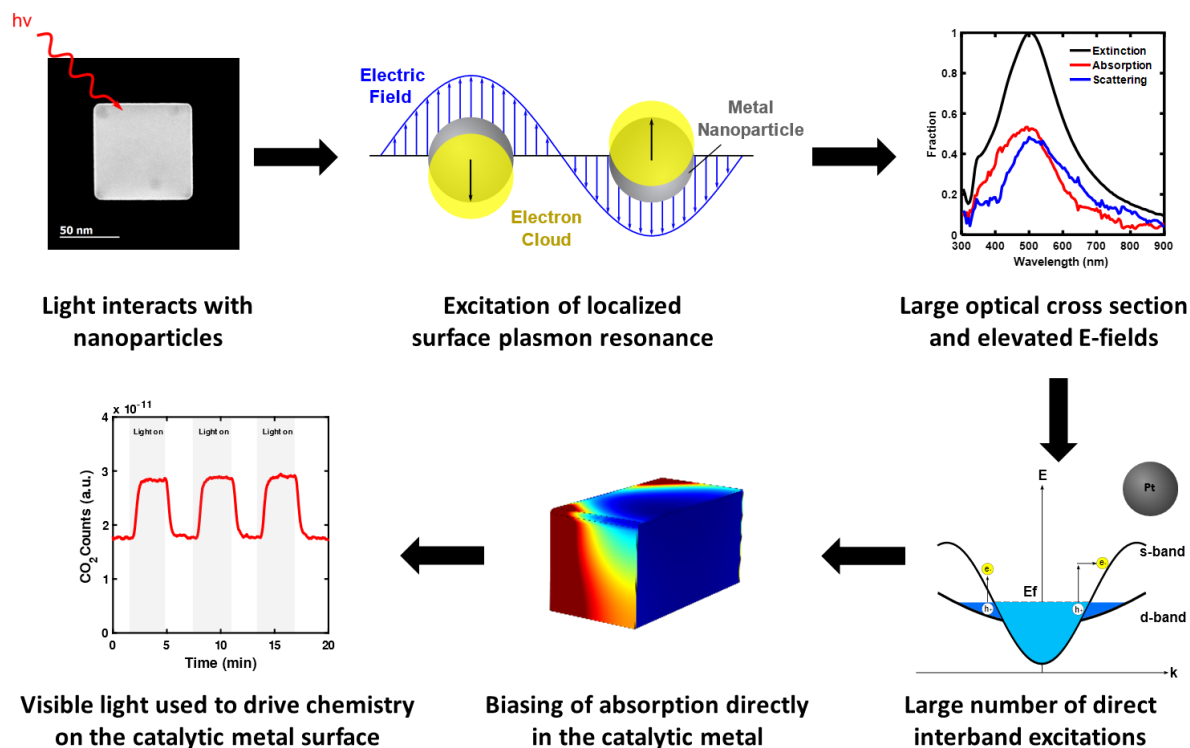
Figure 8.1 Guiding energy flow in multicomponent plasmonic catalysts. Guiding energy from plasmonic Ag to catalytic Pt. Visible light interacts with the Ag-Pt core-shell nanocubes exciting localized surface plasmon resonance in the plasmonic Ag core. Plasmon excitation gives the nanoparticles a large optical cross section allowing them to harvest visible light and concentrate the energy of light in the form of elevated electric fields at the surface of the nanoparticles. The energy stored in the elevated fields localized at the surface channels into the thin Pt shell through inherently-fast, direct electronic excitations in the metal. This produces energetic charge carriers in the Pt shell which can then be used to perform plasmonic photochemical transformations on the Pt surface.

8.3 Future Directions

This dissertation has made significant contributions in the areas of precision nanomaterials synthesis and plasmonic catalysis.[5–7] In particular, this work paves the way for the rational design of other multicomponent plasmonic systems for guiding energy flow in plasmonic, energy harvesting, and photo-catalytic applications. We discuss some of the exciting new possibilities that emerge from these findings in the following section.

8.3.1 Synthesis of New Core/Thin-Shell Multimetallic Nanostructures

We presented a new strategy for the synthesis of multimetallic, core-shell nanoparticles with ultrathin shells by manipulating the chemical reactivity of the shell metal precursor.[6] We believe that this strategy could easily be extended to other combinations of metals. For example, in chapter 5, we demonstrated some preliminary success in the synthesis of Ag-Pd core-shell nanocubes by modifying the chemical reactivity of $[PdCl_4]^{2-}$ precursor via ligand exchange. The recipe presented in chapter 5 suffered from precipitation of Pd salts during ligand exchange, but this could possibly be avoided by exploring different chemical modifiers or even using intermediate exchanges. For instance, ligand exchange with Br^- anions could be performed first followed by exchange with hydroxide to possibly avoid precipitation of Pd salts. Other core-shell combinations that could possibly be achieved using a seed-mediated approach with chemically-modified precursors include Au cores with Pt, Pd, Ni, Fe or other non-plasmonic shells.

Beyond simple bimetallic nanostructures, it is also possible to move into trimetallic or higher order nanostructures. In particular, with the ease of synthesis and scalability of the Ag-Pt core-shell nanoparticles, it may be fruitful to use the Pt shell as a stepping stone for coating other metals onto the surface of these nanostructures. This is attractive because Ag has very little compatibility with other transition metals whereas Pt provides the opportunity to add metals such

as Co or Ni to create core-shell-shell nanostructures or core-alloy shell combinations for plasmonic catalysis.[8–12]

Another tantalizing architecture would combine asymmetric plasmonic cores (such as nanorods) with catalytic metal shells. Asymmetric plasmonic nanostructures often display multiple plasmon modes such as the longitudinal and transverse plasmon mode of Au nanorods.[13,14] Because the transverse plasmon mode overlaps with interband excitations in Au whereas the longitudinal mode does not, it could be possible to selectively transfer energy from an Au core to a transition metal shell by exciting only one plasmon mode. Such hybrid nanoparticles may be quite useful in several applications but especially in near infrared plasmonic heating applications.[15–17]

8.3.2 Demonstrating Unique Reaction Outcomes in Plasmonic Catalysis

Ultimately, the promise of plasmonic catalysis hinges on the ability to demonstrate reaction outcomes unique from those that can be achieved in purely thermal catalysis. There have been a few reports which suggest that it should be possible to access new reaction pathways with potentially higher reaction selectivies through charge carrier-mediated chemistry.[18–20] With the newfound understanding of energy flow from plasmonic metals to catalytic metals, we can now also consider plasmon-mediated charge carrier-driven reactions on non-plasmonic surfaces. An intriguing study from Wolf and Ertl et al. demonstrated that laser excitation of a bulk Ru surface could be used to drive CO oxidation whereas simple heating of the metal mainly resulted in CO desorption.[19] It should be possible, in principle, to reproduce these results using plasmonic metal nanoparticles (in place of the laser) to drive high rates of charge carrier excitation at the Ru-CO interface. Other potential combinations of strongly-interacting metal-adsorbate systems should also be explored such as Pd for selective acetylene hydrogenation or NO_x reduction on Pt.

Another indirect route for demonstrating unique reaction outcomes in plasmonic catalysis involves leveraging the ability of plasmonic structures to reduce surface metal oxides. This phenomenon has been demonstrated a few times but most powerfully in the example of plasmonic Cu nanoparticles.[5,21,22] In this work, plasmonic Cu catalysts were used to perform selective propylene epoxidation; however, the surface of the plasmonic Cu nanostructures oxidized to form Cu-oxide under reaction conditions. It was shown that by shining light under reaction conditions, the surface oxide could be reduced allowing for chemistry to take place on the more selective Cu surface. In this same way, it could be possible to use plasmonic core-shell nanoparticles made of a plasmonic core and a 3d-metal shell to suppress the oxidation of the 3d-metal surface via plasmon excitation thereby allowing the 3d-metal to perform oxidation reactions.

8.3.3 Guiding Plasmonic Energy to Non-metal Catalytic Sites

The ability of plasmonic nanostructure to collect the energy of visible light and guide it to a catalytic active sites could easily be extended to non-metallic active sites. One such active site of potential interest would be molecular catalysts or single-site catalysts. In both these cases, energy harvested by plasmonic nanoparticles can be directed into either molecular catalysts (such as transition metal complexes) or into single metal sites supported on an oxide or carbon through direct electronic (HOMO-LUMO) excitations in those materials (Figure 8.2). These catalytic active sites can then drive chemical reactions. This scheme is analogous to the way plants and bacteria perform photosynthesis. Photosynthetic complexes use strongly-coupled molecular dye aggregates to collect and delocalize the energy of visible light. Enmeshed within these dye aggregates are molecular catalytic active sites which act as sinks for the electromagnetic energy concentrated by the dye aggregates. In multicomponent plasmonic catalyst case, the plasmonic

metal acts as the dye aggregate and the molecular catalyst or single-site catalyst provide the reactive center.
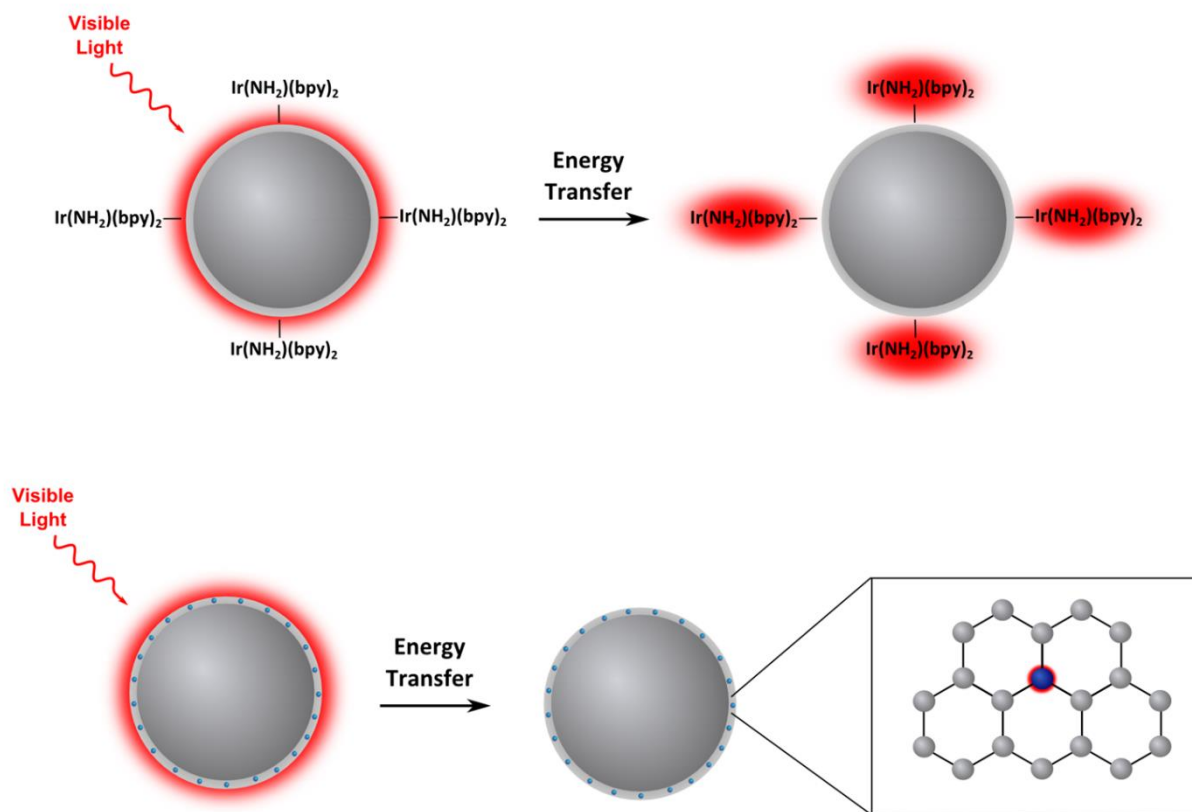

Figure 8.2 Design schemes for other multicomponent plasmonic catalysts. Design schemes for guiding plasmonic energy to molecular catalysts or single-site catalysts. In the top depiction, a molecular catalyst containing ligands with some affinity for metal surfaces (such as amine or thiol groups) is chemically anchored to a plasmonic nanoparticle. Light excites LSPR in the plasmonic metal which results in the concentration of light energy at the surface in the form of elevated electric fields. These fields then their energy into the molecule via HOMO-LUMO excitations thereby energizing the molecular catalyst. In the bottom depiction, the molecular catalyst is substituted for a single-site catalyst immersed in a graphene or silica matrix.

8.4 References

1. Linic, S., Christopher, P. & Ingram, D. B. Plasmonic-metal nanostructures for efficient conversion of solar to chemical energy. *Nat Mater* **10,** 911–921 (2011).

2. Linic, S., Aslam, U., Boerigter, C. & Morabito, M. Photochemical transformations on plasmonic metal nanoparticles. *Nat Mater* **14,** 567–576 (2015).

3. Boerigter, C., Campana, R., Morabito, M. & Linic, S. Evidence and implications of direct charge excitation as the dominant mechanism in plasmon-mediated photocatalysis. *Nat Commun* **7,** 10545 (2016).

4. Boerigter, C., Aslam, U. & Linic, S. Mechanism of Charge Transfer from Plasmonic Nanostructures to Chemically Attached Materials. *ACS Nano* **10,** 6108–6115 (2016).

5. Aslam, U. & Linic, S. Kinetic Trapping of Immiscible Metal Atoms into Bimetallic Nanoparticles through Plasmonic Visible Light-Mediated Reduction of a Bimetallic Oxide Precursor: Case Study of Ag–Pt Nanoparticle Synthesis. *Chem. Mater.* **28,** 8289–8295 (2016).

6. Aslam, U. & Linic, S. Addressing Challenges and Scalability in the Synthesis of Thin Uniform Metal Shells on Large Metal Nanoparticle Cores: Case Study of Ag–Pt Core–Shell Nanocubes. *ACS Appl. Mater. Interfaces* **9,** 43127–43132 (2017).

7. Aslam, U., Chavez, S. & Linic, S. Controlling energy flow in multimetallic nanostructures for plasmonic catalysis. *Nat Nano* **12,** 1000–1005 (2017).

8. Karakaya, I. & Thompson, W. T. The Ag-Pt (Silver-Platinum) system. *Bulletin of Alloy Phase Diagrams* **8,** 334–340 (1987).

9. Wang, D. *et al.* Structurally ordered intermetallic platinum–cobalt core–shell nanoparticles with enhanced activity and stability as oxygen reduction electrocatalysts. *Nat Mater* **12,** 81–87 (2013).

10. Stamenkovic, V. R. *et al.* Improved Oxygen Reduction Activity on Pt3Ni(111) via Increased Surface Site Availability. *Science* **315,** 493–497 (2007).

11. Xin, H., Holewinski, A. & Linic, S. Predictive Structure–Reactivity Models for Rapid Screening of Pt-Based Multimetallic Electrocatalysts for the Oxygen Reduction Reaction. *ACS Catal.* **2,** 12–16 (2012).

12. Cleve, T. V., Moniri, S., Belok, G., More, K. L. & Linic, S. Nanoscale Engineering of Efficient Oxygen Reduction Electrocatalysts by Tailoring the Local Chemical Environment of Pt Surface Sites. *ACS Catal.* **7,** 17–24 (2017).

13. Burrows, N. D., Harvey, S., Idesis, F. A. & Murphy, C. J. Understanding the Seed-Mediated Growth of Gold Nanorods through a Fractional Factorial Design of Experiments. *Langmuir* **33,** 1891–1907 (2017).

14. Gao, J., Bender, C. M. & Murphy, C. J. Dependence of the Gold Nanorod Aspect Ratio on the Nature of the Directing Surfactant in Aqueous Solution. *Langmuir* **19,** 9065–9070 (2003).

15. Huang, X., El-Sayed, I. H., Qian, W. & El-Sayed, M. A. Cancer Cell Imaging and Photothermal Therapy in the Near-Infrared Region by Using Gold Nanorods. *J. Am. Chem. Soc.* **128,** 2115–2120 (2006).

16. Adleman, J. R., Boyd, D. A., Goodwin, D. G. & Psaltis, D. Heterogenous Catalysis Mediated by Plasmon Heating. *Nano Lett.* **9,** 4417–4423 (2009).

17. El-Sayed, I. H., Huang, X. & El-Sayed, M. A. Selective laser photo-thermal therapy of epithelial carcinoma using anti-EGFR antibody conjugated gold nanoparticles. *Cancer Letters* **239,** 129–135 (2006).

18. Kale, M. J., Avanesian, T., Xin, H., Yan, J. & Christopher, P. Controlling Catalytic Selectivity on Metal Nanoparticles by Direct Photoexcitation of Adsorbate–Metal Bonds. *Nano Lett.* **14,** 5405–5412 (2014).

19. Bonn, M. *et al.* Phonon- Versus Electron-Mediated Desorption and Oxidation of CO on Ru(0001). *Science* **285,** 1042–1045 (1999).

20. Zhang, X. *et al.* Product selectivity in plasmonic photocatalysis for carbon dioxide hydrogenation. *Nature Communications* **8,** ncomms14542 (2017).

21. Li, Z. *et al.* Reversible Modulation of Surface Plasmons in Gold Nanoparticles Enabled by Surface Redox Chemistry. *Angewandte Chemie* (2015)

22. Marimuthu, A., Zhang, J. & Linic, S. Tuning Selectivity in Propylene Epoxidation by Plasmon Mediated Photo-Switching of Cu Oxidation State. *Science* **339,** 1590–1593 (2013).

23. Bard, A. J. & Fox, M. A. Artificial Photosynthesis: Solar Splitting of Water to Hydrogen and Oxygen. *Acc. Chem. Res.* **28,** 141–145 (1995).